Aus dem Institut Berlin-Brandenburg Center für Regenerative Therapien (BCRT)

der Medizinischen Fakultät Charité – Universitätsmedizin Berlin

DISSERTATION

Assessment of Cortical Bone Properties at the Tibia Using

Axial Transmission Ultrasound

Abschätzung kortikaler Knocheneigenschaften an der Tibia

mittels axialer Ultraschalltransmission

zur Erlangung des akademischen Grades

Doctor of Philosophy (PhD)

vorgelegt der Medizinischen Fakultät

Charité – Universitätsmedizin Berlin

von

Johannes Matthias Peter Schneider

aus Münster

Datum der Promotion: 13.12.2019

Contents

Abstract

Ultrasonic axial transmission is a non-ionizing, compact and affordable alternative to X-ray-based devices used for fracture risk assessment and osteoporosis diagnosis in the clinic. In this work, a novel 500-kHz axial transmission probe was validated for the assessment of cortical bone microstructure at the tibia against site-matched reference methods. A waveguide model parameterized with cortical porosity (Ct.Po) and thickness (Ct.Th) was used to predict the measured guided wave dispersion curves. To simplify the model, cortical bone was considered as homogenized porous material with fixed matrix elastic properties. The approach was first validated *ex vivo* on 19 tibiae from adult donors without specific bone disorders affecting matrix elastic properties. The best fit between the measured and model-based dispersion curves provided estimates of Ct.Th (R^2 = 0.92, RMSE = 0.20 mm) and Ct.Po (R^2 = 0.83, RMSE = 2.2 %) in agreement with reference data from site-matched micro-computed tomography. We accounted for variations in bone matrix stiffness, reflected in the acoustic impedance measured by scanning acoustic microscopy, and showed that the assumption on a fixed bone matrix stiffness is correct. The approach was then validated *in vivo* at the tibia of 20 patients against site-matched peripheral quantitative computed tomography. Ct.Th was accurately predicted (R^2 = 0.90, RMSE = 0.19 mm) despite the presence of soft tissue. A moderate correlation was found between Ct.Po and volumetric bone mineral density (R^2 = 0.57), which is a strong predictor of Ct.Po. Resonant ultrasound spectroscopy was used to document the elastic tensors of 55 small cortical bone specimens harvested from the axial transmission measurement site. Strong linear correlations between the different elastic coefficients (0.70 < R^2 < 0.99) and between these coefficients and mass density (0.79 < R^2 < 0.89) were found. In conclusion, recovering cortical parameters at the tibia may provide valuable information about skeletal status and fracture risk. Further clinical studies are required to confirm this hypothesis.

Abstrakt

Die axiale Transmission von Ultraschall in der Medizin ist eine nicht-ionisierende, kostengünstige und kompakte Alternative zu herkömmlichen röntgenbasierten Verfahren zur Beurteilung des Frakturrisikos im Rahmen der Osteoporose-Diagnostik. In dieser Dissertation wurde eine neuartige 500-kHz Sonde zur Messung kortikaler Parametern an der Tibia mit Referenzmethoden validiert. Ein Dispersionsmodell, parametrisiert mit kortikaler Dicke (Ct.Th) und Porosität (Ct.Po), wurde automatisch an die experimentellen Dispersionskurven geführter Wellen angeglichen. Der elastische Tensor des Dispersionsmodells wurde in alleiniger Funktion von Ct.Po beschrieben, und zwar unter Verwendung eines Modells mit konstanten elastischen Eigenschaften der Knochenmatrix. Die Methode wurde zunächst an 19 Tibiae *ex vivo* gegen Mikro-Computertomographie validiert. Ct.Th ($R^2 = 0.92$, RMSE = 0.20 mm) und Ct.Po ($R^2 = 0.83$, RMSE = 2.2 %) wurden sehr genau bestimmt. Als Unterschiede in der Matrixsteifigkeit zwischen den einzelnen Proben, abgeschätzt mittels akustischer Rastermikroskopie, berücksichtigt wurden, bestätigte sich die Validität bei der Annahme einer universellen Knochenmatrixsteifigkeit im Dispersionsmodell. Die Messwerte der neuen Sonde wurden dann an der Tibia von 20 Patienten *in vivo* mit peripherer quantitativer Computertomographie verglichen. Ct.Th konnte trotz überlagertem Weichgewebes akkurat vom Dispersionsmodell abgeleitet werden ($R^2 = 0.90$, RMSE = 0.19 mm). Zudem wurde eine moderate Korrelation zwischen Ct.Po und der volumetrischen Knochenmineraldichte festgestellt ($R^2 = 0.57$). Zuletzt wurde Resonanz-Ultraschall-Spektroskopie verwendet, um die elastischen Eigenschaften des kortikalen Knochens an der Ultraschall-Messstelle der Tibia zu dokumentieren. Es fanden sich starke lineare Korrelationen zwischen den elastischen Koeffizienten ($0.70 < R^2 < 0.99$), sowie zwischen diesen Koeffizienten und der Massendichte ($0.79 < R^2 < 0.89$). Über eine Messung kortikaler Parameter an der Tibia könnte in Zukunft das Frakturrisiko eines Patienten besser vorhergesagt werden. Weitere klinische Studien sind erforderlich, um diese Hypothese zu bestätigen.

Abbreviations

μCT	X-ray micro-computed tomography
AT	Axial transmission
BDAT	Bidirectional axial transmission
BMC	Bone mineral content [g·cm^{-1}]
BMD	Bone mineral density [g·cm^{-2}]
BUA	Broadband ultrasonic attenuation [dB·MHz^{-1}]
BWV	Bulk wave velocity [m·s^{-1}]
CTXA	Computed tomography X-ray absorptiometry
CMUTs	Capacitive micromachined ultrasonic transducers
DXA	Dual X-ray absorptiometry
FAS	First arriving signal
FFT	Fast Fourier transform
HMI	Human machine interface
HR-pQCT	High-resolution peripheral quantitative computed tomography
pQCT	Peripheral quantitative computed tomography
QCT	Quantitative computed tomography
RMS-CV	Root-mean-square coefficient of variation
RUS	Resonant ultrasound spectroscopy
SAM	Scanning acoustic microscopy
SVD	Singular vector decomposition
TBS	Trabecular bone score
TMD	Tissue mineral density [g·cm^{-3}]
TOF	Time of flight

1 Introduction

Osteoporosis is a systemic skeletal disorder characterized by a reduction of bone strength. In particular, vertebral and hip fractures impose high morbidity and mortality to society (1). Bone mineral density (BMD) measured with dual-energy X-ray absorptiometry (DXA) is the current standard parameter to diagnose osteoporosis. Though, a large amount of non-traumatic fractures occur in subjects above the diagnostic threshold for osteoporosis (T-score ≤ -2.5) (2). To improve the assessment of fracture risk, research emphasized the importance of cortical bone for the determination of skeletal stability. Recently, it was found that subjects with hip fractures have decreased cortical thickness (Ct.Th) and increased cortical porosity (Ct.Po) at the tibia (3). In the clinic, cortical bone microstructure can be assessed with high-resolution peripheral quantitative computed tomography (HR-pQCT). However, the technology is unlikely to become a screening tool for osteoporosis because it is expensive, based on ionizing radiation, and bound to dedicated rooms.

Alternatively, axial transmission (AT) ultrasound systems are being explored, which are non-ionizing, low-cost, and portable. The setup enables the propagation of ultrasonic waves along the cortex of long bones such as the radius and tibia. The first arriving signal velocity (υ_{FAS}) is a robust measurement parameter, but its ability to discriminate fractures was only found equivalent (4) or lower to DXA (5,6). To improve the discrimination of fractures, researchers considered the phase velocity of the guided A_0 mode (υ_{A0}) (7). The propagation velocity of a guided wave is frequency-dependent. Each guided wave mode exhibits a specific dispersion curve which is determined by the elastic and geometric properties of the cortical waveguide. To date, υ_{A0} has only been measured in the time-domain based on extracted A_0 mode wave packages. In patients, this approach is usually affected by soft tissue, in which ultrasound propagates at similar velocities (~1500 m·s^{-1}) as the A_0 mode in cortical bone (8).

Modern AT systems have focused on the measurement of multiple guided waves. Cortical bone properties are recovered by fitting a physical waveguide model to the measured guided wave dispersion spectrum. For this purpose, a transverse isotropic free plate model was proposed which accounts for the anisotropy of cortical bone (9). The model depends on the waveguide thickness and four elastic parameters. To simplify the model, cortical bone was considered as a homogenized porous material with fixed matrix elastic properties (10). This asymptotic homogenization approach permits to express the four elastic parameters of the transverse isotropic free plate model in sole function of Ct.Po (11). Consequently, the simplified wave-guide model can be used to create a database of theoretical dispersion curves depending on Ct.Th and Ct.Po only. Using a 1-MHz AT probe, the inversion this database was first validated *ex vivo* on a set of human radius and tibia specimens against site-matched X-ray micro-computed tomography (μCT) (12) and then tested *in vivo* at the radius of patients (13).

Resonant ultrasound spectroscopy (RUS) is a non-destructive technique used to measure the effective elastic tensor of small cortical bone specimens (14). Experimental effective elasticity is required to calibrate the fixed tissue stiffness in cortical bone homogenization models, which allow to express the effective elasticity in function of Ct.Po alone. The two-phase material model used for the 1-MHz probe (12,13) was calibrated on the effective elasticity of human femur specimens retrieved from ultrasonic bulk wave velocity (BWV) measurements (11). The fixed tissue stiffness in this homogenization model was found by minimizing the error between the model-predicted and experimental effective elasticity values. In the future, the prediction of guided waves might be enhanced by using a waveguide model that is calibrated directly on the effective elasticity of the measurement site, obtained, for example, from RUS. Compared to the traditional BWV method, RUS is more convenient for measuring small cortical bone specimens, such as those harvested from the human radius or tibia. In this thesis, a novel 500-kHz AT probe was used to characterize the human tibia in terms of cortical microstructure (Ct.Po and Ct.Th) and ultrasonic velocities (υ_{FAS} and υ_{A0}). Moreover, the effective elasticity of cortical bone from the guided wave measurement site of the tibia was measured for the first time using RUS.

2 Aims

The overall aim of this thesis was to validate a novel clinical tool (500-kHz AT) for the assessment of cortical bone parameters at the human tibia. The specific aims were:

- To validate the model-based estimation of Ct.Th and Ct.Po *ex vivo* against site-matched reference values obtained from µCT (study A).

- To test, if accounting for sample-specific variations in tissue stiffness improves the prediction of Ct.Th and Ct.Po, derived from a waveguide model with fixed bone matrix stiffness (study A).

- To validate the model-based estimation of Ct.Th and Ct.Po *in vivo* against reference values from site-matched pQCT and ultradistal HR-pQCT (study B).

- To measure the first arriving signal velocity (υ_{FAS}) using improved signal processing (study A and B).

- To measure the A_0 mode velocity (υ_{A0}) using a novel signal processing (study A and B).

- To document the effective elastic tensors at the AT measurement site using RUS (study C).

3 Background

3.1 Human bone

The human skeleton is composed of two main tissue types: Cortical and trabecular bone. Cortical bone is predominantly found at the central part (diaphysis) of long bones, such as the tibia, radius, or femur. Cortical bone becomes thinner towards the end of those bones (epiphysis), which in turn contains predominantly trabecular (cancellous) bone. Eighty percent of the total body bone mass is cortical with porosities ranging from 2 to 30 %. Trabecular bone forms a network of interconnecting plates and rods with thicknesses in the range 100 - 200 μm. The vertebra and calcaneus, for example, are mainly composed of trabecular bone surrounded by a thin cortical shell. Bone marrow is found inside the bone cavities, which are primary sites of new blood cell production.
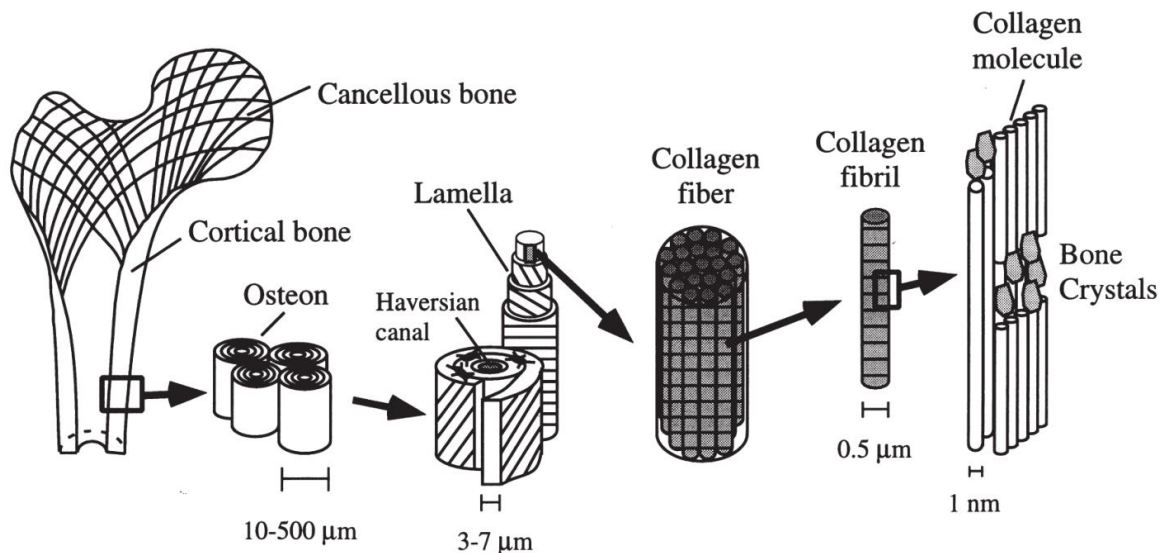

Fig. 1 Hierarchical organization of cortical bone. Reproduced with permission from Elsevier (15).

Bone has a complex hierarchical structure (Fig.1) composed of collagen type I fibers, hydroxyapatite nanocrystals, non-collagenous proteins, and water. Continuous remodeling allows the material to adapt in response to external stimuli and to repair damage. The remodeling is performed by osteoblasts and osteoclasts. A remodeling cycle begins with osteoclasts resorbing bone tissue. Subsequently, osteoblasts are recruited to lay down unmineralized organic matrix (osteoid). During the first few days, osteoid reaches rapidly 70 % of its final mineral content and then slowly matures (16). Remodeling in cortical bone results in osteons consisting of a central (Haversian) canal surrounded by concentric layers of mineralized tissue (lamellae). Trabecular bone is remodeled from the surface with osteoclasts rather cutting trenches than tunnels. Both tissue types are hosting osteocytes which form a complex intercellular network. Apart from regulating phosphate metabolism, osteocytes are mechanosensitive, signal the presence of local damage, and recruit osteoclasts to initiate bone remodeling (17).

3.2   Osteoporosis

Osteoporosis is characterized by imbalanced remodeling of bone tissue with resorption exceeding formation through increased osteoclastic activity (18). As a consequence, the skeleton is destabilized and may fracture due to minor overload. Typical osteoporotic fracture sites are the wrist, spine, and hip. Trabecular bone architecture rapidly deteriorates in patients with increased bone resorption due to its high surface area. That is why vertebral compression fractures may occur early after the onset of osteoporosis, typically after the 50th year of life (19). Postmenopausal women are at particular fracture risk because estrogen deficiency is associated with higher osteoclast activity and, therefore, higher bone resorption (20). In cortical bone, the porosity increases with high variations in pore diameter ranging from 50 to 450 μm, and shape. The cortical bone may also become thinner by conversion into trabecular bone (trabecularization) (Fig. 2b).
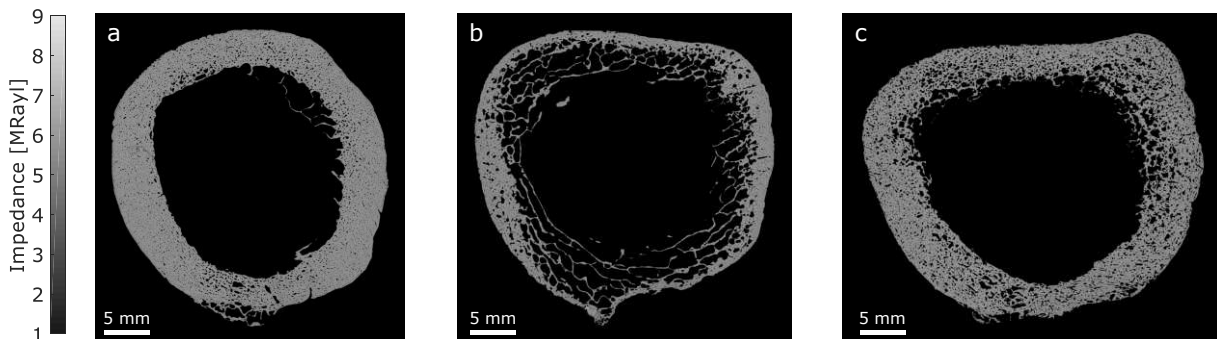
Fig. 2 Femoral shaft cross-sections from different elderly human donors scanned with 100-MHz scanning acoustic microscopy (SAM). (**a**) Intact bone with normal cortical porosity (~8 %) and thickness (~5 mm). (**b**) Trabecularized sample with decreased cortical thickness (~2 mm). (**c**) Sample with normal cortical thickness (~5 mm) and increased porosity (~20 %).

3.3   In-vivo assessment of fracture risk

In this section, the diagnostic methods included in the current German guideline for osteoporosis management and fracture risk estimation are discussed (DVO-Leitlinie 2017). Note that only DXA is recommended for use in routine clinical practice. However, other results from quantitative computed tomography (QCT), trabecular bone score (TBS), or calcaneal quantitative ultrasound (QUS) may be included in the fracture risk assessment, when available.

3.3.1   Dual X-ray absorptiometry (DXA)

This clinical standard method is based on two X-ray beams of different energy transmitted through the examined skeletal site, i.e. the proximal femur or lumbar spine. The separate evaluation of the two absorption spectra allows to eliminate soft tissue effects. Areal BMD (aBMD in g·cm^{-2}) is then derived from the attenuation coefficient. For each site, T-scores are calculated defined as the difference between

the measured aBMD and the mean aBMD of a healthy reference population. According to the World Health Organization criteria, osteoporosis is diagnosed when a T-score is lower than -2.5. DXA scans represent 2D projections of complex 3D structures. This impedes the assessment of bone size and separate evaluation of cortical and trabecular compartments. In particular, bone size is important because larger bones will convey superior strength. The DVO-guideline proposes a risk model combining the T-score with clinical risk factors, such as age, smoking, or prolonged glucocorticoid use. Moreover, DXA images can be used to calculate a trabecular bone score (TBS). Although the TBS is not a direct measure of trabecular bone microarchitecture, it was shown to reflect the structural quality of trabecular bone (21).

### 3.3.2 Quantitative computed tomography (QCT)

In QCT, a skeletal site is imaged using X-rays from multiple angles around a single rotational axis. Based on algebraic reconstruction techniques, tomographic images are reconstructed. Calibration phantoms are scanned with the patient to transform the grey-scale values into volumetric BMD (vBMD in $g \cdot cm^{-3}$). In general, the trabecular regions of the hip and spine are evaluated. However, dedicated segmentation software (e.g. the Medical Image Analysis Framework, University of Erlangen) can be used to calculate additional parameters of the cortical bone compartment, such as Ct.Th. Computed tomography X-ray absorptiometry (CTXA) is a tool for femur scans providing DXA-equivalent aBMD and T-score values. The major limitation of QCT is the limited spatial resolution and anisotropic voxel size, which is usually in the order of 0.5 x 0.5 x 1 mm. This complicates the evaluation of skeletal sites with thin cortical bone, such as the femoral neck or vertebrae. Regarding the assessment of fracture risk, consistent prospective clinical studies and large standardized reference data are still lacking.

3.3.3 Peripheral quantitative computed tomography (pQCT)

Compared to QCT, the peripheral QCT (pQCT) scanner is more compact with smaller gantries. The relatively low-cost and portable device is exclusively produced by Stratec Medizintechnik in Germany. Usually, the tibia or radius is imaged in single-slice mode at different scan locations. A typical site for the evaluation of cortical bone at the tibia is at 66 % of the total bone length. After scanning, a dedicated software automatically segments the cortical and trabecular compartments based on fixed thresholds. Average vBMD values are then calculated from grey-level values and daily calibration scans. Moreover, bone stability indexes can be obtained integrating information on the distribution of bone material, e.g. cross-sectional moments of inertia (22). Nevertheless, few studies have investigated the association between pQCT and fracture risk. A prospective study found that several bone stability indexes measured at the radius and tibia were strongly associated with non-vertebral fractures (23), but the improvements over DXA were only minor.

3.3.4 High-resolution peripheral quantitative computed tomography (HR-pQCT)

The HR-pQCT technology is being developed in Switzerland by Scanco Medical. The clinical scanner allows to image bone microstructure at the tibia and radius with a physical resolution in the order of 100 µm. Due to integrated cooling systems, the scanner is much heavier compared to pQCT. The first generation HR-pQCT was introduced in 2004 with an isotropic voxel size of 82 µm. Ten years later, the second generation HR-pQCT entered the market with superior image stack, faster scanning and smaller voxel size (62 µm). Although the novel scanner has a better resolution, small cortical pores may still not fully be resolved (24). Usually, the ultradistal sites are scanned in order to visualize the trabecular bone architecture (Fig. 3b). However, the ultradistal cortex is very thin (Ct.Th < 2 mm) which complicates the accurate differentiation between cortical and trabecular bone compartments (25). Therefore, cortical bone parameters should be assessed more proximally which is possible with the second generation HR-pQCT.
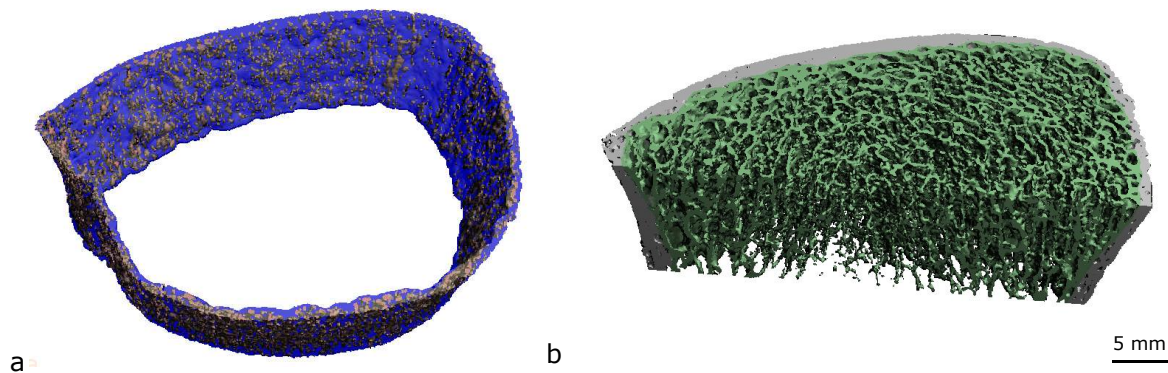
Fig. 3 HR-pQCT images from the ultradistal tibia (82 µm voxel size). (**a**) The segmented intracortical pores are shown in grey. (**b**) The segmented cortical and trabecular compartments are shown in grey and green, respectively. Images courtesy of Z. Ritter.

3.3.5 Calcaneal quantitative ultrasound (QUS)

The calcaneus scanner, commercialized in the 1990s, is the earliest and best-validated clinical QUS technology for the assessment of fracture risk. In a pioneering work, women with hip fractures were discriminated from non-fractured controls by measuring the broadband ultrasonic attenuation (BUA) (26). The attenuation of ultrasound transmitted through the heel depends on the amount and material properties of the trabecular bone structure. However, the relation is complex due to multiple effects that occur simultaneously, such as scattering, diffusion, and absorption. In the range 0.2 – 0.6 MHz the attenuation is linearly proportional to frequency. The slope of the attenuation curve with respect to frequency was shown to depend on BMD (27). Large prospective clinical studies then demonstrated the ability of BUA to predict fractures (28), but the technology did not overcome important challenges, such as the collection of large reference data and standardization between different systems. Conversion formulas have been established for six different commercial heel scanners on the Japanese market, reflecting an attempt of standardization in the bone ultrasound field (29).

3.4 Ex-vivo assessment of cortical bone properties

3.4.1 Scanning acoustic microscopy (SAM)

Scanning acoustic microscopy (SAM) provides both elastic and structural information of bone tissue with spatial resolutions ranging from 1 to 25 µm (Fig. 2) (30). Bone samples are positioned below a focusing ultrasound transducer operating in the frequency range of 50 MHz - 2 GHz. Typically, degassed and temperature-controlled water is used as coupling fluid. The sample surface needs to be flat and smooth without scratches to avoid changes in the propagation direction of the incident waves. Images are acquired by raster scanning the surface in the focal plane of the transducer. For each scan point, the reflected acoustic wave from the sample surface is recorded. The reflection amplitude is directly proportional to the reflection coefficient R, which is determined by the acoustic impedance mismatch between the bone sample (Z_B) and coupling fluid (Z_{CF}):

$$R = \frac{Z_B - Z_{CF}}{Z_B + Z_{CF}}.$$

(1)

The reflection amplitude is usually obtained from the maximum of the Hilbert transform H_{max}. A calibration curve correlating the reflection amplitude of scanned reference materials with their corresponding well-known reflection coefficients is used to transform H_{max} into R (31). The calculation of Z_B (expressed in Mrayl, 1 rayl = 1 kg·m^{-2}·s^{-1}) then becomes possible via equation (1) with Z_{CF} being known. When the wave propagation and particle displacement are in the same direction x_i, the acoustic impedance Z_{ii} is proportional to the elastic coefficient c_{ii} and the mass density ρ:

$$Z_{ii} = \sqrt{c_{ii}\,\rho}.$$

(2)

The acoustic impedance was shown to be a strong predictor for the elastic stiffness of bone tissue in the probing direction ($R^2 = 0.996$) (32).

3.4.2 X-ray micro-computed tomography (µCT)

X-ray micro-computed tomography (µCT) is routinely used in research to evaluate cortical and trabecular bone morphology with standardized nomenclature and key variables (33). Tissue mineral density (TMD) can be obtained from the average attenuation value of bone tissue. Most µCT systems generate polychromatic X-ray beams which are the cause for beam hardening artefacts. Although beam hardening reduction methods are available, e.g. aluminum filters or correction algorithms, it is important to adjust the

X-ray energy to the diameter and density of the object being scanned. In the early stage of the development, μCT was mainly used to measure trabecular bone microarchitecture (34). In recent years, enhanced resolution allowed researchers to visualize and quantify the complex cortical pore network (35).

3.4.3   Resonant ultrasound spectroscopy (RUS)

Resonant ultrasound spectroscopy (RUS) is a non-destructive method used to estimate the elastic tensor of rectangular parallelepiped cortical bone specimens (14). The specimen is clamped with slight contact between two shear transducers, which act as emitter and receiver (Fig. 4a). The resonant frequencies are recorded by tuning the frequency band, typically in the range between 150 - 500 kHz. Then, the elastic tensor is estimated by comparing the experimental resonant frequencies to those obtained from a model. The resonant frequencies are completely determined by the geometry, mass density, and elastic moduli of the specimen. With given geometry and mass density of the specimen, the elastic constants of the model can be adjusted until reaching the best match between the predicted and measured resonant frequencies. In low damping materials, such as metals, the resonant frequencies are clearly separated. In bone, which is a highly damping material, the peaks are broad and strongly overlap (Fig. 4b). To overcome this problem, a statistical approach was proposed including the modelling errors and measurement uncertainties in the inverse problem (Bayesian formulation) (36).
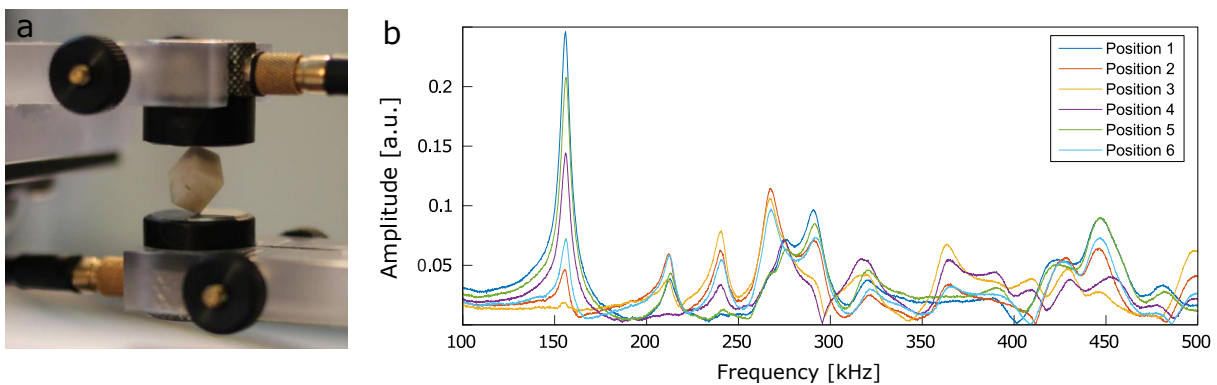
Fig. 4 (**a**) Resonant ultrasound spectroscopy (RUS) of a small (3 x 3 x 4 mm) rectangular parallelepiped cortical bone specimen clamped between two shear ultrasound transducers. (**b**) Typical set of spectra showing the relative amplitudes of the resonant frequencies which vary when the specimen is rotated (Position 1 – 6). Images courtesy of Xiran Cai.

3.5   Axial transmission (AT)

Ultrasound is transmitted by a source through the skin to the surface of a long bone where vibrations are generated that continuously interact with the cortical boundaries. In that way, ultrasonic waves are guided over distances up to several centimeters. The ultrasound propagation can be detected by sensors placed on the surface of the skin through waves leaking out from the cortical bone into the overlaying soft tissue.

Early approaches implemented a simple configuration with one transmitter and receiver, separated a few centimeters from each other (Fig. 5). This setup was used to evaluate the velocity of the first arrival signal (υ_{FAS}) (37). Although υ_{FAS} contains relevant information on the cortical bone microstructure and material properties (38), the ability to discriminate fractures was found lower (5,6) or equivalent to DXA (4).
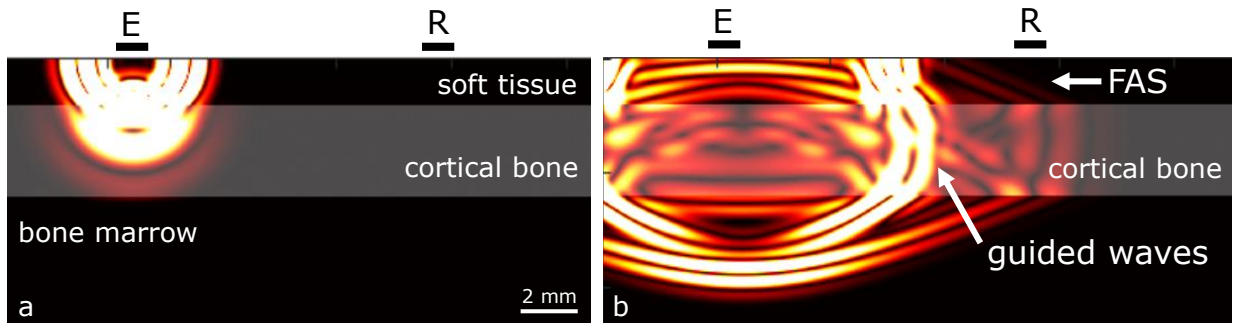
Fig. 5 Snapshots of 2D ultrasonic wave propagation in a cortical bone plate. (**a**) Snapshot taken at 3 µs after emission. The waves have entered the cortical bone layer. (**b**) Snapshot taken at 7 µs after emission. The first arriving signal (FAS) is followed by slower propagating guided waves. E: emitter. R: receiver. The simulations were conducted in SimSonic2D (www.simsonic.fr).

Current research has focused on the measurement of ultrasonic guided waves, which arise from multiple reflections and mode conversions at the waveguide boundaries (39). Each guided wave mode exhibits a characteristic dispersion curve determined by the geometric and elastic properties of the waveguide. Bidirectional multi-emitter multi-receiver array probes are being developed in our group for guided wave measurements in cortical bone. Fig. 6a shows the novel 500-kHz probe used in this thesis at the human tibia. The probe consists of a central 24-receiver array (1.2 mm pitch) and two lateral 5-emitter arrays (1.5 mm pitch) separated by a distance of 8 mm. Five time delays ranging from 0 to 0.8 µs are used to excite the emitters successively. Consequently, five different array waveforms of 24 time-domain signals are recorded for each propagation direction (Fig. 6b).
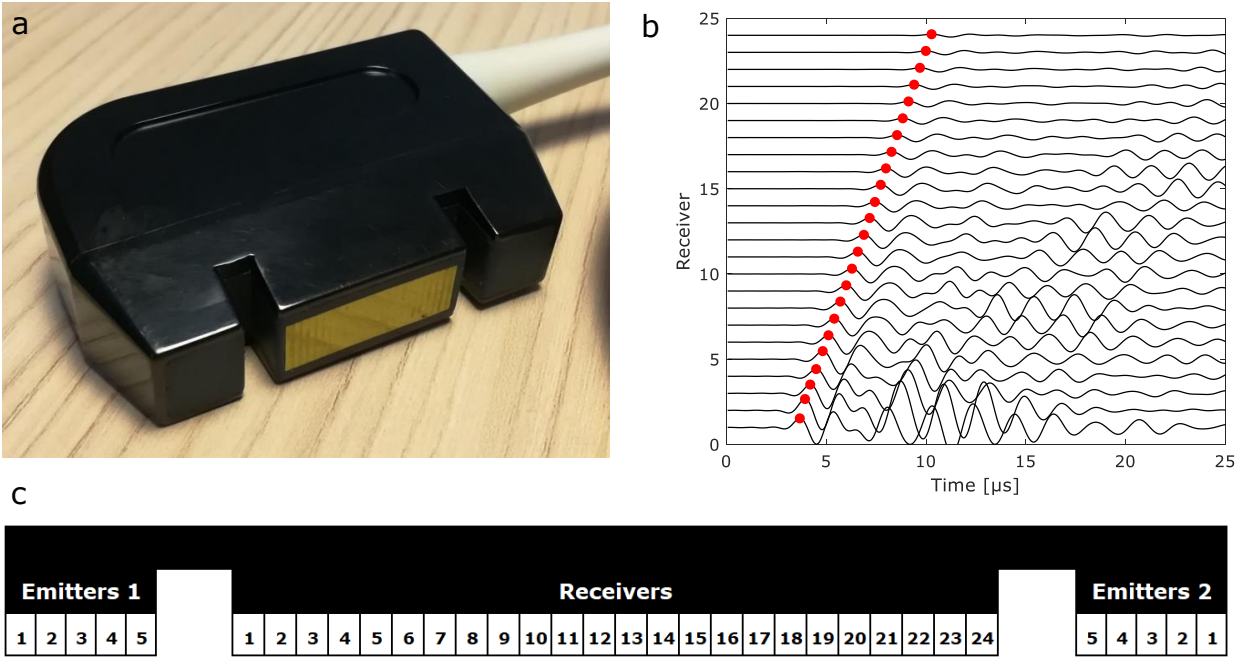
Fig. 6 (**a**) 500-kHz axial transmission (AT) probe designed for the tibia. Picture courtesy of D. Ramiandrisoa. (**b**) Typical array waveform recorded at the human tibia *ex vivo* (study A). The detected first arriving signals (FAS) are marked in red. (**c**) Schematic diagram showing the array arrangements of the probe.

First arriving signal velocity (v_{FAS})

The bidirectional principle allows to correct errors induced by small inclination angles between the probe and the bone surface. The harmonic mean of two sound velocities (V_1 and V_2) measured in opposite directions provides the corrected first arriving signal velocity (v_{FAS}) (40):

$$v_{FAS} = \frac{2}{\frac{1}{V_1} + \frac{1}{V_2}}. \tag{3}$$

The unidirectional sound velocities are derived from the time delays between the first arriving signals (FAS) detected at each receiver. The time of flight (TOF) of the FAS is defined as the first extremum emerging from noise (Fig. 7a). The exact TOF is obtained from a parabolic interpolation around the first extremum (Fig. 7b). V_1 and V_2 are inferred from the inverse slope of a linear regression between the TOF and known inter-receiver distances (Fig. 7c).
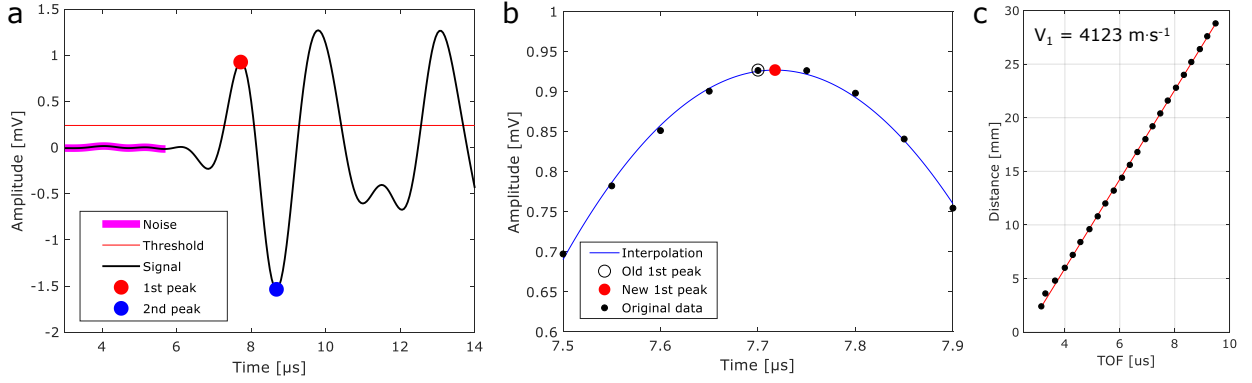
Fig. 7 (**a**) The first arriving signal (FAS) is defined as the first extremum emerging from noise. (**b**) The exact temporal location is refined using a parabolic interpolation around the first extremum. (**c**) The inverse slope of a linear regression between the determined times of flight (TOF) and known inter-receiver distances provides the sound velocities V_1 and V_2.
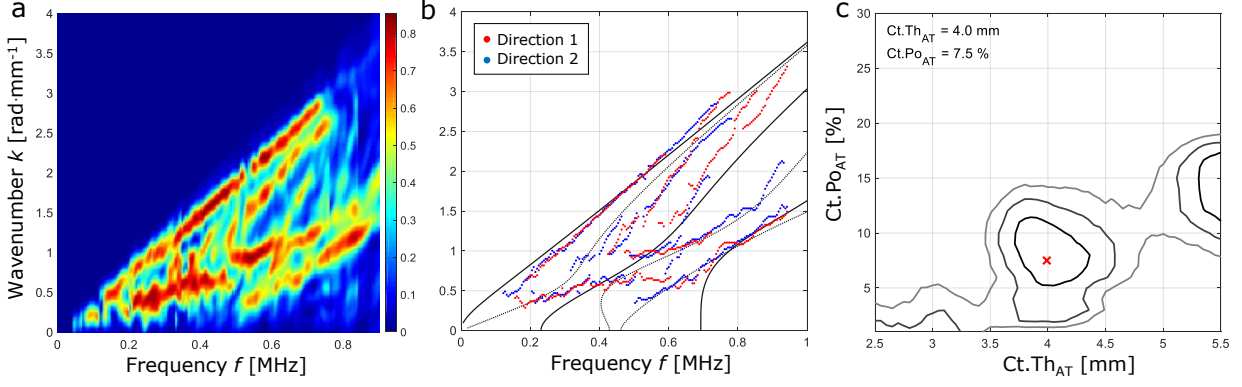
Estimation of Ct.Th and Ct.Po

The estimation of Ct.Th and Ct.Po based on a 2D transverse isotropic free plate model was recently validated *ex vivo* using a 1-MHz probe for the radius (12). For the purpose of this thesis, the previously described signal processing was applied to the novel 500-kHz probe designed for the tibia. In the following, the signal processing procedure is described in detail.

1. Experimental dispersion curves

The so-called *Norm function* reveals the presence rate of a guided wave mode in a normalized scale between 0 and 1 (Fig. 8a). To obtain the *Norm function*, each temporal signal is Fourier transformed to produce a response matrix R with the size N^E x N^R x N^f, where N^E is the number of emitters, N^R the number of receivers and N^f the number of frequencies. A singular value decomposition (SVD) is processed at each frequency N^f on the N^E x N^R elements of R generating N^E singular vectors (41). The weak singular vectors containing the noise from the signal are removed (denoising). A testing vector e^{test} is defined as a normalized and attenuated spatial plane wave with a complex wave number (42). The projection of e^{test} on the denoised singular vector basis $U(f)$ provides:

$$Norm(f,k) = \|e^{test}(k)\|^2_{U(f)}. \tag{4}$$

In the *Norm function*, the maxima of the guided wave modes are close to 1 while the contribution of noise is close to 0. Accordingly, the dispersion curves can be extracted above a heuristical threshold, which is usually set to 0.4. In the next step, the extracted maxima of the guided wave modes are fitted to the theoretical dispersion curves (Fig. 8b) calculated from a 2D transverse isotropic free plate waveguide model. The procedure is performed on the signals from both propagation directions.

15

Fig. 8 Signal processing procedure for the estimation of Ct.Th and Ct.Po. (**a**) *Norm function* calculated from singular values at each frequency and projection of a testing vector onto the singular vector basis. (**b**) Extracted local maxima from bidirectional measurements (red and blue dots) fitted to the symmetric (dashed lines) and anti-symmetric (continuous lines) dispersion curves of a waveguide model. (**c**) Contour plot representation of the objective function with red cross indicating the global solution.

2. Theoretical dispersion curves

The theoretical dispersion curves are obtained from a 2D transverse isotropic non-absorbing free plate model, which was shown to accurately predict the experimental modes at the human radius *ex vivo* (43). In what follows, the directions x_2 and x_3 of the free plate model are considered infinite and the dimension x_1 as finite. The isotropy plane is parallel to the x_1x_2-plane and guided waves propagate only along the x_1x_3-plane. Consequently, the wave propagation can be described by four independent elastic coefficients $(c_{11}, c_{13}, c_{33}, c_{55})$, the mass density ρ, and the plate thickness h. The general form of the dispersion equation can be written as:

$$F_{A,S}(f, k; c_{11}, c_{13}, c_{33}, c_{55}, \rho, h) = 0. \tag{5}$$

A and S represent the antisymmetric and symmetric modes, respectively. The dispersion equation can be expressed in function of three bulk wave velocities. The mass density ρ is then embedded in the velocity parameters:

$$V_L^\perp = \sqrt{\frac{c11}{\rho}}, \ V_L^\parallel = \sqrt{\frac{c33}{\rho}}, \ V_T = \sqrt{\frac{c55}{\rho}}. \tag{6}$$

$V_L^\perp$ and $V_L^\parallel$ correspond to compressional waves propagating along the x_1-and x_3-axes, respectively, whereas V_T corresponds to a shear wave propagating along the x_3-axis. Consequently, the components in

the dispersion equation which account for the plate stiffness can be alternatively formulated as two bulk wave velocities and two stiffness ratios:

$$F_{A,S}\left(f, k; \frac{c13}{c11}, \frac{c33}{c11}, V_L^{\perp}, V_T, h\right) = 0. \tag{7}$$

Granke et al. suggested that the effective (mesoscale) elasticity of cortical bone specimens from the human femur can be reasonably predicted by Ct.Po alone (11). In that study, a micromechanical model was used considering cortical bone as a homogeneous transverse isotropic matrix pervaded by periodically distributed cylindrical pores filled with water (Fig. 9b) (44). The theoretical approach allows one to compute the effective elastic tensor, with given elasticity of the matrix C^m and pore fluid C^f, the mass densities of the latter ρ^m and ρ^f, and Ct.Po. The cortical bone matrix was considered uniform among individuals. Fig. 9c shows that the effective elastic coefficients computed from the model correlate well with the experimental data.
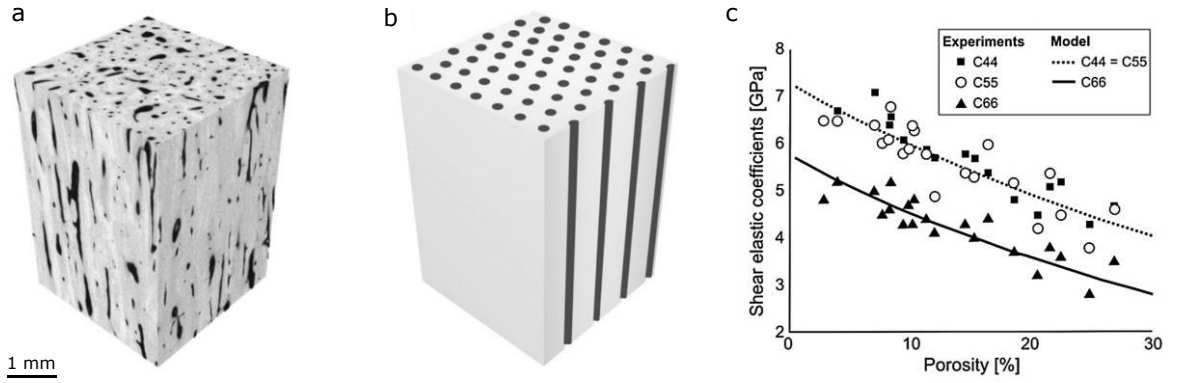
Fig. 9 (**a**) Reconstruction of cortical bone volume from synchrotron radiation µCT. (**b**) Cortical bone simplified as homogeneous anisotropic matrix pervaded by periodically distributed cylindrical pores. (**c**) Effective longitudinal elastic coefficients versus porosity: results from experiments and model (solid and dotted lines). Reproduced with permission from Elsevier (11).

The above mentioned micromechanical model is used to calculate a set of effective mesoscale stiffness tensors for different Ct.Po values with a fixed transverse isotropic elasticity of the matrix C^m and mass density ρ^m (Table 1) (11). In other words, one particular Ct.Po value corresponds to four effective elastic coefficients (c_{11}, c_{13}, c_{33}, c_{55}) and to the effective mass density ρ which can be calculated using the following equation:

$$\rho = \rho^m \times (1 - Ct.Po) + \rho^f \times Ct.Po. \tag{8}$$

17

Microscale		Mesoscale	
Fixed properties	Variable parameter	Effective properties	Model parameters
ρ^m, C^m, ρ^f, C^f	Ct.Po	$c_{11}, c_{13}, c_{33}, c_{55}, \rho,$	$\dfrac{c_{11}}{c_{11}}, \dfrac{c_{33}}{c_{11}}, V_L^{\perp}, V_T$

Table 1 Input (microscale) and output (mesoscale) parameters of two-phase homogenization model.

To compute the theoretical dispersion curves via equation (7), the model output parameters can be rewritten in terms of two stiffness ratios (c_{13}/c_{11} and c_{33}/c_{11}) and bulk wave velocities ($V_L^{\perp}$ and V_T). In summary, the waveguide model has been parameterized in terms of Ct.Po assuming that the mineralized cortical bone matrix is spatially homogeneous and uniform among individuals.

3. Inversion scheme

The best fit between the theoretical and experimental dispersion curves is obtained by maximizing the objective function, defined as the projection of a tested model into the singular vector basis $U(f)$ of the *Norm function* (4):

$$Proj(Ct.Th, Ct.Po) = \frac{1}{fmax - fmin} \int_{fmin}^{fmax} \sum_{m=1}^{M} \left\| e^{test}\left(k_m(f, Ct.Th, Ct.Po)\right) \right\|_{U(f)}^2 df, \qquad (10)$$

where f_{min} and f_{max} correspond to the limits of the frequency bandwidth and M denotes the number of theoretical guided wave modes. Similar to the *Norm function*, each pixel of the objective function reflects the presence rate of a tested model in a 0 - 1 scale. This approach is efficient because at each frequency only a finite number of experimental modes is present for a projected model.

4   Materials and Methods

4.1   Samples and patients

Nineteen tibia pairs without soft tissue from human cadavers (6 male, 13 female, age 69 – 94 years, mean 83.7 ± 8.4 years) were used in study A (left side) and study C (right side). In study B, twenty patients (12 male, 8 female, age 69 – 94 years, mean: 51 ± 14 years) participated. Table 2 shows the applied methods per study.

	Study A	Study B	Study C
Methods	- AT - µCT - SAM	- AT - pQCT - HR-pQCT	- RUS
Samples / Patients	19 tibiae	20 patients	19 tibiae

Table 2 Overview of samples, patients, and methods used in the three studies.

4.2   Measurement protocol

The former AT measurement protocol used in our group for the 1-MHz probe included three cycles of ten successive measurements per specimen (12). In study A and B, notably longer scan times were applied, i.e. three cycles of 400 successive measurements per tibia. Thereby, the probe was slowly tilted in both circumferential directions to scan a wide region above the medullary cavity.

4.3   Statistical analysis

In study A and B, linear regression analysis and Pearson's correlation coefficients were used to quantify the degree of association between all parameters site-matched with AT. Bland-Altman plots were used to reveal biases in the prediction of Ct.Po and Ct.Th obtained from the waveguide model. The single-cycle repeatability of the AT measurements, expressed as root mean square coefficient of variation (RMS-CV), was assessed from the repeated cycles per tibia. Paired *t*-tests and Wilcoxon signed-rank tests were used to test for differences between the means. In study A, a stepwise multiple regression analysis was used to evaluate the optimal combination of parameters for the prediction of Ct.Po and Ct.Th. In study B, the associations between AT and HR-pQCT were assessed using the Spearman's rank-correlation coefficient due to the small sample size (N = 8). In study C, linear least square regressions were computed to analyze the relationships between the different elastic coefficients, quality factors, and mass densites. The level of significance for all statistical tests in this thesis was set to $p < 0.05$.

4.4 Data analysis

First arriving signal velocity (v_{FAS})

In study A and B, the following adjustments to the previously used v_{FAS} algorithm (40) were made. Two binary masks were applied to the array waveforms restricting the region for the noise floor calculation (magenta) and FAS detection (green). The starting position for both masks was calculated from the sum of the last three signals (Fig. 10b). The signals of the first receivers were not considered, although much stronger in amplitude, because in patients with thick soft tissue the detected waves may have traveled through soft tissue only without having reached the bone (see first signal in Fig. 10a). The envelope (Hilbert transform) was computed from the sum of the last three signals. The first peak was determined from the envelope (Fig. 10c) based on a threshold that was 0.4 times the maximum of the envelope amplitude. The temporal location of this peak was used as starting position for the two masks at the last (24th) signal. From this position, the masks followed down the FAS with fixed slopes corresponding to the average axial bulk wave velocity in cortical bone (3900 m·s⁻¹) (4). The width of the green mask was chosen large enough to cover a broad range of individual sound velocities, i.e. 3400 – 4300 m·s⁻¹.
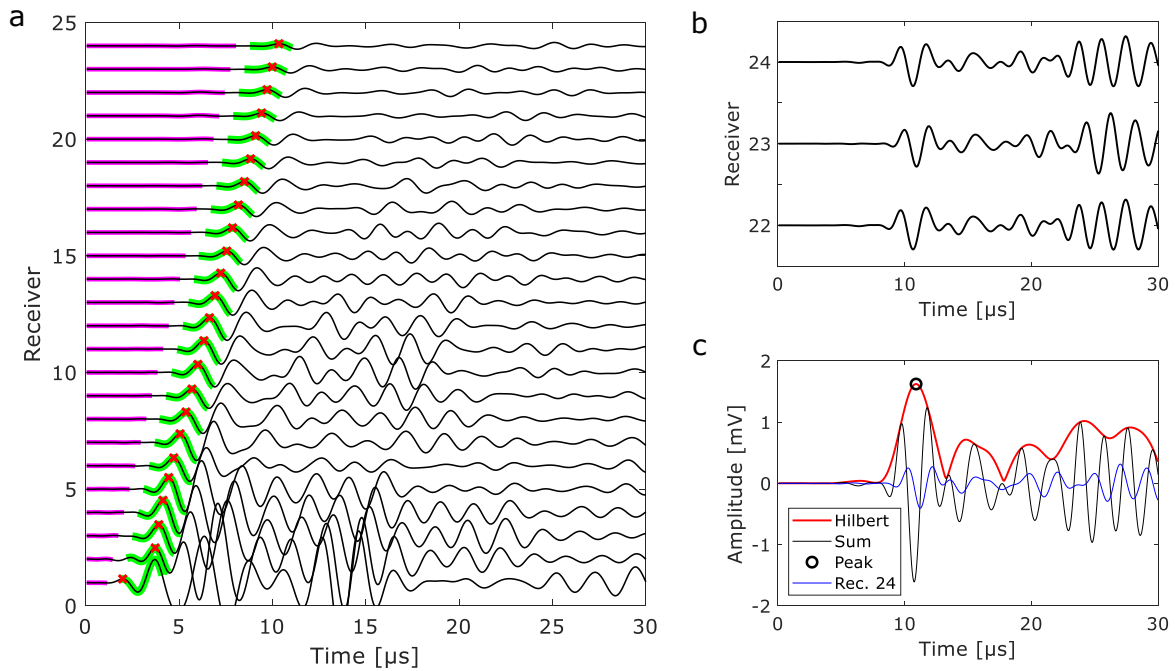
Fig. 10 Signal processing steps for the calculation of the first arriving signal velocity (v_{FAS}). (**a**) The noise level of each receiver is measured in the time interval marked in magenta used to determine the threshold for the peak detection in the time interval marked in green. (**b**) The last three signals (22 – 24) are summed and then Hilbert transformed. (**c**) The temporal location of the first peak is used as starting position at the latest receiver (24) for both masks which then follow down the FAS with fixed slopes.

A₀ mode velocity (υ_{A0})

In study A and B, a novel signal processing method for the calculation of υ_{A0} in the frequency-domain was applied. The first step was to convert the *Norm function* from wave number k (Fig. 11a) into phase velocity cp ($c_{phase} = 2\pi f / k$) (Fig. 11b). Subsequently, the A₀ mode was extracted within a window with fixed ranges (Fig. 11c). For both studies the same phase velocity range was used (1400 to 1900 m·s⁻¹), whereas the frequency range was set higher and wider in study A (0.5 - 1.0 MHz) compared to study B (0.4 - 0.5 MHz). Within the window, the extracted amplitudes of the *Norm function* were averaged over frequency, generating a characteristic single-peak function (Fig. 11d). The maximum of that function was defined as unidirectional υ_{A0}. The harmonic mean of two υ_{A0} measurements in opposite directions was calculated to correct for small inclination angles between the probe and bone surface (40).
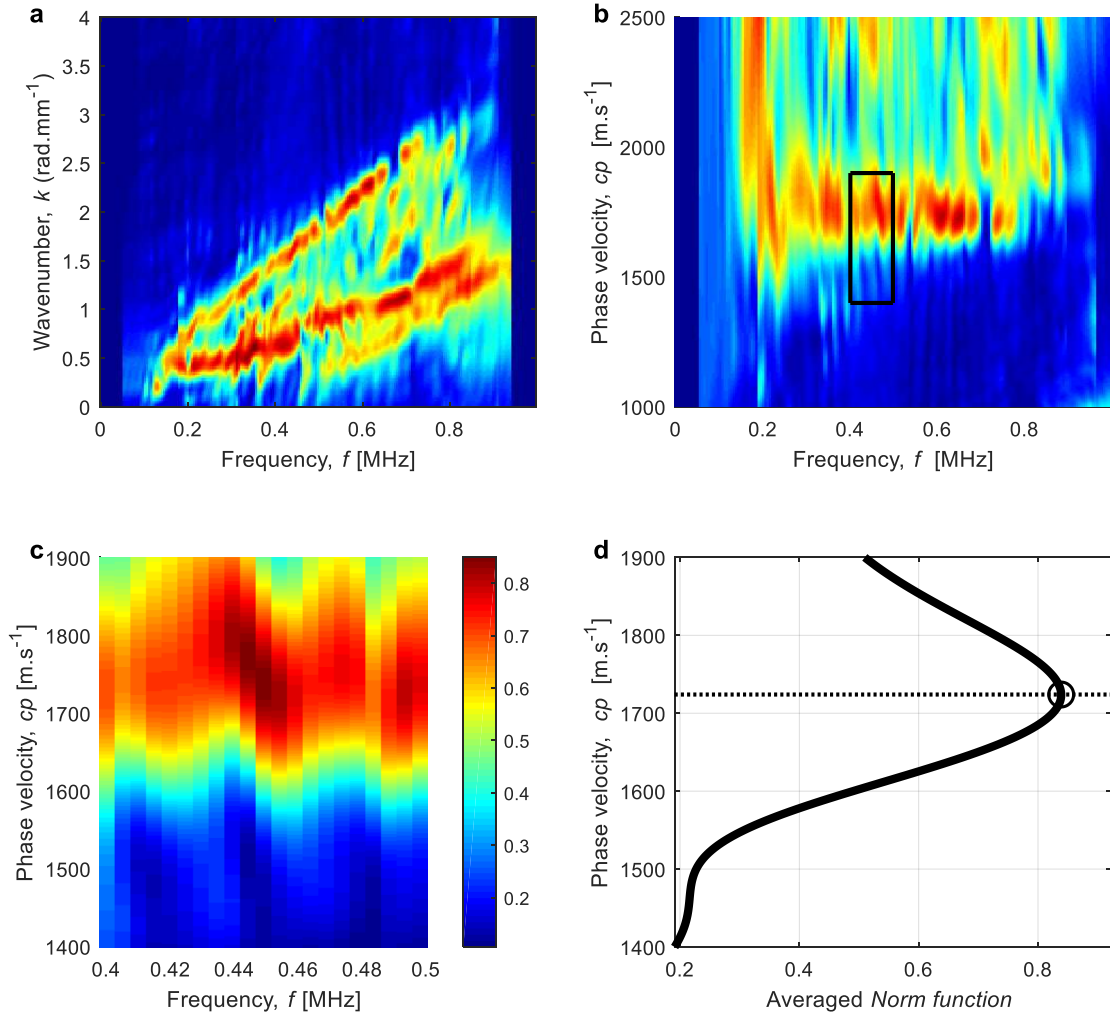
Fig. 11 Signal processing steps for the calculation of the A₀ mode velocity. The *Norm function* is converted from the frequency-wavenumber (**a**) into the frequency-phase velocity domain (**b**). (**c**) The A₀ mode is extracted in a window with fixed ranges. (**d**) The amplitudes of the *Norm function* are averaged over frequency generating a characteristic single-peak function with the maximum defined as υ_{A0}. *In-vivo* measurement from study B.

5 Results

5.1 Study A – AT *ex vivo*

The results from 17 specimens were used for statistical analysis. The best predictor for $Ct.Po_{\mu CT}$ was $Ct.Po_{AT}$ ($R^2 = 0.83$, p < 0.001, RMSE = 2.2 %). The Bland-Altman plot revealed a bias of Ct.Po that depended positively on the porosity level. This effect was also reflected in the slope of the linear regression which, however, was not statistically different from 1 (confidence interval: 1.00 - 1.68). $Ct.Th_{\mu CT}$ was best predicted by $Ct.Th_{AT}$ ($R^2 = 0.92$, $p < 0.001$, RMSE = 0.20 mm) after the exclusion of one sample with heavily trabecularized cortex. For this sample the difference between the two Ct.Th estimates was particularly large (2.2 mm). AT significantly overestimated Ct.Th with respect to µCT ($p < 0.001$; mean difference between both methods: 0.28 mm). A multiple regression analysis, including the tissue acoustic impedance from SAM, did not perform better than the simple regression analysis. The following single-cycle repeatabilities were obtained: 0.32 mm for $Ct.Th_{AT}$, 2.9 % for $Ct.Po_{AT}$, 43.3 m·s^{-1} for υ_{FAS}, and 47.8 m·s^{-1} for υ_{A0}. Table 3 shows the linear correlations between the different measurement parameters.

	$Ct.Po_{\mu CT}$	$Ct.Th_{\mu CT}$	vBMD
$Ct.Po_{AT}$ (%)	0.83***	n.s.	(-) 0.80***
$Ct.Th_{AT}$ (mm)	n.s.	0.92***	n.s.
υ_{FAS} (m·s^{-1})	(-) 0.49**	n.s.	0.58***
υ_{A0} (m·s^{-1})	(-) 0.72***	0.28*	0.64***
$Ct.Po_{\mu CT}$ (%)	-	0.27*	0.77***
$Ct.Th_{\mu CT}$ (mm)	0.27*	-	n.s.
vBMD (g·cm^{-3})	0.77***	n.s.	-

Table 3. R^2 of the linear regressions between the variables. One outlier has been removed. The associations are positive unless otherwise indicated by a negative sign. n.s. = not significant. *$p < 0.05$; **$p < 0.01$; ***$p < 0.001$. N = 17

5.2 Study B – AT *in vivo*

The results from 15 out of 20 patients were used for statistical analysis. $vBMD_{pQCT}$ was best correlated with $Ct.Po_{AT}$ ($R^2 = 0.57$, $p < 0.001$) followed by υ_{FAS} ($R^2 = 0.43$, $p < 0.01$) and υ_{A0} ($R^2 = 0.28$, $p < 0.05$). Ct.Th was accurately predicted by AT after exclusion of one outlier ($R^2 = 0.90$, $p < 0.001$, RMSE = 0.19). A strong correlation between υ_{FAS} and total $vBMD$ from HR-pQCT at the ultradistal tibia was found (Spearman's rho = 0.98, $p = 0.0004$). The following single-cycle repeatabilities were obtained: 0.13 mm for $Ct.Th_{AT}$, 1.6 % for $Ct.Po_{AT}$, 25.8 m·s^{-1} for υ_{FAS} and 17.2 m·s^{-1} for υ_{A0}. Table 4 shows the linear correlations between AT and site-matched pQCT parameters.

	Ct.Th$_{pQCT}$	vBMD$_{pQCT}$
Ct.Po$_{AT}$ (%)	-	(-) 0.57***
Ct.Th$_{AT}$ (mm)	0.90***	-
υ_{FAS} (m$\cdot$s^{-1})	-	0.43***
υ_{A0} (m$\cdot$s^{-1})	0.31*	0.28*

Table 4. R² of the linear regression between parameters from AT and pQCT. One outlier has been removed. Associations are positive unless otherwise indicated by a negative sign. *p < 0.05; **p < 0.01; ***p < 0.001. N = 15.

5.3 Study C - RUS

The measured transverse isotropic stiffness tensors from 55 out of 59 specimens were used for statistical analysis. The ranges of variations of the elastic coefficients and mass densities are shown in Fig. 12a. In Fig. 12b, the shear stiffness coefficients are plotted in function of mass density in comparison with the results of two other experimental studies conducted on human femur specimens (11,45). Except for the Poisson's ratios and non-diagonal stiffness coefficients, strong linear correlations between the different elastic coefficients (0.70 < R² < 0.99) and between these coefficients and mass density (0.79 < R² < 0.89) were found.
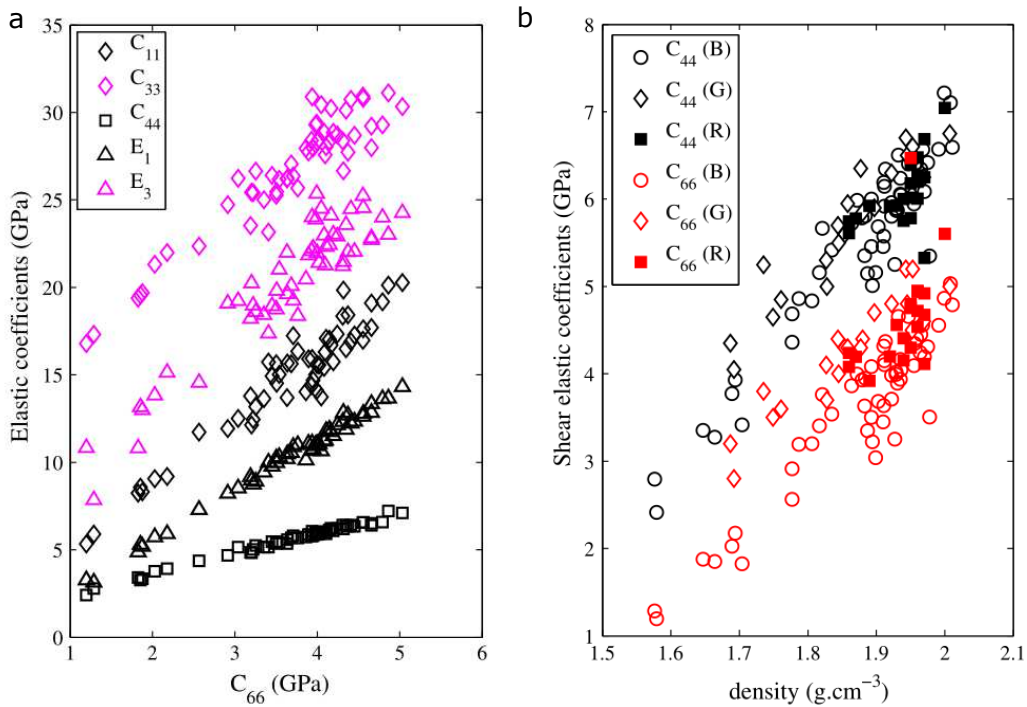
Fig. 12 (**a**) Stiffness and engineering coefficients plotted as a function of C$_{66}$ illustrating the interdependency of the different elastic coefficients. (**b**) Comparison of C$_{11}$ and C$_{66}$ from different studies: study C (B), Granke et al. (11) (G), Rudy et al. (45) (R). Reproduced with permission from Springer (46).

6 Discussion

To advance the clinical management of osteoporosis, further diagnostic tools are needed to measure skeletal factors related to fracture risk other than classical BMD. Ct.Po and Ct.Th are potential target parameters, because they were shown to be associated with hip fracture at the fracture site, i.e. femoral neck (47,48), and tibia (3). Accordingly, it was proposed to test the hypothesis that an ultrasound-based assessment of cortical bone properties at the tibia might improve the identification of patients at fracture risk. To reach this goal, a novel 500-kHz AT probe was designed and used to characterize the human tibia in terms of cortical microstructure (Ct.Po and Ct.Th) and ultrasonic velocities (v_{FAS} and v_{A0}).

An automatic signal processing has been developed in our group to estimate Ct.Po and Ct.Th from guided waves measured using the 1-MHz probe (12). In study A and B, the procedure was successfully applied to the signals of the novel 500-kHz probe. In both studies, excellent agreement was found between Ct.Th estimates and reference values (study A: $R^2 = 0.92$; study B: $R^2 = 0.90$). However, in each study one outlier had to be excluded. In study A, the outlier could be associated with a heavily trabecularized cortex visible in the µCT images. In study B, trabecularization was not observable due to the poor resolution of pQCT (500 µm voxel size). It remains unclear whether trabecularized cortical bone accurately guides ultrasound. 3D simulations of ultrasonic wave propagation in diverse geometries from µCT could provide a deeper insight into this problem. Ct.Po was accurately predicted in study A ($R^2 = 0.83$), but a bias was found depending positively on the porosity level. This bias may be associated with larger partial volume effects in the µCT reference scans for samples with higher Ct.Po. Alternatively, the bias may be related to the two-phase material model which was recently found to provide slightly biased estimates in comparison to a model based on real cortical bone microstructure (49). The discrepancy between these models increased with higher porosities, which is similar to the bias we observed in study A.

For study A and B, a novel measurement protocol was established to ensure reproducible estimates of Ct.Po and Ct.Th, particularly in the presence of soft tissue. The repeatability found *in vivo* (study B) (Ct.Th: 0.13 mm, Ct.Po: 1.6 %) was comparable to what Minonzio et al. (12) previously found *ex vivo* (Ct.Th: 0.11 mm, Ct.Po: 1.9 %). This result is promising, considering the disturbing effect of soft tissue modes on the inversion procedure. During the measurements, the main difficulty was to obtain proper experimental dispersion curves, which are mandatory for an accurate solution of the inverse problem. When the ultrasound data was acquired, the human machine interface (HMI) only visualized the experimental modes, but did not superimpose the waveguide model. This feature has recently been added to the HMI in order to better guide the operator during scanning. The updated HMI is currently being tested clinically with the 1-MHz probe at the radius by trained operators.

We accounted for inter-specimen variations in matrix stiffness and showed that the assumption of the waveguide model on uniform bone matrix stiffness among individuals is correct (study B). However, the used specimens were donated by elderly subjects without diseases known to affect the intrinsic material properties of bone tissue, such as osteogenesis imperfecta (50). The same concern would apply for children and adolescents, which are known to have a different matrix elasticity than adults. The validity of the assumption on uniform matrix stiffness needs to be confirmed also for such distinct subpopulations. Alternatively, the 2D transverse isotropic free plate model could be used without homogenization of cortical bone elasticity (43) to overcome the bone matrix assumption. The retrieved four stiffness coefficients, instead of Ct.Po, may then directly be used as cortical bone biomarkers to identify patients at fracture risk. However, the complex (5D) inverse problem has not yet been validated.

The fixed bone matrix elastic tensor used in the waveguide model was set according to Granke et al. (11). In that study, the effective elastic components of human femur specimens were retrieved from bulk wave velocity (BWV) measurements. Ct.Po was calculated from scanning acoustic microscopy (SAM). The effective elastic constants were then predicted in function of Ct.Po using a two-phase material model with fixed elastic tensors of the bone matrix (10). The fixed elastic tensor, also used in this thesis, was finally obtained by minimizing the discrepancies between the experimental and predicted elastic components. Recently, the calibration of the two-phase material model was repeated, but using the elastic data from RUS (49). The study also proposed a fast Fourier transform (FFT) homogenisation model based on real cortical bone microstructure from synchrotron µCT. Such a multiscale cortical bone model cannot be created from the RUS data of study C, because Ct.Po was not assessed. Nevertheless, the established measurement and sample preparation protocols will facilitate a follow-up RUS study including Ct.Po to build a site-specific waveguide model for the human tibia.

In conclusion, a novel 500-kHz AT probe for the clinical assessment of cortical bone parameters at human tibia was successfully validated against site-matched reference methods. For the first time, the elastic properties of the tibia were assessed using RUS, a non-destructive tool that allows one to measure large series of small cortical bone specimens conveniently. The data might be useful in the future to model ultrasonic wave propagation. The estimation of four cortical parameters (Ct.Th, Ct.Po, v_{FAS}, v_{A0}) at the tibia using the novel 500-kHz probe might advance the clinical assessment of fracture risk. Moreover, an accurate estimation of additional skeletal characteristics may allow clinicians to better select and monitor individual treatment strategies. In contrast to current clinical imaging technologies for cortical bone, such as HR-pQCT, the ultrasound device tested in this thesis is non-ionizing, compact, and affordable.

7 Outlook

Another clinical validation study could be conducted using the second generation HR-pQCT. The novel scanner is no longer restricted to the distal tibia, which would allow scanning the midshaft at 62 µm voxel size site-matched with AT. Consequently, the model-based estimates of Ct.Po could directly be compared to those from HR-pQCT. Small cortical pores may still not fully be resolved (24), but HR-pQCT currently provides the best *in-vivo* option for imaging cortical bone of human subjects.

Further work is also needed on the waveguide model. To improve the accuracy of the Ct.Th and Ct.Po estimates, the creation of a site-specific waveguide model is envisioned. In other words, the two-phase material model used in this work could be calibrated on the elastic tibia data from RUS, as it has been recently reported for the human femur (49). Another idea is to generate a more sophisticated waveguide model which accounts for the soft tissue layer. The soft tissue layer could be evaluated using additional methods, such as conventional pulse-echo imaging.

Further technical improvements could be made on the hardware side and HMI. In both studies, guided waves were not sufficiently excited in thin cortical bone (Ct.Th < 2 mm) using the novel 500-kHz probe. Capacitive micromachined ultrasonic transducers (CMUTs) might allow the design of a novel probe with a larger frequency bandwidth. Combining CMUTs with smaller receiver pitches could significantly enhance the detection of guided waves modes over a larger Ct.Th range. Finally, for a reproducible measurement it is crucial to align the probe with the main axis of the tibia. Real-time feedback on the probe alignment could be added to the HMI for a better guidance of the operator during scanning.

References

1. Teng GG, Curtis effrey R, Saag KG. Mortality and osteoporotic fractures: is the link causal, and is it modifiable? Clin Exp Rheumatol. 2008;26(5 0 51):S125-37.

2. Wainwright SA, Marshall LM, Ensrud KE, Cauley JA, Black DM, Hillier TA, Hochberg MC, Vogt MT, Orwoll ES. Hip Fracture in Women without Osteoporosis. J Clin Endocrinol Metab. 2005;90(5):2787-93. DOI: 10.1210/jc.2004-1568

3. Sundh D, Nilsson AG, Nilsson M, Johansson L, Mellström D, Lorentzon M. Increased cortical porosity in women with hip fracture. J Intern Med. 2017;281(5):496-506. DOI: 10.1111/joim.12587

4. Talmant M, Kolta S, Roux Ch, Haguenauer D, Vedel I, Cassou B, Bossy E, Laugier P. In vivo Performance Evaluation of Bi-Directional Ultrasonic Axial Transmission for Cortical Bone Assessment. Ultrasound Med Biol. 2009;35(6):912-9. DOI: 10.1016/j.ultrasmedbio.2008.12.008

5. Knapp KM, Blake GM, Fogelman I, Doyle DV, Spector TD. Multisite quantitative ultrasound: Colles' fracture discrimination in postmenopausal women. Osteoporos Int J Establ Result Coop Eur Found Osteoporos Natl Osteoporos Found USA. 2002;13(6):474-9. DOI: 10.1007/s001980200057

6. Moilanen P, Määttä M, Kilappa V, Xu L, Nicholson PHF, Alén M, Timonen J, Jämsä T, Cheng S. Discrimination of fractures by low-frequency axial transmission ultrasound in postmenopausal females. Osteoporos Int. 2012;24(2):723-30. DOI: 10.1007/s00198-012-2022-x

7. Moilanen P, Nicholson PHF, Kilappa V, Cheng S, Timonen J. Measuring guided waves in long bones: Modeling and experiments in free and immersed plates. Ultrasound Med Biol. 2006;32(5):709-19. DOI: 10.1016/j.ultrasmedbio.2006.02.1402

8. Moilanen P, Nicholson PHF, Kärkkäinen T, Wang Q, Timonen J, Cheng S. Assessment of the tibia using ultrasonic guided waves in pubertal girls. Osteoporos Int. 2003;14(12):1020-7. DOI: 10.1007/s00198-003-1528-7

9. Minonzio J-G, Foiret J, Moilanen P, Pirhonen J, Zhao Z, Talmant M, Timonen J, Laugier P. A free plate model can predict guided modes propagating in tubular bone-mimicking phantoms. J Acoust Soc Am. 2014;137(1):EL98-104. DOI: 10.1121/1.4903920

10. Parnell WJ, Vu MB, Grimal Q, Naili S. Analytical methods to determine the effective mesoscopic and macroscopic elastic properties of cortical bone. Biomech Model Mechanobiol. 2012;11(6):883-901. DOI: 10.1007/s10237-011-0359-2

11. Granke M, Grimal Q, Saïed A, Nauleau P, Peyrin F, Laugier P. Change in porosity is the major determinant of the variation of cortical bone elasticity at the millimeter scale in aged women. Bone. 2011;49(5):1020-6. DOI: 10.1016/j.bone.2011.08.002

12. Minonzio J-G, Bochud N, Vallet Q, Bala Y, Ramiandrisoa D, Follet H, Mitton D, Laugier P. Bone cortical thickness and porosity assessment using ultrasound guided waves: An ex vivo validation study. Bone. 2018;116:111-9. DOI: 10.1016/j.bone.2018.07.018

13. Minonzio J-G, Bochud N, Vallet Q, Ramiandrisoa D, Etcheto A, Briot K, Kolta S, Roux C, Laugier P. Ultrasound-based estimates of cortical bone thickness and porosity are associated with non-traumatic fractures in postmenopausal women: A pilot study. J Bone Miner Res. 2019;0(ja). DOI: 10.1002/jbmr.3733

14. Bernard S, Grimal Q, Laugier P. Accurate measurement of cortical bone elasticity tensor with resonant ultrasound spectroscopy. J Mech Behav Biomed Mater. 2013;18:12-9. DOI: 10.1016/j.jmbbm.2012.09.017

15. Rho J-Y, Kuhn-Spearing L, Zioupos P. Mechanical properties and the hierarchical structure of bone. Med Eng Phys. 1998;20(2):92-102. DOI: 10.1016/S1350-4533(98)00007-1

16. Parfitt AM. Osteonal and hemi-osteonal remodeling: The spatial and temporal framework for signal traffic in adult human bone. J Cell Biochem. 1994;55(3):273-86. DOI: 10.1002/jcb.240550303

17. Schaffler MB, Cheung W-Y, Majeska R, Kennedy O. Osteocytes: Master Orchestrators of Bone. Calcif Tissue Int. 2013;94(1):5-24. DOI: 10.1007/s00223-013-9790-y

18. Boyle WJ, Simonet WS, Lacey DL. Osteoclast differentiation and activation. Nature. 2003;423(6937):337-42. DOI: 10.1038/nature01658

19. Johnell O, Kanis JA. An estimate of the worldwide prevalence and disability associated with osteoporotic fractures. Osteoporos Int. 2006;17(12):1726-33. DOI: 10.1007/s00198-006-0172-4

20. Riggs BL, Khosla S, Melton LJ. Sex Steroids and the Construction and Conservation of the Adult Skeleton. Endocr Rev. 2002;23(3):279-302. DOI: 10.1210/edrv.23.3.0465

21. Silva BC, Leslie WD, Resch H, Lamy O, Lesnyak O, Binkley N, McCloskey EV, Kanis JA, Bilezikian JP. Trabecular Bone Score: A Noninvasive Analytical Method Based Upon the DXA Image. J Bone Miner Res. 2014;29(3):518-30. DOI: 10.1002/jbmr.2176

22. Rittweger J, Beller G, Ehrig J, Jung C, Koch U, Ramolla J, Schmidt F, Newitt D, Majumdar S, Schiessl H, Felsenberg D. Bone-muscle strength indices for the human lower leg. Bone. 2000;27(2):319-26. DOI: 10.1016/S8756-3282(00)00327-6

23. Sheu Y, Zmuda JM, Boudreau RM, Petit MA, Ensrud KE, Bauer DC, Gordon CL, Orwoll ES, Cauley JA, for the Osteoporotic Fractures in Men (MrOS) Research Group. Bone strength measured by peripheral quantitative computed tomography and the risk of nonvertebral fractures: The osteoporotic fractures in men (MrOS) study. J Bone Miner Res. 2011;26(1):63-71. DOI: 10.1002/jbmr.172

24. Ostertag A, Peyrin F, Fernandez S, Laredo JD, de Vernejoul MC, Chappard C. Cortical measurements of the tibia from high resolution peripheral quantitative computed tomography images: A comparison with synchrotron radiation micro-computed tomography. Bone. 2014;63:7-14. DOI: 10.1016/j.bone.2014.02.009

25. Zebaze R, Seeman E. Cortical Bone: A Challenging Geography. J Bone Miner Res. 2015;30(1):24-9. DOI: 10.1002/jbmr.2419

26. Langton CM, Palmer SB, Porter RW. The Measurement of Broadband Ultrasonic Attenuation in Cancellous Bone. Eng Med. 1984;13(2):89-91. DOI: 10.1243/EMED_JOUR_1984_013_022_02

27. Chappard C, Laugier P, Fournier B, Roux C, Berger G. Assessment of the relationship between broadband ultrasound attenuation and bone mineral density at the calcaneus using BUA imaging and DXA. Osteoporos Int. 1997;7(4):316-22. DOI: 10.1007/BF01623771

28. Huopio J, Kröger H, Honkanen R, Jurvelin J, Saarikoski S, Alhava E. Calcaneal ultrasound predicts early postmenopausal fractures as well as axial BMD. A prospective study of 422 women. Osteoporos Int. 2004;15(3):190-5. DOI: 10.1007/s00198-003-1534-9

29. Otani T, Fukunaga M, Yho K, Miki T, Yamazaki K, Kishimoto H, Matsukawa M, Endoh N, Hachiya H, Kanai H, Fujiwara S, Nagai Y. Attempt at standardization of bone quantitative ultrasound in Japan. J Med Ultrason. 2018;45(1):3-13. DOI: 10.1007/s10396-017-0814-5

30. Raum K. Microelastic imaging of bone. IEEE Trans Ultrason Ferroelectr Freq Control. 2008;55(7):1417-31. DOI: 10.1109/TUFFC.2008.817

31. Raum K, Reißhauer J, Brandt J. Frequency and resolution dependence of the anisotropic impedance estimation in cortical bone using time-resolved scanning acoustic microscopy. J Biomed Mater Res A. 2004;71A(3):430-8. DOI: 10.1002/jbm.a.30156

32. Lakshmanan S, Bodi A, Raum K. Assessment of Anisotropic Tissue Elasticity of Cortical Bone from High-Resolution, Angular Acoustic Measurements. IEEE Trans Ultrason Ferroelectr Freq Control. 2007;54(8):1560-70. DOI: 10.1109/TUFFC.2007.426

33. Bouxsein ML, Boyd SK, Christiansen BA, Guldberg RE, Jepsen KJ, Müller R. Guidelines for assessment of bone microstructure in rodents using micro–computed tomography. J Bone Miner Res. 2010;25(7):1468-86. DOI: 10.1002/jbmr.141

34. Ulrich D, van Rietbergen B, Laib A, Řuegsegger P. The ability of three-dimensional structural indices to reflect mechanical aspects of trabecular bone. Bone. 1999;25(1):55-60. DOI: 10.1016/S8756-3282(99)00098-8

35. Palacio-Mancheno PE, Larriera AI, Doty SB, Cardoso L, Fritton SP. 3D Assessment of Cortical Bone Porosity and Tissue Mineral Density Using High-Resolution Micro-CT: Effects of Resolution and Threshold Method. J Bone Miner Res Off J Am Soc Bone Miner Res. 2014;29(1). DOI: 10.1002/jbmr.2012

36. Bernard S, Marrelec G, Laugier P, Grimal Q. Bayesian normal modes identification and estimation of elastic coefficients in resonant ultrasound spectroscopy. Inverse Probl. 2015;31(6):065010. DOI: 10.1088/0266-5611/31/6/065010

37. Camus E, Talmant M, Berger G, Laugier P. Analysis of the axial transmission technique for the assessment of skeletal status. J Acoust Soc Am. 2000;108(6):3058-65.

38. Raum K, Leguerney I, Chandelier F, Bossy E, Talmant M, Saïed A, Peyrin F, Laugier P. Bone microstructure and elastic tissue properties are reflected in QUS axial transmission measurements. Ultrasound Med Biol. 2005;31(9):1225-35. DOI: 10.1016/j.ultrasmedbio.2005.05.002

39. Talmant M, Foiret J, Minonzio J-G. Guided Waves in Cortical Bone. Dans: Laugier P, Haïat G, directeurs. Bone Quantitative Ultrasound Chap. 7. Dordrecht: Springer Netherlands; 2011. DOI: 10.1007/978-94-007-0017-8

40. Bossy E, Talmant M, Laugier P. Bi-directional axial transmission improves accuracy and precision of ultrasonic velocity measurement in cortical bone. IEEE Trans Ultrason Ferroelectr Freq Control. 2004;51(1):71–79.

41. Minonzio J-G, Talmant M, Laugier P. Guided wave phase velocity measurement using multi-emitter and multi-receiver arrays in the axial transmission configuration. J Acoust Soc Am. 2010;127(5):2913-9. DOI: 10.1121/1.3377085

42. Minonzio J-G, Foiret J, Talmant M, Laugier P. Impact of attenuation on guided mode wavenumber measurement in axial transmission on bone mimicking plates. J Acoust Soc Am. 2011;130(6):3574. DOI: 10.1121/1.3652884

43. Bochud N, Vallet Q, Minonzio J-G, Laugier P. Predicting bone strength with ultrasonic guided waves. Sci Rep. 2017;7:43628. DOI: 10.1038/srep43628

44. Parnell WJ, Grimal Q. The influence of mesoscale porosity on cortical bone anisotropy. Investigations via asymptotic homogenization. J R Soc Interface. 2009;6(30):97-109. DOI: 10.1098/rsif.2008.0255

45. Rudy DJ, Deuerling JM, Espinoza Orías AA, Roeder RK. Anatomic variation in the elastic inhomogeneity and anisotropy of human femoral cortical bone tissue is consistent across multiple donors. J Biomech. 2011;44(9):1817-20. DOI: 10.1016/j.jbiomech.2011.04.009

46. Bernard S, Schneider J, Varga P, Laugier P, Raum K, Grimal Q. Elasticity–density and viscoelasticity–density relationships at the tibia mid-diaphysis assessed from resonant ultrasound spectroscopy measurements. Biomech Model Mechanobiol. 2016;15(1):97-109. DOI: 10.1007/s10237-015-0689-6

47. Power J, Loveridge N, Kröger H, Parker M, Reeve J. Femoral neck cortical bone in female and male hip fracture cases: Differential contrasts in cortical width and sub-periosteal porosity in 112 cases and controls. Bone. 2018;0(0). DOI: 10.1016/j.bone.2018.05.027

48. Bell KL, Loveridge N, Power J, Garrahan N, Stanton M, Lunt M, Meggitt BF, Reeve J. Structure of the femoral neck in hip fracture: cortical bone loss in the inferoanterior to superoposterior axis. J Bone Miner Res Off J Am Soc Bone Miner Res. 1999;14(1):111-9. DOI: 10.1359/jbmr.1999.14.1.111

49. Cai Xiran, Brenner Renald, Peralta Laura, Olivier Cécile, Gouttenoire Pierre-Jean, Chappard Christine, Peyrin Françoise, Cassereau Didier, Laugier Pascal, Grimal Quentin. Homogenization of cortical bone reveals that the organization and shape of pores marginally affect elasticity. J R Soc Interface. 2019;16(151):20180911. DOI: 10.1098/rsif.2018.0911

50. Weber M, Roschger P, Fratzl-Zelman N, Schöberl T, Rauch F, Glorieux FH, Fratzl P, Klaushofer K. Pamidronate does not adversely affect bone intrinsic material properties in children with osteogenesis imperfecta. Bone. 2006;39(3):616-22. DOI: 10.1016/j.bone.2006.02.071

Eidesstattliche Versicherung

„Ich, Johannes Matthias Peter Schneider, versichere an Eides statt durch meine eigenhändige Unterschrift, dass ich die vorgelegte Dissertation mit dem Thema: *Assessment of Cortical Bone Properties at the Tibia Using Axial Transmission Ultrasound (Abschätzung kortikaler Knocheneigenschaften an der Tibia mittels axialer Ultraschalltransmission)* selbstständig und ohne nicht offengelegte Hilfe Dritter verfasst und keine anderen als die angegebenen Quellen und Hilfsmittel genutzt habe. Alle Stellen, die wörtlich oder dem Sinne nach auf Publikationen oder Vorträgen anderer Autoren beruhen, sind als solche in korrekter Zitierung kenntlich gemacht. Die Abschnitte zu Methodik (insbesondere praktische Arbeiten, Laborbestimmungen, statistische Aufarbeitung) und Resultaten (insbesondere Abbildungen, Graphiken und Tabellen werden von mir verantwortet.

Meine Anteile an den ausgewählten Publikationen entsprechen denen, die in der untenstehenden gemeinsamen Erklärung mit dem Betreuer, angegeben sind. Für sämtliche im Rahmen der Dissertation entstandenen Publikationen wurden die Richtlinien des ICMJE (International Committee of Medical Journal Editors; www.icmje.og) zur Autorenschaft eingehalten. Ich erkläre ferner, dass mir die Satzung der Charité - Universitätsmedizin Berlin zur Sicherung Guter Wissenschaftlicher Praxis bekannt ist und ich mich zur Einhaltung dieser Satzung verpflichte.

Die Bedeutung dieser eidesstattlichen Versicherung und die strafrechtlichen Folgen einer unwahren eidesstattlichen Versicherung (§156,161 des Strafgesetzbuches) sind mir bekannt und bewusst.

_____

Unterschrift und Datum des Doktoranden

Anteilserklärung an den erfolgten Publikationen

Johannes Matthias Peter Schneider hatte folgenden Anteil an den folgenden Publikationen:

Study A
<u>Schneider J</u>, Iori G, Ramiandrisoa D, Hammami M, Gräsel M, Chappard C, Barkmann R, Laugier P, Grimal Q, Minonzio JG, Raum K. *Ex vivo cortical porosity and thickness predictions at the tibia using full-spectrum ultrasonic-guided wave analysis*. Archives of Osteoporosis, Jan. 2019.

Beitrag im Einzelnen (80%):

Maßgeblich verantwortlich für die axiale Transmission (AT) und akustische Mikroskopie (SAM), sowie für die Datenauswertung und Interpretation der Ergebnsisse unter Supervision durch Prof. Kay Raum und Dr. Jean-Gabriel Minonzio.

<u>Einleitung / Methodik / Ergebnisse:</u>
- Literaturrecherche
- Auswahl, Vergleich und Verifikation geeigneter statistischer Methoden unter fachlicher Unterstützung von Prof. Kay Raum. Entscheidung zur Verwendung einer multivariaten Regression und Korrelationskoeffizienten nach Pearson.
- Entwicklung eines neuen AT-Messprotokolls, mit dem Ziel die Reproduzierbarkeit der Messparameter zu verbessern (gemeinsam mit Dr. Donatien Ramiandrisoa)
- Durchführung der AT-Messungen
- Probenpräparation für SAM (gemeinsam mit Ginaluca Iori und Anke Kadow-Romacker)
- Durchführung der SAM-Messungen (gemeinsam mit Ginaluca Iori)
- Anpassung und Optimierung bestehender Auswertungsalgorithmen einer Vorgängersonde zur Messung am Radius an die neue Sonde zur Messung an der Tibia in Matlab.
- Entwicklung eines neuartigem Messverfahren für die Schallgeschwindigkeit des A_0 Modes unter fachlichlicher Unterstützung von Dr. Jean-Gabriel Minonzio in Matlab.
- Verbesserung eines bestehenden Messverfahrens für die Schallgeschwindigkeit des First Arriving Signals in Matlab unter fachlicher Unterstützung von Prof. Kay Raum.

<u>Diskussion:</u>
- Interpretation und Diskussion der gewonnenen Daten mit fachlicher Unterstützung von Prof. Kay Raum und Dr. Jean-Gabriel Minonzio in enger Zusammenarbeit mit den Ko-Autoren

<u>Manuskript:</u>
- Visuelle Aufarbeitung der Ergebnisse
- Initialer Entwurf des gesamten Manuskripts und eigenständige Überarbeitung auf Basis der Begutachtungen der Ko-Autoren und im Rahmen des Review-Prozesses

Study B
<u>Schneider J</u>, Ramiandriosa D, Armbrecht G, Ritter Z, Felsenberg D, Raum K, Minonzio JG. *In Vivo Measurements of Cortical Thickness and Porosity at the Proximal Third of the Tibia Using Guided Waves: Comparison with Site-Matched Peripheral Quantitative Computed Tomography and Distal High-Resolution Peripheral Quantitative Computed Tomography*. UMB, Jan. 2019.

Beitrag im Einzelnen (80%):

Maßgeblich verantwortlich für die axiale Transmission (AT) sowie für die Datenauswertung und Interpretation der Ergebnisse unter Supervision durch Dr. Jean-Gabriel Minonzio.

Einleitung / Methodik / Ergebnisse:
- Literaturrecherche
- Auswahl und Rekrutierung der Patienten (gemeinsam mit Dr. Gabriele Armbrecht)
- Durchführung der Ultraschallmessungen am CBF (AT)
- Optimierung der bestehenden Algorithmen zur Auswertung der AT-Messdaten in Matlab mit dem Ziel den Einfluss vom Weichgewebe zu kompensieren.
- Auswahl, Vergleich und Verifikation geeigneter statistischer Methoden unter fachlicher Unterstützung von Prof. Kay Raum und Dr. Jean-Gabriel Minonzio

Diskussion:
- Interpretation und Diskussion der gewonnenen Daten mit fachlicher Unterstützung von Dr. Jean-Gabriel Minonzio in enger Zusammenarbeit mit den Ko-Autoren

Manuskript:
- Visuelle Aufarbeitung der Ergebnisse
- Initialer Entwurf des gesamten Manuskripts und eigenständige Überarbeitung auf Basis der Begutachtungen der Ko-Autoren und im Rahmen des Review-Prozesses

---

Study C
Bernard S, <u>Schneider J</u>, Varga P, Laugier P, Raum K, Grimal Q. *Elasticity–density and viscoelasticity–density relationships at the tibia mid-diaphysis assessed from resonant ultrasound spectroscopy measurements*. Biomechanics and Modeling in Mechanobiology, May 2015.

Beitrag im Einzelnen (30%):
Maßgeblich verantwortlich für die Entwicklung des Probennahmeprotokolls und für die Probenpräparation unter Supervision durch Prof. Quentin Grimal und Prof. Kay Raum.

Einleitung / Methodik / Ergebnisse:
- Entwicklung des Probennahmeprotokolls in enger Zusammenarbeit mit den Ko-Autoren
- Probennahme und Bestimmung der Massendichte
- Datenauswertung in Matlab (gemeinsam mit Dr. Simon Bernard)

Manuskript:
- Begutachtung des Manuskripts

Unterschrift und Datum des Doktoranden

Journal Data Filtered By: **Selected JCR Year: 2017** Selected Editions: SCIE,SSCI Selected Categories: **"ORTHOPEDICS"** Selected Category Scheme: WoS
Gesamtanzahl: 77 Journale

Rank	Full Journal Title	Total Cites	Journal Impact Factor	Eigenfactor Score
1	AMERICAN JOURNAL OF SPORTS MEDICINE	32,251	6.057	0.041740
2	OSTEOARTHRITIS AND CARTILAGE	15,911	5.454	0.026630
3	JOURNAL OF BONE AND JOINT SURGERY-AMERICAN VOLUME	46,966	4.583	0.044930
4	Journal of Physiotherapy	839	4.542	0.002390
5	ARTHROSCOPY-THE JOURNAL OF ARTHROSCOPIC AND RELATED SURGERY	15,568	4.330	0.020760
6	CLINICAL ORTHOPAEDICS AND RELATED RESEARCH	40,313	4.091	0.037880
7	Bone & Joint Journal	4,676	3.581	0.019010
8	JOURNAL OF ORTHOPAEDIC RESEARCH	14,800	3.414	0.016570
9	JOURNAL OF ARTHROPLASTY	16,901	3.338	0.029760
10	KNEE SURGERY SPORTS TRAUMATOLOGY ARTHROSCOPY	14,017	3.210	0.026090
11	Spine Journal	8,564	3.119	0.019380
12	JOURNAL OF ORTHOPAEDIC & SPORTS PHYSICAL THERAPY	6,612	3.090	0.006800
13	Acta Orthopaedica	8,583	3.076	0.008670
14	JOURNAL OF SHOULDER AND ELBOW SURGERY	12,263	2.849	0.017730
15	SPINE	46,984	2.792	0.035050
16	ORTHOPEDIC CLINICS OF NORTH AMERICA	3,140	2.672	0.003050
17	FOOT & ANKLE INTERNATIONAL	8,682	2.653	0.008190
18	Journal of Hand Surgery-European Volume	4,234	2.648	0.004220
19	JOURNAL OF THE AMERICAN ACADEMY OF ORTHOPAEDIC SURGEONS	5,082	2.638	0.007810
20	EUROPEAN SPINE JOURNAL	15,242	2.634	0.023050

Rank	Full Journal Title	Total Cites	Journal Impact Factor	Eigenfactor Score
21	Cartilage	653	2.621	0.001590
22	CONNECTIVE TISSUE RESEARCH	2,195	2.608	0.002310
23	PHYSICAL THERAPY	11,858	2.587	0.008870
24	Archives of Osteoporosis	860	2.382	0.002840
25	JOURNAL OF ORTHOPAEDIC TRAUMA	8,271	2.381	0.010090
26	INTERNATIONAL ORTHOPAEDICS	9,173	2.377	0.017140
27	Bone & Joint Research	730	2.362	0.003010
28	JOURNAL OF SPINAL DISORDERS & TECHNIQUES	4,715	2.310	0.005440
29	GAIT & POSTURE	12,927	2.273	0.016950
30	CLINICAL JOURNAL OF SPORT MEDICINE	3,683	2.224	0.004470
31	INJURY-INTERNATIONAL JOURNAL OF THE CARE OF THE INJURED	13,720	2.199	0.019980
32	Journal of Knee Surgery	1,406	2.079	0.003260
33	Journal of Orthopaedic Translation	180	2.078	0.000430
34	BMC MUSCULOSKELETAL DISORDERS	8,804	1.998	0.020980
35	Clinical Spine Surgery	406	1.987	0.001450
36	ARCHIVES OF ORTHOPAEDIC AND TRAUMA SURGERY	6,108	1.967	0.009570
37	KNEE	4,191	1.903	0.008430
38	CLINICAL BIOMECHANICS	8,064	1.863	0.008750
39	JOURNAL OF PEDIATRIC ORTHOPAEDICS	6,783	1.853	0.007670
40	JOURNAL OF HAND SURGERY-AMERICAN VOLUME	10,191	1.776	0.011220
41	Brazilian Journal of Physical Therapy	1,247	1.699	0.001820
42	Journal of Foot and Ankle Research	892	1.683	0.001990
43	Journal of Orthopaedic Surgery and Research	1,695	1.610	0.004430
44	SKELETAL RADIOLOGY	5,482	1.567	0.007550
45	PHYSICIAN AND SPORTSMEDICINE	1,124	1.545	0.001690

ORIGINAL ARTICLE

CrossMark

Ex vivo cortical porosity and thickness predictions at the tibia using full-spectrum ultrasonic guided-wave analysis

Johannes Schneider[1] · Gianluca Iori[1] · Donatien Ramiandrisoa[2,3] · Maroua Hammami[2] · Melanie Gräsel[4] ·
Christine Chappard[5] · Reinhard Barkmann[4] · Pascal Laugier[2] · Quentin Grimal[2] · Jean-Gabriel Minonzio[2,6] · Kay Raum[1]

Abstract

Summary The estimation of cortical thickness (Ct.Th) and porosity (Ct.Po) at the tibia using axial transmission ultrasound was successfully validated ex vivo against site-matched micro-computed tomography. The assessment of cortical parameters based on full-spectrum guided-wave analysis might improve the prediction of bone fractures in a cost-effective and radiation-free manner.

Purpose Cortical thickness (Ct.Th) and porosity (Ct.Po) are key parameters for the identification of patients with fragile bones. The main objective of this ex vivo study was to validate the measurement of Ct.Po and Ct.Th at the tibia using a non-ionizing, low-cost, and portable 500-kHz ultrasound axial transmission system. Additional ultrasonic velocities and site-matched reference parameters were included in the study to broaden the analysis.

Methods Guided waves were successfully measured ex vivo in 17 human tibiae using a novel 500-kHz bi-directional axial transmission probe. Theoretical dispersion curves of a transverse isotropic free plate model with invariant matrix stiffness were fitted to the experimental dispersion curves in order to estimate Ct.Th and Ct.Po. In addition, the velocities of the first arriving signal (v_{FAS}) and A_0 mode (v_{A0}) were measured. Reference Ct.Po, Ct.Th, and vBMD were obtained from site-matched micro-computed tomography. Scanning acoustic microscopy (SAM) provided the acoustic impedance of the axial cortical bone matrix.

Results The best predictions of Ct.Po ($R^2 = 0.83$, RMSE = 2.2%) and Ct.Th ($R^2 = 0.92$, RMSE = 0.2 mm, one outlier excluded) were obtained from the plate model. The second best predictors of Ct.Po and Ct.Th were vBMD ($R^2 = 0.77$, RMSE = 2.6%) and v_{A0} ($R^2 = 0.28$, RMSE = 0.67 mm), respectively.

Conclusions Ct.Th and Ct.Po were accurately predicted at the human tibia ex vivo using a transverse isotropic free plate model with invariant matrix stiffness. The model-based predictions were not further enhanced when we accounted for variations in axial tissue stiffness as reflected by the acoustic impedance from SAM.

Keywords Acoustic microscopy · Axial transmission ultrasound · Cortical bone porosity · Guided waves · Micro-computed tomography

✉ Johannes Schneider
   johannes.schneider@charite.de

1   Berlin-Brandenburg School for Regenerative Therapies (BSRT),
    Charité - Universitätsmedizin Berlin, Augustenburger Platz 1,
    13353 Berlin, Germany

2   Laboratoire d'Imagerie Biomédicale (LIB), CNRS, INSERM,
    Sorbonne University, 15, rue de l'école de médecine,
    75006 Paris, France

3   BleuSolid, 29, rue Beauséjour, 77400 Pomponne, France

4   Molecular Imaging North Competence Center (MOIN),
    Universitätsklinikum Schleswig-Holstein, Am Botanischen Garten
    14, 24118 Kiel, Germany

5   Osteo-Articular Bioengineering and Bioimaging (B2OA), CNRS,
    INSERM, University Denis Diderot, 10, Avenue de Verdun,
    75010 Paris, France

6   Escuela de Ingeniería Civil en Informática, Universidad de
    Valparaíso, General Cruz 222, Valparaíso, Chile

Springer

Introduction

In postmenopausal women, the majority of bone is lost from the cortical bone compartment as a result of both reduced cortical thickness (Ct.Th) and increased cortical porosity (Ct.Po) [1]. Both parameters can be measured in vivo with high-resolution peripheral quantitative computed tomography (HR-pQCT) and were recently shown to be associated with a higher prevalence of hip fractures [2]. However, this novel imaging technology is still rarely available and based on ionizing radiation. Alternatively, quantitative ultrasound (QUS) techniques are being developed, which are non-ionizing, low cost, and portable. For example, a simple ultrasonic pulse-echo measurement was proposed to predict Ct.Th, but the ultrasonic wave-speed in the cortical bone layer was assumed to be known [3].

Modern ultrasound axial transmission (AT) measures the dispersion curves of guided waves, which propagate in the cortical shell of long bones [4]. In early AT applications, isotropic tube models were fitted to the dispersion curves, providing Ct.Th ex vivo at the human radius [5] and bovine tibia [6]. Subsequently, a transverse isotropic free plate model was proposed, the use of which allowed estimating Ct.Th and four bone elastic coefficients at the same time [7]. The unknown coefficients of this plate model were then reduced to Ct.Th and Ct.Po [8]. To build such a model, asymptotic homogenization [9] has been applied to estimate the effective stiffness tensor as a function of porosity, assuming an invariable stiffness of the tissue matrix. However, the mineralization of the bone tissue matrix in humans, intimately related to the stiffness, is not constant, but affected by age [10], gender [11], treatment, and disease [12].

In the beginning of its development, AT has extensively been used to measure the first arriving signal velocity (v_{FAS}) in the cortex of the radius and tibia. The first arriving signal measured at low frequencies has a larger penetration depth than at high frequencies. Thus, it can capture features of deeper cortical bone layers in which disease-associated changes usually start to occur [13]. Accordingly, low-frequency v_{FAS} (200 kHz) measured at the tibia was significantly correlated with Ct.Th (R = 0.24, $p < 0.001$), whereas high-frequency v_{FAS} (1.25 MHz) was not [14]. The ability of v_{FAS} to discriminate subjects with osteoporotic fractures from non-fractured controls was shown to be similar [15] or inferior [16, 17] when compared to areal bone mineral density (aBMD) measured by dual-energy X-ray absorptiometry (DXA) at the hip or spine. DXA is considered the current standard method for osteoporosis diagnosis and fracture risk prediction.

In an attempt to provide complementary parameters to v_{FAS} with improved fracture discrimination ability, researchers also considered the phase velocity of the A_0 mode (v_{A0}) [18, 19]. A_0 is a fundamental flexural guided wave, which propagates within the cortical bounds and is particularly sensitive to both Ct.Th and to pathological changes in the endosteal region

depending on the frequency-thickness ratio regime [20]. Following these findings, an ex vivo study at the radius showed significant correlations of v_{A0} with Ct.Th ($R^2 = 0.52$, $p < 0.001$) and with volumetric bone mineral density (vBMD) ($R^2 = 0.45$, $p < 0.001$) [21]. However, when investigated in vivo at the tibia, the correlations between both v_{A0} and vBMD and v_{A0} and Ct.Th were less strong [14]. According to the authors, the correlations decreased due to interferences with the soft tissue, in which ultrasound propagates at similar velocities ($\sim 1500\ \mathrm{m\,s}^{-1}$) as the A_0 mode in cortical bone [22].

In this ex vivo study, we predicted Ct.Th and Ct.Po at the human tibia using a model-based inversion method which was previously proposed by our group for a similar 1-MHz radius probe [23]. To account for the difference in Ct.Th between the tibia and radius, a novel probe was designed to optimize the excitation of guided waves in the Ct.Th range usually found in humans at the diaphysis of the tibia. Compared to the former radius probe, the central frequency is reduced from 1.0 to 0.5 MHz, whereas the probe dimensions are slightly increased. Cortical bone samples were extracted from the region below the receiver array for $Ct.Po_{\mu CT}$ reference measurements using high-resolution micro-computed tomography (μCT, 7.4 μm isotropic voxel size). Site-matched reference $Ct.Th_{\mu CT}$ and vBMD were obtained from a larger μCT scan at lower resolution (39 μm isotropic voxel size). In addition, we assessed the acoustic impedance (a surrogate for matrix stiffness) using scanning acoustic microscopy (SAM) to evaluate the assumption of a waveguide model with invariant matrix stiffness. The ultrasonic velocities v_{FAS} and v_{A0} were measured and compared to site-matched cortical bone properties.

Methods

Bone samples

Nineteen left tibia specimens without soft tissue from human cadavers (6 male, 13 female, age 69–94 years, mean 83.7 ± 8.4 years) were provided by the Institute of Anatomy, University of Lübeck. The sample collection was obtained in accordance with the German law "*Gesetz über das Leichen-, Bestattungs- und Friedhofswesen des Landes Schleswig-Holstein, Abschnitt II, § 9 Leichenöffnung, anatomisch*" from 04.02.2005. All specimens were received without distal ends (cut off at approximately 50%) and stored at $-20\ °C$.

Axial transmission ultrasound

Experimental system

The axial transmission (AT) system (Azalée, Paris, France) included a custom-made probe (Vermon, Tours, France),

driving electronics (Althais, Tours, France), and a human-machine interface (BleuSolid, Paris, France). The multi-channel probe consisted of a central 24-receiver array (pitch = 1.2 mm) and two lateral 5-emitter arrays (pitch = 1.5 mm). The dimensions of each rectangular receiver and emitter element were 1.2×13 mm^2 and 1.5×13 mm^2, respectively. A distance of 8 mm separated the receiver from each emitter array. This configuration enabled the propagation of ultrasound in two opposite directions, a technique used to correct errors induced by small inclination angles between the probe and the bone surface [24]. The excitation signal consisted of a wideband pulse with a center frequency of 500 kHz (-6 dB frequency bandwidth from 0.3 to 0.7 MHz). The five multi-element transmitters were used successively with time delays ranging from 0 to 0.8 μs. After 16 averages performed by the hardware, a set of 120 radio-frequency (RF) signals corresponding to all possible transmission-receiver pairs were digitized (12 bits, 20 MHz, 1024 samples) for each propagation direction.

Measurement protocol

Measurements were performed in water at room temperature (21 °C) (Fig. 1a). The probe was placed in contact with the specimens at the medial surface of the tibia (*facies medialis*) above the medullary cavity. The edge of the probe was aligned

with (i) the distal cut plane and (ii) the long main axis of the bone. The protocol required the acquisition of three cycles of 400 successive measurements. During each cycle, the probe was slowly tilted in both circumferential directions (arrow in Fig. 1a) to scan a wide region above the medullary cavity. Between the cycles, the probe was removed from the water bath and repositioned. At each measurement, 120 RF signals (5 × 24) were acquired from each propagation direction. The scan time per cycle was about 3 min.

Cortical porosity and thickness estimation

Cortical thickness (Ct.Th) and porosity (Ct.Po) were estimated by fitting a transverse isotropic free plate model (Fig. 2) to the measured guided wave dispersion curves in line with Minonzio et al. [23]. Briefly, the recorded time signals were transformed to the frequency-wavenumber (*f-k*) space using a singular value decomposition (SVD) enhanced two-dimensional spatiotemporal Fourier transform. This signal processing step provided the so-called *Norm function* of which each pixel (*f, k*) reflects the presence rate of a guided wave mode in a 0 to 1 scale [4]. Subsequently, a transverse isotropic free plate model was fitted to the maxima of the *Norm function* (Fig. 3c). A plate model was used since effects from the bone's curvature can be neglected [25]. The model
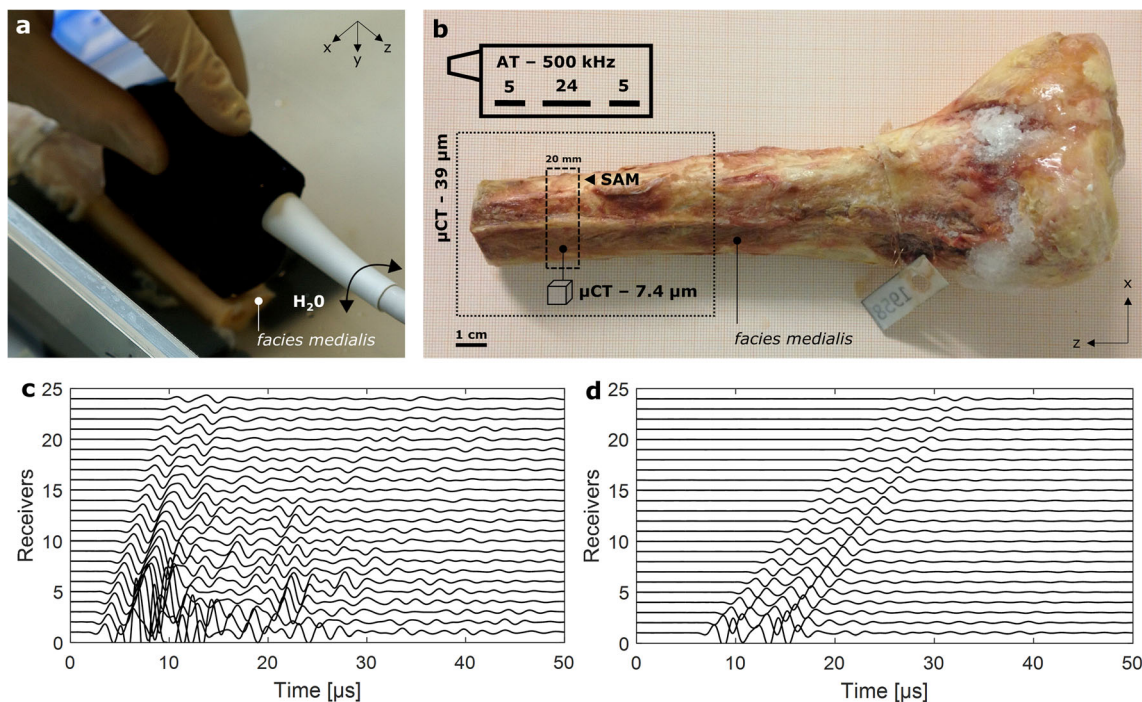
Fig. 1 **a** 500-kHz axial transmission (AT) multi-channel probe positioned on the *facies medialis* and aligned with the z-axis of a tibia specimen. The arrow indicates the movement of the probe during the acquisition of 400 individual measurements. **b** *Top left* sketch of probe showing the number and positions of central receivers and adjacent lateral emitters. The distal ends of each tibia (pointed line box) were imaged using micro-computed tomography (μCT, 39 μm isotropic voxel size). A cross-section (dashed line box) was extracted from the AT measurement region. The proximal surface of the cross-section was scanned with 100-MHz scanning acoustic microscopy (SAM). A parallelepiped sample of around $2 \times 3 \times 4$ mm^3 was obtained from the *facies medialis* of this cross-section and imaged with μCT (7.4 μm isotropic voxel size). Typical waveforms acquired after one ultrasound transmission at the tibia ex vivo (**c**) and in a water tank of 65 mm depth (**d**)
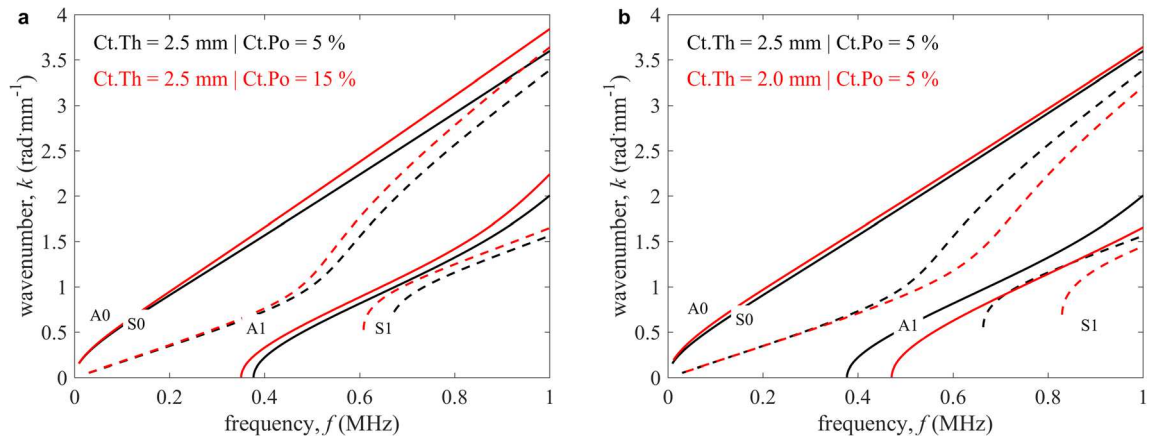
Fig. 2 Dispersion curves of the transverse isotropic free plate model with homogenized elastic properties in the frequency-wavenumber (*f-k*) space. **a** Constant cortical thickness (Ct.Th) (2.5 mm) with varying cortical porosity (Ct.Po) (5 and 15%). **b** Constant Ct.Po (5%) with varying Ct.Th (2.5 and 2.0 mm). Antisymmetric (A) and symmetric (S) modes are represented as continuous and dashed lines, respectively

required four elastic coefficients, the mass density, and the thickness of the waveguide. Granke et al. suggested that in aged women, changes in Ct.Po account for most of the bone's mesoscopic elasticity variations [26]. We used thus a micro-mechanical model [9] to calculate a set of effective mesoscale stiffness tensors for a set of porosity values assuming that transverse isotropic elastic coefficients ($c_{11} = 26.8$ GPa, $c_{13} = 15.3$ GPa, $c_{33} = 35.1$ GPa, and $c_{55} = 7.3$ GPa) and mass density ($\rho = 1.91$ g·cm^{-3}) for the tissue matrix are invariant [26]. Then, the predicted mesoscale stiffness tensors were
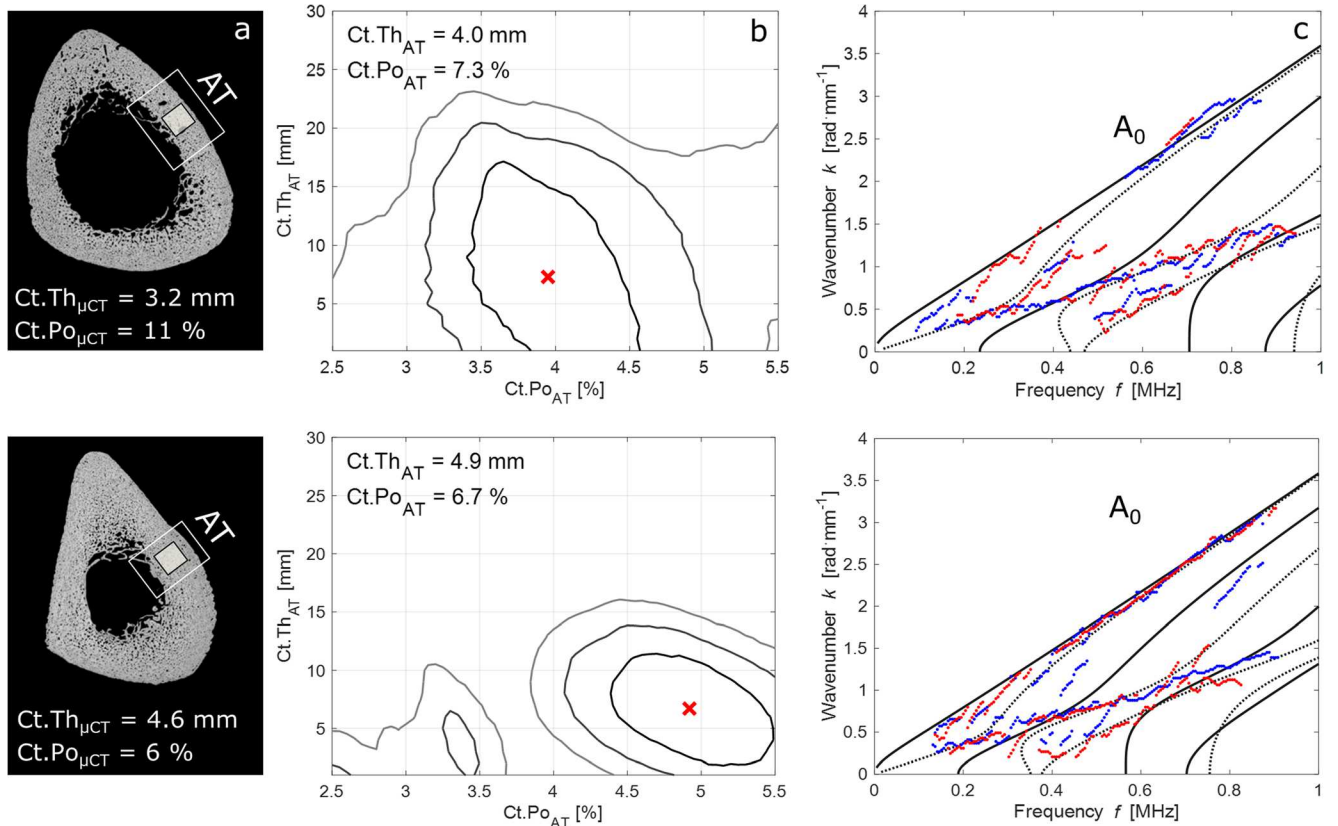
Fig. 3 **a** 100-MHz scanning acoustic microscopy (SAM) images with 12 μm pixel size, showing the axial transmission (AT) measurement region. The cortical thickness (Ct.Th) below the probe was measured using μCT with 39 μm voxel size. The black square indicates the region from which a parallelepiped sample was extracted for cortical porosity (Ct.Po) measurements using μCT with 7.4 μm voxel size. **b** Contour plot representations of the objective functions with global maxima (crosses) corresponding to the best fit between the waveguide model and experimental dispersion curves (**c**). Continuous and dashed lines represent antisymmetric and symmetric modes, respectively. Red and blue dotted lines correspond to the experimental dispersion curves obtained from bi-directional guided wave measurements

used to create a database of dispersion curves for a combination of porosity and thickness values. The thickness ranged from 2.5 to 5.5 mm with intervals of 0.1 mm and the porosity from 1 to 25% with intervals of 1%. Figure 2 shows the effect of changes in Ct.Th and Ct.Po on the modeled dispersion curves. Ct.Po mainly modifies the slope of the curves in the *f-k* space (a), whereas the curves shift towards lower frequencies with increasing Ct.Th (b).

To find the best fit between the plate model and the experimental dispersion curves (Fig. 3c), the model database was projected onto the singular vector basis $U(f)$ of the *Norm function*. Accordingly, the objective function is denoted as

$Proj(Ct.Th, Ct.Po)$

$$= \frac{1}{fmax - fmin} \int_{fmin}^{fmax} \sum_{m=1}^{M} \|e^{test}(km(f, Ct.Th, Ct.Po))\|_{U(f)}^2 df, \tag{1}$$

where f_{min} and f_{max} correspond to the frequency bandwidth limits, M denotes the number of theoretical guided modes, and e^{test} the testing vector being a normalized attenuated plane wave. Figure 3b shows contour plot representations of the objective function with the global maxima corresponding to the fitted models in Fig. 3c. Due to ill conditioning of the objective function, i.e., incomplete experimental dispersion curves, often more than one local maxima was obtained. To remove this model ambiguity, we compared the two highest local maxima for each of the 400 successive measurements: when the highest maximum (global) exceeded the second highest of at least 3%, this was considered to be a valid solution to the problem. The threshold was empirically chosen based on a tradeoff between the standard deviation of the Ct.Th/Ct.Po estimates and the total number of valid measurements per measurement cycle. If at least 10 of the 400 successive measurements produced a valid parameter pair, the medians of the Ct.Th/Ct.Po estimates were calculated. Otherwise, the entire measurement cycle would have been rejected. Finally, if at least two out of three cycles were valid, the medians of these valid cycles were averaged for every specimen. Otherwise, the entire measurement series for that sample would have been rejected.

Estimation of the first arriving signal velocity

The velocity of the first arriving signal (v_{FAS}) was calculated based on a bi-directional measurement [27]. Briefly, the time of flight was determined for each emitter-receiver distance using the first extremum of the signal in the time domain. The sound velocity was derived from the inverse slope of a linear fit through these time points plotted against the known emitter-receiver distances. This procedure was performed for each of the five transmissions and from both directions to account for small inclination angles between the probe and the bone

surface. It was previously shown that larger probe inclination angles increase the relative measurement error of v_{FAS} [28]. Accordingly, bi-directional measurements for which the absolute difference between the two opposite velocities exceeded 50 m s^{-1} were eliminated [29]. Ideally, a measurement provided five corrected velocities, corresponding to the five bi-directional ultrasound transmissions per measurement, which were then averaged. Histograms of the corrected velocities were obtained for each measurement cycle. For each specimen, the v_{FAS} was calculated as the average of the three histogram peaks.

Estimation of the A_0 mode velocity

The A_0 mode phase velocity (v_{A0}) was calculated in the frequency-domain based on SVD-enhanced 2D Fourier transforms of the acquired multi-dimensional radiofrequency signals. The principal signal processing steps are illustrated in Online Resource 1. First, the *Norm function* was converted from the frequency-wavenumber (*f-k*) into the frequency-phase velocity (*f-cp*) domain ($cp = 2\pi f/k$) [30]. Afterwards, the A_0 mode was extracted using a fixed frequency (0.5 to 0.8 MHz) and c_p range (1400 to 1900 m s^{-1}). Inside this window, the amplitudes of the *Norm function* were averaged over frequency generating a characteristic single-peaked function of which the maximum was defined as uni-directional velocity v_{A0}. For each individual measurement of a cycle, the harmonic mean of the two bi-directional velocities was calculated to correct for inclination angles between the probe and bone surface [28]. Unstable measurements for which the absolute difference between two opposite velocities was larger than 50 m s^{-1} were eliminated [15]. The final velocity v_{A0} of a tibia specimen was calculated by averaging the peak values of the velocity histograms obtained for each cycle.

Reference measurements

Micro-computed tomography—39 μm

Micro-computed tomography (μCT) with 39 μm isotropic voxel size was used to measure cortical thickness ($Ct.Th_{\mu CT}$) and vBMD. The proximal epiphyses were removed with a hand saw to fit the frozen shaft specimens into a custom-made thermo-isolated plastic tube. The tube containing the specimen was filled with dry ice and scanned with the μCT system (VivaCT 80, Scanco Medical, Brüttisellen, Switzerland). Before scanning, the bone's longitudinal axis was aligned with the rotation axis of the sample holder. The diameter of the field of view was 50 mm, allowing the imaging of the entire shaft cross-section. Source voltage and current were set at 70 kV and 114 μA, respectively. Five hundred projections were acquired over a range of 360° using an integration time of 200 m s. A filtered back-projection reconstruction was used to obtain stacks of 1850 slices with an isotropic voxel size of

39 μm. The gray values of the images were transformed into mgHA·cm^{-3} based on a calibration procedure provided by the scanner vendor. The bone region insonified by AT was extracted from the μCT stack (approximately 30 mm, equivalent to 795 slices) and first binarized using Otsu's method [31]. After this, the cortical bone compartment was automatically segmented applying the algorithm proposed by Burghardt et al. [32]. The radius of the structuring element for morphological closing of the mask was set to 0.03 mm. A manual correction was needed for one sample which had the highest $Ct.Po_{\mu CT}$ (22%). $vBMD$ was defined as the mean mineralization value for all voxels in the cortical compartment at the medial portion of the tibia and above the medullary canal. Ct.Th was calculated in that region as the minimum distance between endosteal and periosteal surfaces [33].

Scanning acoustic microscopy

Scanning acoustic microscopy (SAM) provided the acoustic impedance (Z_{SAM}) of the cortical bone matrix. Cross sections of approximately 20 mm thickness were extracted from the diaphysis, site-matched with the region of the AT receiver array (Fig. 1b). Of each section, the proximal surface was polished using a planar grinder (Phoenix 4000, Buehler Ltd., Illinois) at constant speed (50 rpm) and decreasing grain size (ISO/FEPA grit: P80, P600, P1200, P2500, and P4000, Buehler Ltd., Illinois). Subsequently, the samples were washed and degassed for approximately 30 min. The custom-made microscope and scanning procedure have been described in detail elsewhere [34]. Briefly, a 100-MHz spherically focused transducer was used (KSI 100/60°, Krämer Scientic Instruments, Herborn, Germany) which had a −6-dB bandwidth at the confocal pulse echo between 84.4 and 100.7 MHz. The −6-dB depth of focus and lateral beam diameter in the focal plane were 139 and 19.8 μm, respectively [35]. The samples were immersed in a temperature-controlled tank with a 25 °C degassed 1% PBS solution. Images were acquired by moving the transducer along the x-y-plane with a scan increment of 12 μm. The scan time was up to 5 h. A defocus correction was applied before the images were converted into acoustic impedance maps (Fig. 3a) using calibration materials (PMMA and titanium). The cortical compartment was obtained by drawing the endosteal boundary manually (following the rules proposed by Malo et al. [10]) whereas the periosteal boundary was detected automatically by morphological region filling and tracing of the contour on the segmented image. Segmentation was performed using an adaptive threshold as described by Lakshmanan et al. [36]. The acoustic impedance (Z_{SAM}) was calculated as the mean impedance value of all bone tissue pixels within the cortical compartment at the medial portion of the tibia and above the medullary canal. Z_{SAM} was converted into the stiffness coefficient c_{33} using a non-linear regression function [37].

Micro-computed tomography—7.4 μm

Rectangular parallelepiped samples of cortical bone were harvested from the cross sections, previously scanned with SAM (Fig. 3a), for the characterization of cortical porosity ($Ct.Po_{\mu CT}$). The typical sample size was $2 \times 3 \times 4$ mm^3. Cutting was performed using a precision linear saw (Isomet 4000, Buehler GmbH, Düsseldorf, Germany). In the desktop μCT system (Skyscan 1172, Bruker MicroCT, Kontich, Belgium), the samples were positioned so that the anatomical vertical axis was aligned with the rotation axis of the sample holder. A source voltage of 80 kV, a current of 100 μA, and steps of 0.3° over 180° rotation were used. The exposure time for each frame was 320 ms. Twenty frames were averaged leading to a total scan time of 60 min per sample. A 0.5-mm-thick aluminum filter reduced beam hardening artifacts. Images were saved as 16-bit TIFF files and reconstructed using a filtered back-projection algorithm (NRecon, V1.6.10.4, Skyscan NV, Kontich, Belgium) with 20% ring artifact correction. For each parallelepiped sample, a stack of 650 sections was reconstructed with a 1968 × 1968 pixel field of view and 7.4 μm isotropic voxel size. Further post-processing was performed using the software CTan (V1.16.1.0, Skyscan NV, Kontich, Belgium). To separate the sample from the background, a semi-automatic procedure was performed, based on manual contouring on a selected number of slices, and followed by interpolation. A Gaussian 2D filter (R = 1) was applied to the images which were then segmented using the Otsu's method [31]. Finally, in a 3D analysis, the tissue volume (TV), pore volume (PV), and cortical porosity (Ct.Po = PV / TV * 100%) were calculated.

Statistical analysis

The normality of the distributions of the derived parameters was verified with Shapiro-Wilk tests. Linear regression analysis and Pearson's correlation coefficients were used to quantify the degree of association between parameters obtained from AT, SAM, and μCT. Bland-Altman plots were used to reveal biases in the prediction of $Ct.Po_{\mu CT}$ and $Ct.Th_{\mu CT}$. Differences between the means were tested either with paired t tests or Wilcoxon signed-rank tests in case the data was not normally distributed. Correlations were considered statistically significant for p values lower than 0.05. Stepwise multiple regression analysis was applied to evaluate the optimal combination of parameters to predict $Ct.Po_{\mu CT}$ and $Ct.Th_{\mu CT}$. The single-cycle repeatability of the AT measurement parameters ($Ct.Th_{AT}$, $Ct.Po_{AT}$, v_{FAS}, v_{A0}) was estimated using the root-mean-square average of the standard deviation [38] obtained from at least two repeated cycles. Unless stated otherwise, all image processing and statistical analysis were performed using MATLAB (R2017a, The MathWorks Inc., Natick, MA, USA).

Results

The results from 17 out of 19 specimens were used for statistical analysis. Two samples (Fig. 5a, b) were excluded due to large deviations of the ultrasonic measurements between the cycles. The distributions of the parameters were normal after logarithm transformation except for $vBMD$ ($p = 0.004$). Between both groups, no statistically significant differences were found for all parameters. The single-cycle repeatability was 0.32 mm for $Ct.Th_{AT}$, 2.9% for $Ct.Po_{AT}$, 43.3 m$\cdot$s^{-1} for v_{FAS}, and 47.8 m$\cdot$s^{-1} for v_{A0}. Table 1 shows the results and correlations between the different measurement parameters.

Prediction of cortical porosity

The best predictor for cortical porosity ($Ct.Po_{\mu CT}$) was $Ct.Po_{AT}$ ($R^2 = 0.83$, $p < 0.001$, RMSE = 2.2%, Fig. 4c). The difference between the estimates of the two methods was not statistically significant. Figure 4d shows the according Bland-Altman plot which suggests a bias of Ct.Po that depends positively on the porosity level. This effect was also reflected in the slope of the linear regression (Fig. 4c) which, however, was not statistically different from 1 (confidence interval 1.00–1.68).

Prediction of cortical thickness

$Ct.Th_{\mu CT}$ was best predicted by $Ct.Th_{AT}$ ($R^2 = 0.92$, $p < 0.001$, RMSE = 0.20 mm) after removal of one sample with a heavily trabecularized cortex (Fig. 5c). For this sample, the difference between the two Ct.Th estimates was particularly large (2.2 mm); approximately five times larger than the 95% confidence interval at ± 1.96 SD (0.4 mm, Fig. 4b). Figure 5c suggests that ultrasonic guided waves may also propagate in the trabecularized bone region (red line) which in the μCT images was not considered to belong to the cortical compartment (green). Moreover, AT significantly overestimated Ct.Th with respect to μCT ($p < 0.001$; mean difference between both methods 0.28 mm). The second best predictor of $Ct.Th_{\mu CT}$ was v_{A0} ($R^2 = 0.29$, $p = 0.031$, RMSE = 0.59 mm). Multiple regression analysis did not perform better than the abovementioned simple regression analysis.

Discussion

In this ex vivo study, the estimation of cortical thickness (Ct.Th) and porosity (Ct.Po) at the human tibia using full spectrum guided-wave analysis was successfully validated against site-matched high-resolution micro-computed tomography (μCT). We utilized a novel 500-kHz axial transmission (AT) transducer which was designed to optimize the excitation of guided wave modes at the diaphysis of the tibia. Furthermore, we accounted for a possible inter-specimen variation of the cortical bone matrix elasticity by incorporating the acoustic impedance from site-matched scanning acoustic microscopy (SAM). The variability of the matrix elasticity did not improve our model-based predictions of Ct.Po and Ct.Th. This result supports the concept of variations in matrix stiffness which has a minor impact on the effective elasticity tensor compared to the effect of variations in porosity [26]. Note that our matrix stiffness measurements might have also been biased by experimental errors. For the first time, the A_0 mode velocity (v_{A0}) was measured in human cortical bone using SVD-enhanced 2D Fourier transforms and compared to site-matched Ct.Th and Ct.Po at the same time.

The systematic overestimation of Ct.Th (0.28 mm) by AT has twofold implications. On the one hand, the $Ct.Th_{\mu CT}$ reference measurement is affected by the natural variability of the bone morphology, as illustrated in Fig. 5, and by the horizontal error bars of Fig. 4a. On the other hand, the exact behavior of guided waves in samples with irregular and trabecularized boundaries (Fig. 5c) has not yet been

Table 1 Descriptive statistics: mean, standard deviation (SD), and range of the measurement variables. R^2 of the univariate linear regression between the variables. The outlier (Fig. 4 circle) has not been removed. The associations are positive unless otherwise indicated by a negative sign. *n.s.* not significant. $N = 17$

	Descriptive statistics		R^2		
	Mean ± SD	Range	Ct.Po$_{\mu CT}$	Ct.Th$_{\mu CT}$	vBMD
Ct.Po$_{AT}$ (%)	11.1 ± 7.7	2.0–25.0	0.83***	n.s.	(−) 0.80***
Ct.Th$_{AT}$ (mm)	4.0 ± 0.6	2.9–5.2	n.s.	0.57***	n.s.
v_{FAS} (m$\cdot$s^{-1})	3806 ± 183	3429–4034	(−) 0.49**	n.s.	0.58***
v_{A0} (m$\cdot$s^{-1})	1701 ± 89	1583–1865	(−) 0.72***	0.28*	0.64***
Ct.Po$_{\mu CT}$ (%)	11.5 ± 5.2	5.6–22.8	–	0.27*	0.77***
Ct.Th$_{\mu CT}$ (mm)	3.6 ± 0.8	2.0–5.1	0.27*	–	n.s.
vBMD (g$\cdot$cm^{-3})	923 ± 59	794–980	0.77***	n.s.	–
Z$_{SAM}$ (MRayl)	6.7 ± 0.5	6.8–8.4	n.s.	n.s.	n.s.
c$_{33}$ (GPa)	32.0 ± 3.5	24.3–36.7	n.s.	n.s.	n.s.

*$p < 0.05$; **$p < 0.01$; ***$p < 0.001$
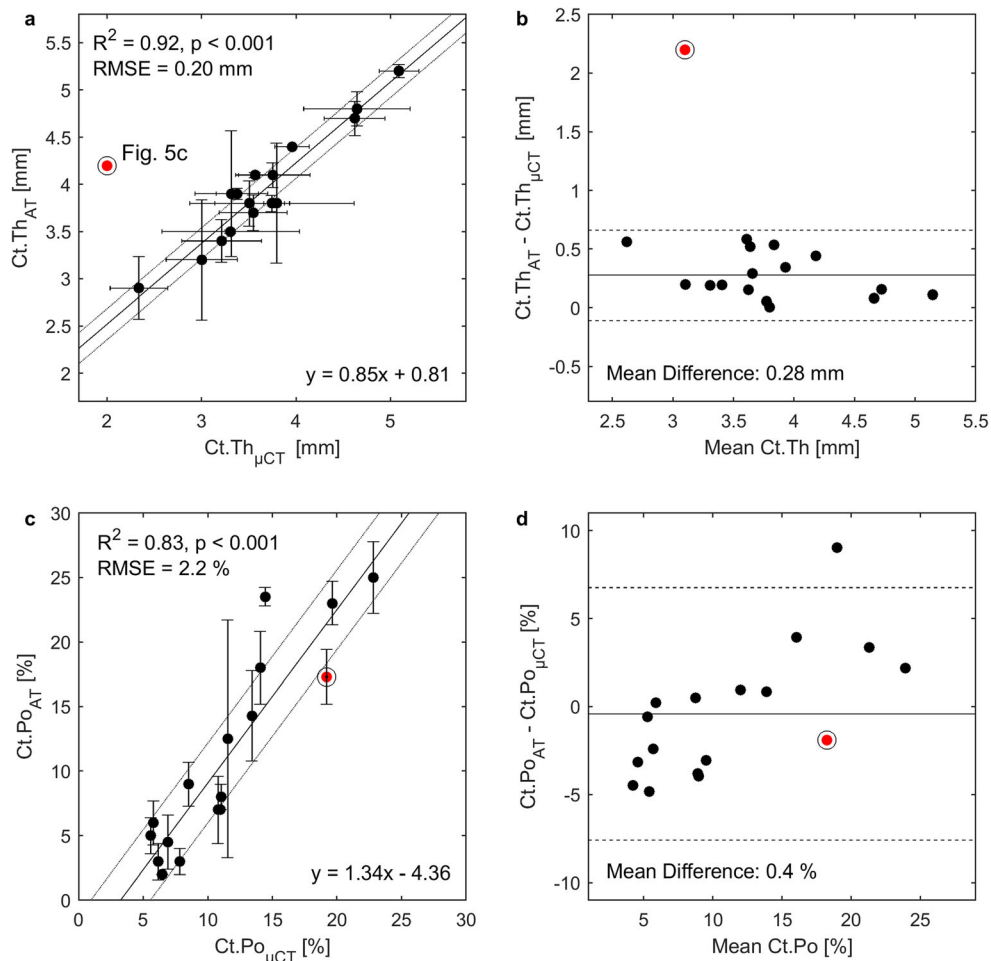
**Fig. 4** **a** Correlation between cortical thickness estimated from ultrasound axial transmission ($Ct.Th_{AT}$) and micro-computed tomography ($Ct.Th_{\mu CT}$) with 39 μm voxel size after exclusion of one outlier (red circled) (Fig. 5c). The correlation including the outlier was $R^2 = 0.57$, $p < 0.001$, RMSE 0.37 mm. Horizontal error bars represent sample-specific Ct.Th variations in the region below the probe obtained from the full width of the distance histogram at 60% of its maximum. Vertical error bars represent standard deviations (within at least two cycles). **b** Mean difference and lines of according Bland-Altman plot were calculated without outlier. Mean difference including the outlier was 0.39 mm and 0.28 mm excluding the outlier. **c** Correlation between cortical porosity from AT ($Ct.Po_{AT}$) and μCT with 7.4 μm voxel size ($Ct.Po_{\mu CT}$). **d** According Bland-Altman plot. Solid lines represent fitted linear regression curves (**a**, **c**) and *mean* values (**b**, **d**). Dotted lines in (**a**, **c**) represent RMSE. Dashed lines and in (**b**, **d**) indicate 95% confidence intervals at ± 1.96 SD. $N = 17$

investigated. Interpreting the results for these cases is particularly challenging, since the distinction of cortical bone from the trabecular compartment in the μCT images is itself a matter of arbitrary decision, as discussed in the next paragraph. Numerical simulations of ultrasound propagation using realistic (structurally heterogeneous) cortical bone models could help in clarifying to what extent trabecularized regions participate in the waveguide. Figure 4d suggests a bias of Ct.Po that depends positively on the porosity level. This bias might be partially caused by larger partial volume effects in the estimation of reference $Ct.Po_{\mu CT}$ for samples with higher Ct.Po. The assumption of a waveguide model with invariant matrix stiffness might also contribute to the bias. To partially correct for this effect, we accounted for variations in the axial tissue stiffness (c_{33}) by means of average acoustic impedance of mineralized tissue from SAM. Future ex vivo studies could

incorporate the full transverse isotropic stiffness tensor of the waveguide, e.g., as experimentally obtained from resonant ultrasound spectroscopy [39].

The prediction of Ct.Th ($R^2 = 0.57$) was weaker than for Ct.Po ($R^2 = 0.83$). This was mainly caused by one sample (indicated with a circle in Fig. 4) which had a heavily trabecularized cortex as shown in Fig. 5c. When this sample was excluded, the correlation between $Ct.Th_{AT}$ and $Ct.Th_{\mu CT}$ improved significantly (R^2 from 0.57 to 0.94, RMSE from 0.37 to 0.16 mm). We believe that this is due to the definition used for the determination of $Ct.Th_{\mu CT}$, which is especially uncertain within highly trabecularized cortical bone regions. Note that a consensus on how to segment the cortical bone compartment has not yet been reached. The longitudinal μCT section of Fig. 5c (right) obtained from the outlier sample explains the Ct.Th discrepancy between μCT (green) and
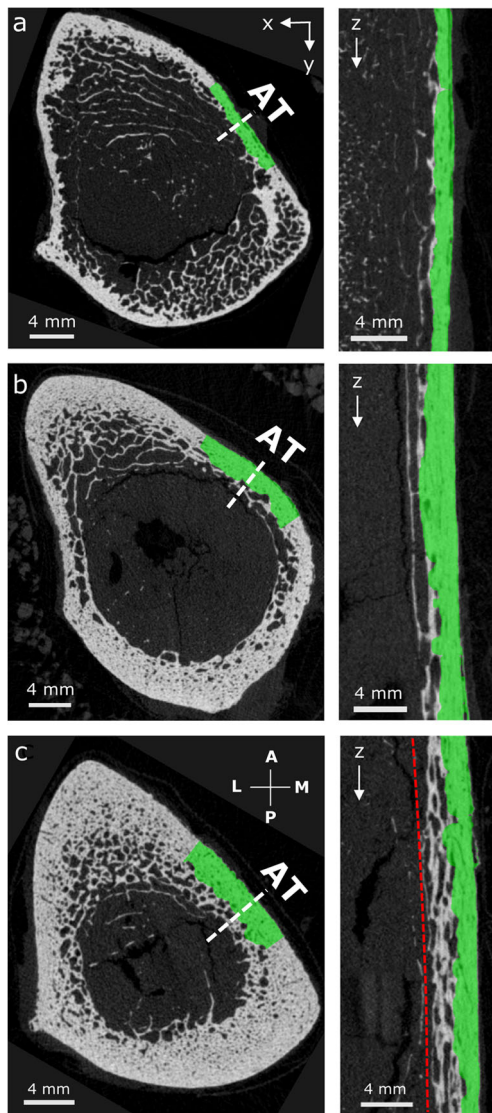
Fig. 5 Images obtained from μCT stacks of 795 slices with 39 μm isotropic voxel size. Longitudinal sections (right) were taken at the dashed line in the cross sections (left) where axial transmission (AT) was performed. The segmented cortex mask, used to calculate site-matched *vBMD* and $CtTh_{\mu CT}$, is shown in green. **a, b** AT failure cases. **c** Outlier sample with heavily trabecularized cortex (indicated by a circle in Fig. 4). Here, the measurement of a reference $CtTh_{\mu CT}$ (green) does not agree with $CtTh_{AT}$ (red line). The cross sections were rotated according to the anatomical alignment: A anterior, M medial, P posterior, and L lateral

AT (red line). The figure suggests that guided waves also propagated in the trabecularized bone region, but our applied cortical compartment segmentation algorithm [32] did not include this region.

We have used cortical bone samples from adults without report of metabolic bone diseases. For this reason, we cannot conclude on the general applicability of our method to subjects with considerably different matrix stiffness compared to normal adult bone (e.g., children, patients with osteogenesis imperfecta [40], or patients on long-term bisphosphonate treatment [41]). To overcome the assumption of invariant

matrix stiffness, the elastic tensor could be derived from the plate model instead of porosity as it was previously suggested [7, 42]. However, this approach would increase the number of unknown model coefficients and require complete resolutions of the experimental dispersion curves. Our current guided wave transducer technology is limited, particularly in spatial resolution, and therefore cannot yet provide such reconstruction quality.

The major limitation of this study was the small sample size used for statistics ($N = 17$). Nevertheless, a broad range of $Ct.Th_{\mu CT}$ (2.3–5.1 mm) and $Ct.Po_{\mu CT}$ (5.6–22.8%) was covered, which represents what is usually found in other studies [26, 43]. Furthermore, the dependency of v_{FAS} on *vBMD* is consistent with previous studies at the tibia using different frequencies (200 kHz [14], 250 kHz [44], 400 kHz [45], and 1.25 MHz [43]). However, we did not find a statistically significant correlation between v_{FAS} and $Ct.Th_{\mu CT}$, as it has been observed for the tibia using 200 kHz [14] and 400 kHz [45]. The dependency of v_{A0} on Ct.Th and *vBMD* confirms the findings of an ex vivo study at the radius using 200-kHz AT [21]. We excluded two samples due to large deviations of the ultrasonic measurements between the cycles. The one failure case (Fig. 5a) had a very thin cortical bone layer (Ct.Th < 2.0 mm) in which ultrasonic guided waves cannot sufficiently be excited using the 500-kHz probe. Alternatively, we could have used the 1-MHz probe which was originally designed for measurements at the thinner radius. The second failure case exhibited a very inhomogeneous and trabecularized cortex (Fig. 5b) which might not have guided the ultrasonic waves appropriately.

Previous studies which measured v_{A0} in cortical bone extracted the wave packages of the A_0 mode in the time domain [5, 19]. In contrast, our method isolates the A_0 dispersion curve in the frequency-phase velocity domain. We assume that this approach is more accurate since it ensures that no other signals interfere. Furthermore, we accounted for small inclination angles between the probe and bone surface using bi-directional measurements which will become more beneficial in vivo in the presence of soft tissue. However, the in vivo applicability of this novel v_{A0} measurement technique remains to be demonstrated.

A former data acquisition protocol, used by our group at the radius, was based on three cycles of ten successive measurements [42]. For the current work, we used notably longer scan times (i.e., 400 successive measurements per cycle) and slowly tilted the probe. In the post-processing, a waveguide model was then fitted to the dispersion curves of each measurement, providing estimates of Ct.Th and Ct.Po. When the dispersion curves were too noisy or incomplete, the solution to the problem was no longer unique, as indicated by several local maxima in the objective function. Therefore, we used a criterion that allowed us to exclude such problematic measurements. In the future, this automatic criterion could be evaluated in real time to retain only measurements without model ambiguities.

In conclusion, the best predictions of cortical thickness (Ct.Th) and porosity (Ct.Po) were obtained from a plate model with invariant matrix stiffness, which was fitted to the measured guided wave dispersion curves. The second best predictors of Ct.Po and Ct.Th were $vBMD$ and v_{A0}, respectively. No further enhancements were observed by accounting for variations in matrix stiffness. Clinical pilot studies are currently ongoing to confirm the possibility of a full-spectrum ultrasonic guided-wave analysis in vivo.

Compliance with ethical standards

Conflicts of interest   None.

Publisher's note   Springer Nature remains neutral with regard to jurisdictional claims in published maps and institutional affiliations.

References

1. Zebaze RM, Ghasem-Zadeh A, Bohte A et al (2010) Intracortical remodelling and porosity in the distal radius and post-mortem femurs of women: a cross-sectional study. Lancet 375:1729–1736. https://doi.org/10.1016/S0140-6736(10)60320-0

2. Sundh D, Nilsson AG, Nilsson M, Johansson L, Mellström D, Lorentzon M (2017) Increased cortical porosity in women with hip fracture. J Intern Med 281:496–506. https://doi.org/10.1111/joim.12587

3. Karjalainen J, Riekkinen O, Töyräs J et al (2008) Ultrasonic assessment of cortical bone thickness in vitro and in vivo. IEEE Trans Ultrason Ferroelectr Freq Control 55:2191–2197. https://doi.org/10.1109/TUFFC.918

4. Minonzio J-G, Talmant M, Laugier P (2010) Guided wave phase velocity measurement using multi-emitter and multi-receiver arrays in the axial transmission configuration. J Acoust Soc Am 127:2913–2919. https://doi.org/10.1121/1.3377085

5. Moilanen P, Nicholson PHF, Kilappa V, Cheng S, Timonen J (2007) Assessment of the cortical bone thickness using ultrasonic guided waves: modelling and in vitro study. Ultrasound Med Biol 33:254–262. https://doi.org/10.1016/j.ultrasmedbio.2006.07.038

6. Ta D, Wang W, Wang Y, le LH, Zhou Y (2009) Measurement of the dispersion and attenuation of cylindrical ultrasonic guided waves in long bone. Ultrasound Med Biol 35:641–652. https://doi.org/10.1016/j.ultrasmedbio.2008.10.007

7. Foiret J, Minonzio J-G, Chappard C, Talmant M, Laugier P (2014) Combined estimation of thickness and velocities using ultrasound guided waves: a pioneering study on in vitro cortical bone samples. IEEE Trans Ultrason Ferroelectr Freq Control 61:1478–1488. https://doi.org/10.1109/TUFFC.2014.3062

8. Vallet Q, Bochud N, Chappard C, Laugier P, Minonzio JG (2016) In vivo characterization of cortical bone using guided waves measured by axial transmission. IEEE Trans Ultrason Ferroelectr Freq Control 63:1361–1371. https://doi.org/10.1109/TUFFC.2016.2587079

9. Parnell WJ, Vu MB, Grimal Q, Naili S (2012) Analytical methods to determine the effective mesoscopic and macroscopic elastic properties of cortical bone. Biomech Model Mechanobiol 11:883–901. https://doi.org/10.1007/s10237-011-0359-2

10. Malo MKH, Rohrbach D, Isaksson H, Töyräs J, Jurvelin JS, Tamminen IS, Kröger H, Raum K (2013) Longitudinal elastic properties and porosity of cortical bone tissue vary with age in human proximal femur. Bone 53:451–458. https://doi.org/10.1016/j.bone.2013.01.015

11. Goldman H, Bromage T, Boyde A et al (2003) Intrapopulation variability in mineralization density at the human femoral midshaft. J Anat 203:243–255. https://doi.org/10.1046/j.1469-7580.2003.00212.x

12. Roschger P, Paschalis EP, Fratzl P, Klaushofer K (2008) Bone mineralization density distribution in health and disease. Bone 42:456–466. https://doi.org/10.1016/j.bone.2007.10.021

13. Perilli E, Bala Y, Zebaze R, Reynolds KJ, Seeman E (2015) Regional heterogeneity in the configuration of the intracortical canals of the femoral shaft. Calcif Tissue Int 97:327–335. https://doi.org/10.1007/s00223-015-0014-5

14. Moilanen P, Nicholson PHF, Kärkkäinen T et al (2003) Assessment of the tibia using ultrasonic guided waves in pubertal girls. Osteoporos Int 14:1020–1027. https://doi.org/10.1007/s00198-003-1528-7

15. Talmant M, Kolta S, Roux C, Haguenauer D, Vedel I, Cassou B, Bossy E, Laugier P (2009) In vivo performance evaluation of bidirectional ultrasonic axial transmission for cortical bone assessment. Ultrasound Med Biol 35:912–919. https://doi.org/10.1016/j.ultrasmedbio.2008.12.008

16. Moilanen P, Määttä M, Kilappa V, Xu L, Nicholson PHF, Alén M, Timonen J, Jämsä T, Cheng S (2012) Discrimination of fractures by low-frequency axial transmission ultrasound in postmenopausal females. Osteoporos Int 24:723–730. https://doi.org/10.1007/s00198-012-2022-x

17. Knapp KM, Blake GM, Fogelman I et al (2002) Multisite quantitative ultrasound: Colles' fracture discrimination in postmenopausal women. Osteoporos Int J Establ Result Coop Eur Found Osteoporos Natl Osteoporos Found USA 13:474–479. https://doi.org/10.1007/s001980200057

18. Moilanen P, Nicholson PHF, Kilappa V, Cheng S, Timonen J (2006) Measuring guided waves in long bones: modeling and experiments in free and immersed plates. Ultrasound Med Biol 32:709–719. https://doi.org/10.1016/j.ultrasmedbio.2006.02.1402

19. Tatarinov A, Sarvazyan A, Beller G, Felsenberg D (2011) Comparative examination of human proximal tibiae in vitro by ultrasonic guided waves and pQCT. Ultrasound Med Biol 37:1791–1801. https://doi.org/10.1016/j.ultrasmedbio.2011.04.013

20. Talmant M, Foiret J, Minonzio J-G (2011) Guided waves in cortical bone. In: Laugier P, Haïat G (eds) Bone Quantitative Ultrasound Chap. 7. Springer Netherlands, Dordrecht

21. Muller M, Moilanen P, Bossy E, Nicholson P, Kilappa V, Timonen J, Talmant M, Cheng S, Laugier P (2005) Comparison of three ultrasonic axial transmission methods for bone assessment. Ultrasound Med Biol 31:633–642. https://doi.org/10.1016/j.ultrasmedbio.2005.02.001

22. Moilanen P, Talmant M, Kilappa V, Nicholson P, Cheng S, Timonen J, Laugier P (2008) Modeling the impact of soft tissue on axial transmission measurements of ultrasonic guided waves in

human radius. J Acoust Soc Am 124:2364–2373. https://doi.org/10.1121/1.2973228

23. Minonzio J-G, Bochud N, Vallet Q, Bala Y, Ramiandrisoa D, Follet H, Mitton D, Laugier P (2018) Bone cortical thickness and porosity assessment using ultrasound guided waves: an ex vivo validation study. Bone 116:111–119. https://doi.org/10.1016/j.bone.2018.07.018

24. Moreau L, Minonzio J-G, Talmant M, Laugier P (2014) Measuring the wavenumber of guided modes in waveguides with linearly varying thickness. J Acoust Soc Am 135:2614–2624. https://doi.org/10.1121/1.4869691

25. Minonzio J-G, Foiret J, Moilanen P et al (2014) A free plate model can predict guided modes propagating in tubular bone-mimicking phantoms. J Acoust Soc Am 137:EL98–EL104. https://doi.org/10.1121/1.4903920

26. Granke M, Grimal Q, Saïed A, Nauleau P, Peyrin F, Laugier P (2011) Change in porosity is the major determinant of the variation of cortical bone elasticity at the millimeter scale in aged women. Bone 49:1020–1026. https://doi.org/10.1016/j.bone.2011.08.002

27. Bossy E, Talmant M, Laugier P (2004) Bi-directional axial transmission improves accuracy and precision of ultrasonic velocity measurement in cortical bone. IEEE Trans Ultrason Ferroelectr Freq Control 51(1):71–79

28. Bossy E, Talmant M, Defontaine M, Patat F, Laugier P (2004) Bidirectional axial transmission can improve accuracy and precision of ultrasonic velocity measurement in cortical bone: a validation on test materials. IEEE Trans Ultrason Ferroelectr Freq Control 51:71–79. https://doi.org/10.1109/TUFFC.2004.1268469

29. Talmant M, Kolta S, Roux C, Haguenauer D, Vedel I, Cassou B, Bossy E, Laugier P (2009) In vivo performance evaluation of bi-directional ultrasonic axial transmission for cortical bone assessment. Ultrasound Med Biol 35:912–919. https://doi.org/10.1016/j.ultrasmedbio.2008.12.008

30. Minonzio J-G, Talmant M, Laugier P (2010) Guided wave phase velocity measurement using multi-emitter and multi-receiver arrays in the axial transmission configuration. J Acoust Soc Am 127:2913–2919. https://doi.org/10.1121/1.3377085

31. Otsu N (1979) A threshold selection method from gray-level histograms. IEEE Trans Syst Man Cybern 9:62–66

32. Burghardt AJ, Buie HR, Laib A, Majumdar S, Boyd SK (2010) Reproducibility of direct quantitative measures of cortical bone microarchitecture of the distal radius and tibia by HR-pQCT. Bone 47:519–528. https://doi.org/10.1016/j.bone.2010.05.034

33. Chappard C, Bensalah S, Olivier C, Gouttenoire PJ, Marchadier A, Benhamou C, Peyrin F (2013) 3D characterization of pores in the cortical bone of human femur in the elderly at different locations as determined by synchrotron micro-computed tomography images. Osteoporos Int 24:1023–1033. https://doi.org/10.1007/s00198-012-2044-4

34. Raum K, Jenderka KV, Klemenz A, Brandt J (2003) Multilayer analysis: quantitative scanning acoustic microscopy for tissue characterization at a microscopic scale. IEEE Trans Ultrason Ferroelectr Freq Control 50:507–516. https://doi.org/10.1109/TUFFC.2003.1201463

35. Raum K, Reißhauer J, Brandt J (2004) Frequency and resolution dependence of the anisotropic impedance estimation in cortical bone using time-resolved scanning acoustic microscopy. J Biomed Mater Res A 71A:430–438. https://doi.org/10.1002/jbm.a.30156

36. Lakshmanan S, Bodi A, Raum K (2007) Assessment of anisotropic tissue elasticity of cortical bone from high-resolution, angular acoustic measurements. IEEE Trans Ultrason Ferroelectr Freq Control 54:1560–1570. https://doi.org/10.1109/TUFFC.2007.426

37. Preininger B, Checa S, Molnar FL, Fratzl P, Duda GN, Raum K (2011) Spatial-temporal mapping of bone structural and elastic properties in a sheep model following osteotomy. Ultrasound Med Biol 37:474–483. https://doi.org/10.1016/j.ultrasmedbio.2010.12.007

38. Glüer DC-C, Blake G, Lu Y et al (1995) Accurate assessment of precision errors: how to measure the reproducibility of bone densitometry techniques. Osteoporos Int 5:262–270. https://doi.org/10.1007/BF01774016

39. Bernard S, Schneider J, Varga P, Laugier P, Raum K, Grimal Q (2016) Elasticity–density and viscoelasticity–density relationships at the tibia mid-diaphysis assessed from resonant ultrasound spectroscopy measurements. Biomech Model Mechanobiol 15:97–109. https://doi.org/10.1007/s10237-015-0689-6

40. Weber M, Roschger P, Fratzl-Zelman N, Schöberl T, Rauch F, Glorieux FH, Fratzl P, Klaushofer K (2006) Pamidronate does not adversely affect bone intrinsic material properties in children with osteogenesis imperfecta. Bone 39:616–622. https://doi.org/10.1016/j.bone.2006.02.071

41. Allen MR (2018) Recent advances in understanding bisphosphonate effects on bone mechanical properties. Curr Osteoporos Rep 16:198–204. https://doi.org/10.1007/s11914-018-0430-3

42. Bochud N, Vallet Q, Bala Y, Follet H, Minonzio JG, Laugier P (2016) Genetic algorithms-based inversion of multimode guided waves for cortical bone characterization. Phys Med Biol 61:6953–6974. https://doi.org/10.1088/0031-9155/61/19/6953

43. Sievänen H, Cheng S, Ollikainen S, Uusi-Rasi K (2001) Ultrasound velocity and cortical bone characteristics in vivo. Osteoporos Int 12:399–405. https://doi.org/10.1007/s001980170109

44. Foldes AJ, Rimon A, Keinan DD, Popovtzer MM (1995) Quantitative ultrasound of the tibia: a novel approach for assessment of bone status. Bone 17:363–367. https://doi.org/10.1016/S8756-3282(95)00244-8

45. Kilappa V, Moilanen P, Xu L, Nicholson PHF, Timonen J, Cheng S (2010) Low-frequency axial ultrasound velocity correlates with bone mineral density and cortical thickness in the radius and tibia in pre- and postmenopausal women. Osteoporos Int 22:1103–1113. https://doi.org/10.1007/s00198-010-1273-7

Journal Data Filtered By: **Selected JCR Year: 2017** Selected Editions: SCIE,SSCI
Selected Categories: **"RADIOLOGY, NUCLEAR MEDICINE and MEDICAL IMAGING"** Selected Category Scheme: WoS
Gesamtanzahl: 128 Journale

Rank	Full Journal Title	Total Cites	Journal Impact Factor	Eigenfactor Score
1	JACC-Cardiovascular Imaging	8,104	10.247	0.026360
2	European Heart Journal-Cardiovascular Imaging	4,630	8.336	0.020640
3	EUROPEAN JOURNAL OF NUCLEAR MEDICINE AND MOLECULAR IMAGING	14,983	7.704	0.024870
4	RADIOLOGY	54,109	7.469	0.063710
5	JOURNAL OF NUCLEAR MEDICINE	27,101	7.439	0.037560
6	CLINICAL NUCLEAR MEDICINE	4,756	6.281	0.006950
7	INVESTIGATIVE RADIOLOGY	6,486	6.224	0.012410
8	Circulation-Cardiovascular Imaging	5,438	6.221	0.020160
9	IEEE TRANSACTIONS ON MEDICAL IMAGING	17,837	6.131	0.024200
10	ULTRASOUND IN OBSTETRICS & GYNECOLOGY	12,420	5.654	0.018820
11	INTERNATIONAL JOURNAL OF RADIATION ONCOLOGY BIOLOGY PHYSICS	46,595	5.554	0.055060
12	JOURNAL OF CARDIOVASCULAR MAGNETIC RESONANCE	4,918	5.457	0.013530
13	NEUROIMAGE	92,719	5.426	0.152610
14	MEDICAL IMAGE ANALYSIS	6,383	5.356	0.011900
15	RADIOTHERAPY AND ONCOLOGY	17,184	4.942	0.027840
16	HUMAN BRAIN MAPPING	20,334	4.927	0.042810
17	SEMINARS IN NUCLEAR MEDICINE	2,285	4.558	0.002990
18	ULTRASCHALL IN DER MEDIZIN	2,201	4.389	0.004310
19	MAGNETIC RESONANCE IN MEDICINE	31,440	4.082	0.034130
20	EUROPEAN RADIOLOGY	18,615	4.027	0.034120
20	SEMINARS IN RADIATION ONCOLOGY	2,480	4.027	0.003620
22	JOURNAL OF NUCLEAR CARDIOLOGY	3,508	3.847	0.004120
23	AMERICAN JOURNAL OF NEURORADIOLOGY	22,667	3.653	0.029840
24	JOURNAL OF MAGNETIC RESONANCE IMAGING	16,398	3.612	0.027440
25	MOLECULAR IMAGING AND BIOLOGY	2,415	3.608	0.005480

Rank	Full Journal Title	Total Cites	Journal Impact Factor	Eigenfactor Score
26	Biomedical Optics Express	8,120	3.482	0.022750
27	INTERNATIONAL JOURNAL OF HYPERTHERMIA	3,350	3.440	0.004040
28	Journal of the American College of Radiology	3,228	3.383	0.007340
29	RADIOGRAPHICS	11,207	3.249	0.008990
30	AMERICAN JOURNAL OF ROENTGENOLOGY	33,453	3.125	0.031050
31	Journal of Cardiovascular Computed Tomography	1,608	3.095	0.004280
32	KOREAN JOURNAL OF RADIOLOGY	2,331	3.072	0.004670
33	NMR IN BIOMEDICINE	7,537	3.031	0.014150
34	CANCER IMAGING	1,150	3.016	0.002250
35	Contrast Media & Molecular Imaging	1,215	2.934	0.002490
36	MEDICAL PHYSICS	25,701	2.884	0.035220
37	Radiation Oncology	5,157	2.862	0.013540
38	EUROPEAN JOURNAL OF RADIOLOGY	12,571	2.843	0.025400
39	Clinical Neuroradiology	630	2.790	0.002090
40	JOURNAL OF VASCULAR AND INTERVENTIONAL RADIOLOGY	9,021	2.758	0.012460
41	JOURNAL OF NEURORADIOLOGY	949	2.706	0.001620
42	PHYSICS IN MEDICINE AND BIOLOGY	24,912	2.665	0.032160
43	ULTRASOUND IN MEDICINE AND BIOLOGY	10,316	2.645	0.013450
44	EJNMMI Research	1,110	2.630	0.004030
45	MAGNETIC RESONANCE IMAGING	7,194	2.564	0.011680
46	RADIATION RESEARCH	8,468	2.530	0.006760
47	STRAHLENTHERAPIE UND ONKOLOGIE	2,820	2.459	0.004600
48	ABDOMINAL IMAGING	3,203	2.443	0.005940
49	COMPUTERIZED MEDICAL IMAGING AND GRAPHICS	2,190	2.435	0.002730
49	Dose-Response	824	2.435	0.001320
51	ULTRASONICS	6,518	2.377	0.009140
52	QUARTERLY JOURNAL OF NUCLEAR MEDICINE AND MOLECULAR IMAGING	1,032	2.368	0.001450
53	JOURNAL OF BIOMEDICAL OPTICS	13,503	2.367	0.019540
54	NEURORADIOLOGY	5,420	2.346	0.007640
55	ULTRASONIC IMAGING	1,076	2.300	0.000690
56	CLINICAL RADIOLOGY	6,234	2.282	0.008470

Selected JCR Year: 2017; Selected Categories: "RADIOLOGY, NUCLEAR MEDICINE and MEDICAL IMAGING"

● *Original Contribution*

IN VIVO MEASUREMENTS OF CORTICAL THICKNESS AND POROSITY AT THE PROXIMAL THIRD OF THE TIBIA USING GUIDED WAVES: COMPARISON WITH SITE-MATCHED PERIPHERAL QUANTITATIVE COMPUTED TOMOGRAPHY AND DISTAL HIGH-RESOLUTION PERIPHERAL QUANTITATIVE COMPUTED TOMOGRAPHY

JOHANNES SCHNEIDER,* DONATIEN RAMIANDRISOA,[†,‡] GABRIELE ARMBRECHT,[§] ZULLY RITTER,[§]
DIETER FELSENBERG,[§] KAY RAUM,* and JEAN-GABRIEL MINONZIO[†,¶]

* Berlin-Brandenburg School for Regenerative Therapies (BSRT), Charité−Universitätsmedizin Berlin, Berlin, Germany;
[†] Laboratoire d'Imagerie Biomédicale (LIB), Sorbonne University, CNRS, INSERM, Paris, France; [‡] BleuSolid, Pomponne, France;
[§] Center for Muscle and Bone Research (ZMK), Charité−Universitätsmedizin Berlin, Berlin, Germany; and [¶] Escuela de Ingeniería
Civil en Informática, Universidad de Valparaíso, Valparaíso, Chile

Abstract—The aim of this study was to estimate cortical porosity (Ct.Po) and cortical thickness (Ct.Th) using 500-kHz bi-directional axial transmission (AT). $Ct.Th_{AT}$ and $Ct.Po_{AT}$ were obtained at the tibia in 15 patients from a 2-D transverse isotropic free plate model fitted to measured guided wave dispersion curves. The velocities of the first arriving signal (υ_{FAS}) and A_0 mode (υ_{A0}) were also determined. Site-matched peripheral quantitative computed tomography (pQCT) provided volumetric cortical bone mineral density ($Ct.vBMD_{pQCT}$) and Ct. Th_{pQCT}. Good agreement was found between $Ct.Th_{AT}$ and $Ct.Th_{pQCT}$ ($R^2 = 0.62$, root mean square error [RMSE] = 0.39 mm). $Ct.vBMD_{pQCT}$ correlated with $Ct.Po_{AT}$ ($R^2 = 0.57$), υ_{FAS} ($R^2 = 0.43$) and υ_{A0} ($R^2 = 0.28$). Furthermore, a significant correlation was found between AT and distal high-resolution pQCT. The measurement of cortical parameters at the tibia using guided waves might improve the prediction of bone fractures in a cost-effective and radiation-free manner. (E-mail: kay.raum@charite.de) © 2019 The Author(s). Published by Elsevier Inc. on behalf of World Federation for Ultrasound in Medicine & Biology. This is an open access article under the CC BY-NC-ND license. (http://creativecommons.org/licenses/by-nc-nd/4.0/).

Key Words: Axial transmission ultrasound, Cortical bone porosity, Guided waves, Peripheral quantitative computed tomography, Dual-energy X-ray absorptiometry.

INTRODUCTION

The diagnosis of osteoporosis is currently based on areal bone mineral density (aBMD) measured by dual-energy X-ray absorptiometry (DXA), the current gold standard technique. However, a majority of bone fractures occur in patients who are not classified osteoporotic according to the current aBMD criteria (*T*-score < −2.5) (Schuit et al. 2004; Wainwright et al. 2005). This might be due to the technique's limited capacity to capture bone microstructure and differentiate between trabecular and cortical compartments. High-resolution peripheral quantitative computed tomography (HR-pQCT) is an advanced *in vivo* imaging technology

that provides 3-D characterization of trabecular and cortical bone at the distal radius and tibia (Boyd 2008). Recent clinical studies using HR-pQCT have reported that bone microstructure and volumetric bone mineral density (vBMD) are associated with genetic disorder (Neto et al. 2017), effect of treatment (Lespessailles et al. 2016) and fracture (Sundh et al. 2017). However, HR-pQCT cannot easily be used for population-based screening because it is expensive, voluminous, non-portable and based on ionizing radiation. Cost-effective and radiation-free systems for the measurement of bone microstructure are needed to improve the prevention of fragility fractures in our society.

Ultrasound-based solutions are attractive because they are low cost, portable and non-ionizing. The heel (calcaneus) scanner was among the first devices using the transverse transmission configuration (emitter and receiver placed on opposite sites) to measure ultrasound

Address correspondence to: Kay Raum, Berlin-Brandenburg School for Regenerative Therapies, Charité−Universitätsmedizin Berlin, Augustenburger Platz 1, 13353 Berlin, Germany. E-mail: kay.raum@charite.de

propagation through trabecular bone (Langton and Njeh 2008). Recent research has focused on the measurement of guided waves in cortical bone using the axial transmission (AT) configuration (emitter and receiver placed on the same site). Guided waves depend both on the geometry and on the material properties of the propagation medium. Accordingly, an *ex vivo* study revealed that the phase velocity of the A_0 mode (v_{A0}), measured at 200 kHz, was significantly correlated with cortical thickness (Ct.Th) ($R^2 = 0.52$, $p < 0.001$) and vBMD ($R^2 = 0.45$, $p < 0.001$) (Muller et al. 2005). Furthermore, it is also possible to extract the dispersion curves of multiple guided wave modes (Minonzio et al. 2010) and to predict them analytically using a 2-D transverse isotropic free plate model (Foiret et al. 2014). If constant stiffness of the bone matrix is then assumed, cortical porosity (Ct.Po) and Ct.Th can be obtained from the fitted theoretical dispersion curves (Bochud et al. 2016). Recently, this approach was validated *ex vivo* on 31 radii and 15 tibiae from human cadavers with site-matched micro-CT (Minonzio et al. 2018).

To date, guided wave measurements were performed in our group using a 1-MHz probe optimized for the radius. Recent *ex vivo* (Kroker et al. 2017) and *in vivo* (Sundh et al. 2017) studies suggest that cortical bone parameters measured at the tibia are strong predictors of hip fracture. These findings motivated us to develop a novel AT probe for ultrasound measurements at the tibia that exhibits a larger Ct.Th range ($2-6$ mm) compared with the radius ($1-4$ mm) (Karjalainen et al. 2008). To optimize the excitation of guided waves, we decreased the central frequency to 500 kHz and slightly increased the probe dimensions. The novel probe was used previously *ex vivo* on 17 tibiae and could successfully predict Ct.Po ($R^2 = 0.83$, root mean square error [RMSE] = 2.2%) and Ct.Th ($R^2 = 0.57$, RMSE 0.37 mm) measured by site-matched micro-CT (Schneider et al., 2019). The aim of this study was to test the 500-kHz probe for the first time *in vivo* at the tibia in a small group of patients. We compared the results obtained from the ultrasound measurements with those for site-matched pQCT and ultradistal HR-pQCT.

METHODS

Patients

Twenty patients (mean age: 51 ± 14 y, mean body mass index: 25.5 ± 3.0 kg/m^2) participated in this study. The study cohort represented a subgroup of 8 women and 12 men participating in two different ongoing studies. The first study was a population-based cross-sectional study approved by the local ethics committee (EA4/095/05), as well as by the German Radiation Protection Ordinance (Z5-22462/2-2005-063). The second study was a randomized controlled trial, Preventing the Impairment of Primary Osteoarthritis by High Impact Long-Term Physical Exercise Regimen, approved by the local ethics committee (EA4/027/15), as well as by the German Radiation Protection Ordinance (Z5-22462/2-2015-027). Written informed consent was obtained from all participants before recruitment.

Peripheral quantitative computed tomography

The proximal third of the tibia (66% of the lower-limb length up from the lateral malleolus of the fibula) of all patients was imaged using a clinical pQCT scanner (XCT2000, Stratec Medizintechnik GmbH, Pforzheim, Germany) according to our previously described procedure (Rittweger et al. 2000). The voxel size was $0.5 \times 0.5 \times 2.3$ mm. The cortical volumetric bone mineral density (Ct.vBMD$_{pQCT}$) was determined as the average across a single cross-sectional scan using the manufacturer's software package (threshold: 711 mg/cm^3). A custom MATLAB (The MathWorks, Natick, MA, USA) program was used to calculate the cortical thickness (Ct.Th$_{pQCT}$) based on the only available cross-sectional slice (Fig. 1b) downloaded from the scanner per patient. The tibia cross section was cropped manually before the image was binarized using Otsu's (1979) method. Subsequently, Ct.Th$_{pQCT}$ was defined as the minimum distance between the endosteal and periosteal surfaces (Chappard et al. 2013) at the medial portion of the tibia and above the medullary canal, according to the location of the ultrasound measurement.

High-resolution peripheral quantitative computed tomography

The ultradistal tibia (standard protocol, starting at 22.5 mm from the tibial endplate) of 8 patients was imaged using a clinical HR-pQCT scanner (XtremeCT I, Scanco Medical AG, Brüttisellen, Switzerland) according to our previously described procedure (Armbrecht et al. 2011). Each scan consisted of 110 slices with a nominal isotropic resolution of 82 μm. The total volumetric bone mineral density (Tt.vBMD$_{XCT}$) was obtained from the standard morphologic analysis (Boutroy et al. 2005). Then, the cortical bone compartment was segmented according to the morphologic analysis described by Burghardt et al. (2010). The following parameters were calculated based on these cortical bone volumes: Ct.vBMD$_{XCT}$, Ct.Th$_{XCT}$, cortical pore diameter (Po.Dm$_{XCT}$) and cortical porosity (Ct.Po$_{XCT}$). The scripts provided by the manufacturer were used.

Dual-energy X-ray absorptiometry

Dual-energy X-ray absorptiometry (DXA, iDXA, GE Medical Systems, WI, USA, software EnCore v13) was used to measure aBMD at the whole body
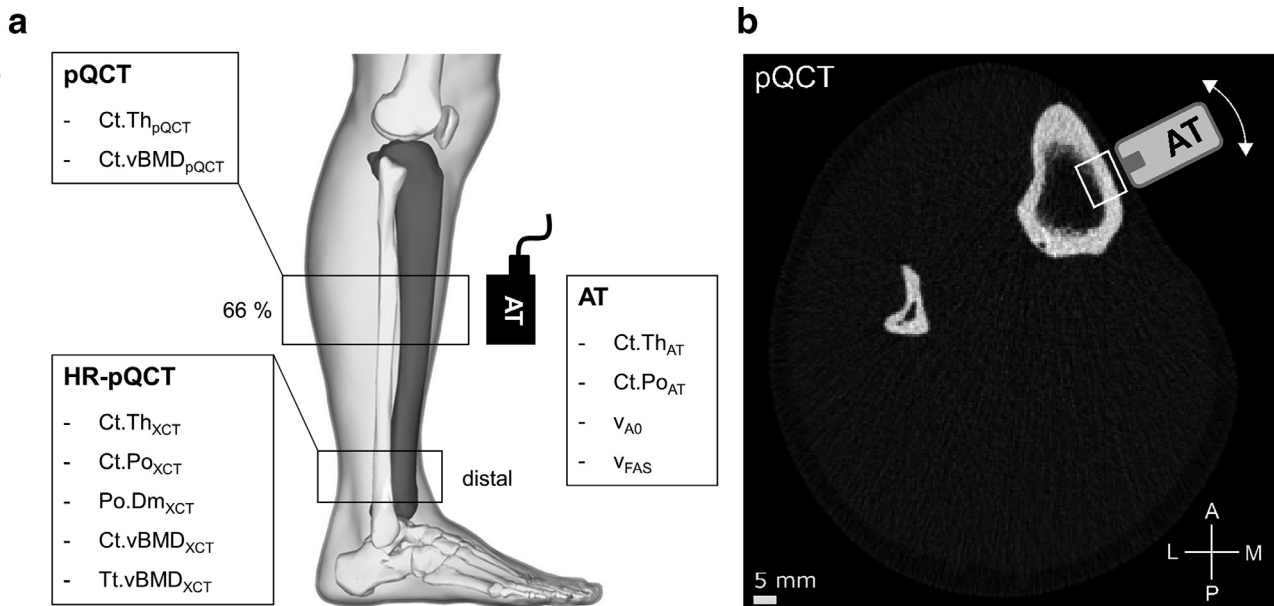
Fig. 1. (a) Overview of measurements. Five hundred-kilohertz axial transmission (AT) was performed site-matched with pQCT (voxel size: 500 μm) at the proximal third of the tibia (66%). The distal site of the same limb was scanned with HR-pQCT (voxel size: 82 μm). (b) Cross-sectional pQCT image illustrating the tangential position of the ultrasound probe, which was slowly tilted in both circumferential directions (*arrow*) during the acquisition of 400 individual measurements. The side view of the lower limb was generated with the BodyParts3D/Anatomography service (DBCLS, Japan). HR-pQCT = high-resolution peripheral quantitative computed tomography.

(aBMD$_{WB}$), lumbar spine (aBMD$_{LS}$, L1−L4 in the posterior−anterior projection) and total femur (aBMD$_{TF}$). All scans and analyses were performed by the same operator to ensure consistency and standard quality control procedures. Patients were classified as normal or osteopenic based on their total femur *T*-score in accordance with World Health Organization criteria (Kanis 1994).

Axial transmission

An ultrasound bi-directional AT system (Azalée, Paris, France) consisting of a custom-made probe (Vermon, Tours, France), driving electronics (Althais, Tours, France) and a human machine interface (HMI, Bleu-Solid, Paris, France) was used. The multichannel probe had a central 24-receiver array (pitch = 1.2 mm) and two lateral five-emitter arrays (pitch = 1.5 mm). The dimensions of each rectangular receiver and emitter were 1.2×13 and 1.5×13 mm^2, respectively. A distance of 8 mm separated the receiver array from each emitter array. This configuration enabled the propagation of ultrasound in two opposite directions, a technique that is used to correct errors induced by small inclination angles between the probe and the bone surface (Moreau et al. 2014). A wideband pulse with a center frequency of 500 kHz (−6-dB frequency bandwidth from 0.3 to 0.7 MHz) was used to excite the five multi-element transmitters successively with time delays ranging from 0 to 0.8

μs. One hundred twenty radiofrequency (RF) signals, corresponding to all possible receiver−transmission pairs, were digitized (12 bits, 20 MHz, 1024 samples) for each propagation direction after 16 averages performed by the hardware.

The ultrasound measurements were performed at the proximal third of the tibia (66%) according to the pQCT scan location (Fig. 1a). The probe was placed at the anteromedial surface of the tibia (facies medialis) aligned with the long axis of the bone. Acoustic coupling gel was used to ensure sound transmission to and from the body. The circumferential position of the probe is illustrated in Figure 1b. One measurement cycle consisted of 400 subsequent measurements. The reproducibility was assessed by repeating the acquisition of a cycle at least three times with intermediate probe repositioning. During each cycle the probe was slowly tilted in both circumferential directions to scan a wide region above the medullary cavity. During every measurement 120 RF signals (5×24) were acquired from each propagation direction. The scan time per cycle was about 3 min.

Ct.Th$_{AT}$ and Ct.Po$_{AT}$ were estimated by fitting a 2-D transverse isotropic free plate model to the measured dispersion curves as described in detail elsewhere (Minonzio et al. 2018). Briefly, the recorded time signals were transformed to the frequency−wavenumber ($f−k$) space using a 2-D spatiotemporal Fourier transform

enhanced with singular value decomposition. This provided the so-called *Norm function,* of which each pixel (f, k) reflected the presence rate of a wave mode on a 0 to 1 scale (Minonzio et al. 2010). Then, a database of dispersion curves from a 2-D transverse isotropic free plate model was projected onto the singular vector basis to obtain the objective function (Minonzio et al. 2018). The dispersion curves of the plate model were generated from a set of effective stiffness tensors which were predicted for different thickness−porosity combinations (Bochud et al. 2016; Parnell et al. 2012). We thereby assumed that the transverse isotropic elastic coefficients ($c_{11} = 26.8$ GPa, $c_{13} = 15.3$ GPa, $c_{33} = 35.1$ GPa and $c_{55} = 7.3$ GPa) and mass density ($\rho = 1.91$ g/cm^3) for the tissue matrix are invariant (Granke et al. 2011).

The objective function of the projection was obtained and optimized to find the best fit between the theoretical and experimental dispersion curves (Fig. 2a). Often, we obtained more than one local maximum mainly because of incomplete experimental dispersion curves. Such model ambiguities were removed by comparing the two highest local maxima for each of the 400 measurements of a cycle. When the highest local maximum exceeded the secondary maximum of at least 10%, this was considered to be a valid solution to the problem. Otherwise, the single measurement was rejected. If at least 10 of the 400 measurements produced a valid parameter pair, the medians of Ct.Po/Ct.Th were calculated. Otherwise, the entire measurement cycle was rejected. Finally, if at least two cycles were valid, the medians of the corresponding cycles were averaged for

every specimen. Otherwise, the entire measurement series for that sample was rejected.

The velocity of the first arriving signal (υ_{FAS}) was calculated based on a bi-directional measurement principle (Bossy et al. 2004). Briefly, the time of flight was determined for each emitter−receiver distance using the first extremum of the signal in the time domain. The sound velocity was then derived from the inverse slope of a linear fit through the measured times of flight plotted versus the known emitter−receiver distances. This procedure was performed for each of the five emissions and from both directions to account for small inclination angles between the probe and the bone surface. Unstable measurements for which the absolute difference between two opposite velocities was larger than 50 m/s (Talmant et al. 2009) were eliminated. Ideally, a single measurement provided five corrected velocities, which were then averaged. Velocity histograms were obtained for each cycle, and υ_{FAS} was calculated as the average of the histogram peaks.

The A_0 mode phase velocity (υ_{A0}) was calculated in the frequency range 0.4 to 0.5 MHz (Fig. 2b). First, the Norm function was expressed in the frequency-phase velocity domain ($c_{phase} = 2\pi f/k$) (Minonzio et al. 2010). Then, its amplitudes were averaged over frequency in the phase velocity c_{phase} range 1400 to 1900 m/s, and υ_{A0} was defined as the maximum position of the averaged Norm function. The harmonic mean of the velocities from the two opposite emissions was calculated to correct for inclination angles between the probe and the bone surface (Bossy et al. 2004). Similarly to υ_{FAS},
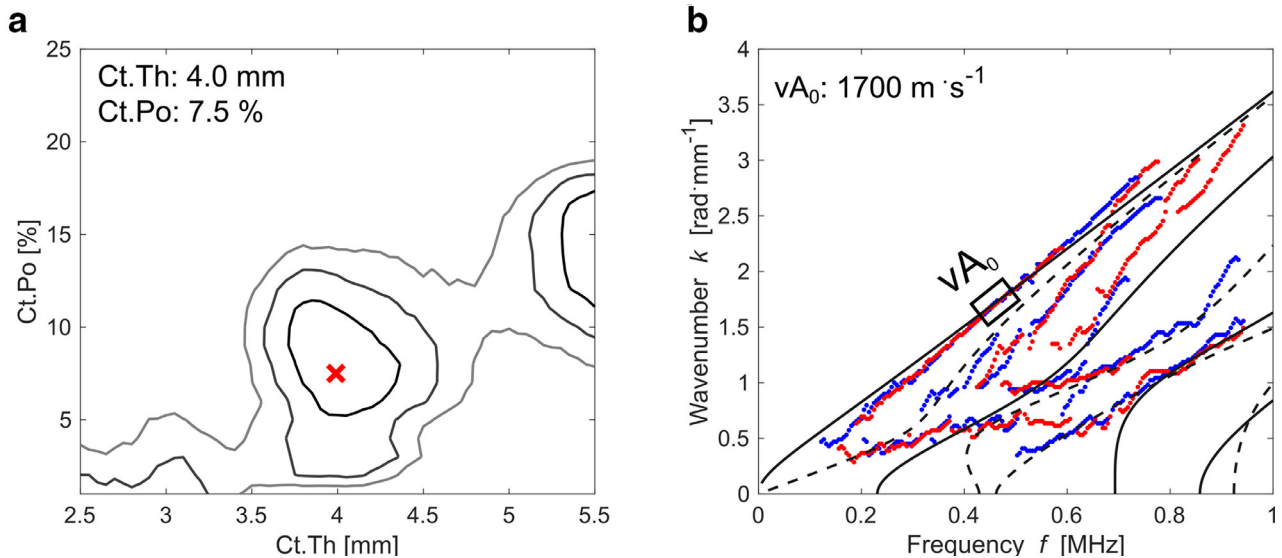

Fig. 2. (a) Contour plot depiction of the objective function. The *red cross* indicates the global maximum, corresponding to the best fit (b) between the transverse isotropic free plate model (*continuous and dashed lines*) and the measured dispersion curves (*red and blue dots*). The red and blue colors of the dots correspond to the two opposite directions of the bi-directional guided wave measurements.

measurements for which the absolute difference between two opposite velocities was larger than 50 m/s were considered unstable and eliminated. The subject's final v_{A0} was calculated by averaging the peak values of the velocity histograms obtained for each cycle.

Statistical analysis

Linear regression analysis and Pearson's correlation coefficients were used to quantify the degree of association between site-matched parameters obtained with AT and pQCT. Associations between AT and HR-pQCT were assessed using Spearman's rank-correlation coefficient. AT (N = 15), pQCT (N = 15) and HR-pQCT (N = 8) parameters were normally distributed as determined by Shapiro−Wilk tests. The Bland−Altman plot was used to reveal biases in the prediction of Ct.Th$_{pQCT}$. Differences between the means were tested with paired *t*-tests. Correlations were considered statistically significant for *p* values < 0.05. The AT *in vivo* single-cycle repeatability (Ct.Th$_{AT}$, Ct.Po$_{AT}$, v_{FAS} and v_{A0}) was estimated using the root-mean-square average of the standard deviation of repeated cycles for each measured patient (Glüer et al. 1995). Unless stated otherwise, all image processing and statistical analysis were performed using MATLAB (R2017a).

RESULTS

The ultrasound measurements from 15 of 20 patients were used for statistical analysis. Five patients were excluded after evaluating the pQCT scans because Ct.Th$_{pQCT}$ was below 2.5 mm. In such thin cortical layers, our ultrasound transducer does not excite sufficient guided wave modes (in particular those existing at higher frequencies) because of its limited frequency bandwidth. Thirteen of the 15 patients received DXA scans at the proximal femur. The total femur *T*-score was used to classify the patients into two groups: osteopenic ($-2.5 <$ *T*-score < -1.0, N = 4) and normal (*T*-score > -1.0, N = 9). Note that no osteoporotic patients (*T*-score < -2.5) were included. Between both groups, no statistically significant differences were found for the AT, pQCT and HR-pQCT parameters. The single-cycle repeatability of the ultrasound measurements was 0.13 mm for Ct.Th$_{AT}$, 1.6% for Ct.Po$_{AT}$, 25.8 m/s for v_{FAS} and 17.2 m/s for v_{A0}. The measurement data obtained in the study sample are summarized in Table 1.

The R^2 values of the linear regression between AT and site-matched pQCT parameters are listed in Table 2. Ct.vBMD$_{pQCT}$ was best correlated with Ct.Po$_{AT}$ ($R^2 = 0.57$, *p* < 0.001, Fig. 3a) followed by v_{FAS} ($R^2 = 0.43$, *p* < 0.01) and v_{A0} ($R^2 = 0.28$, *p* < 0.05). Good agreement was found between Ct.Th$_{AT}$ and Ct. Th$_{pQCT}$ ($R^2 = 0.62$, *p* < 0.001, RMSE = 0.39). When one

Table 1. Descriptive statistics

	Mean ± SD	Range	N
Axial transmission			
Ct.Th$_{AT}$ (mm)	4.0 ± 0.7	3.1−5.1	15
Ct.Po$_{AT}$ (%)	12.7 ± 4.2	5.3−20	15
v_{A0} (m/s)	1626 ± 67	1491−1711	15
v_{FAS} (m/s)	3918 ± 40	3838−3965	15
pQCT			
Ct.vBMD$_{pQCT}$ (mg/cm^3)	1176 ± 26	1134−1208	15
Ct.Th$_{pQCT}$ (mm)	3.7 ± 0.8	2.7−5.1	15
HR-pQCT			
Ct.Th$_{XCT}$ (mm)	1.3 ± 0.4	0.7−1.7	8
Ct.Po$_{XCT}$ (%)	5.5 ± 1.6	2.8−7.5	8
Po.Dm$_{XCT}$ (μm)	123 ± 11	102−136	8
Ct.vBMD$_{XCT}$ (mg/cm^3)	842 ± 56	769−928	8
Tt.vBMD$_{XCT}$ (mg/cm^3)	296 ± 77	176−381	8
DXA			
aBMD$_{LS}$ (mg/cm^2)	1.19 ± 0.16	0.98−1.50	13
aBMD$_{TF}$ (mg/cm^2)	1.04 ± 0.19	0.76−1.29	13
aBMD$_{WB}$ (mg/cm^2)	1.32 ± 0.14	1.07−1.50	15

DXA = dual-energy X-ray absorptiometry; HR-pQCT = high-resolution peripheral quantitative computed tomography; SD = standard deviation.

Table 2. R^2 of the linear regression between parameters from site-matched axial transmission and peripheral quantitative computed tomography (N = 15)

	Ct.Th$_{pQCT}$	Ct.vBMD$_{pQCT}$
Ct.Th$_{AT}$	0.62[§]	ns
Ct.Po$_{AT}$	ns	(−) 0.57[§]
v_{A0}	0.31[†]	0.28[†]
v_{FAS}	ns	0.43[‡]

ns = not significant.
*The associations are positive unless otherwise indicated by a negative sign.
† *p* < 0.05.
‡ *p* < 0.01.
§ *p* < 0.001.

outlier was excluded, the correlation improved significantly ($R^2 = 0.90$, *p* < 0.001, RMSE = 0.19, Fig. 3b) and decreased the mean difference between both methods from 0.39 to 0.23 mm in the Bland−Altman plot (Fig. 3c). There was a statistically significant difference between the values of both methods with (*p* = 0.013) and without (*p* = 0.009) the outlier.

We compared the AT parameters with those of distal HR-pQCT and found a strong correlation between v_{FAS} and Tt.vBMD$_{XCT}$ (Spearman's $\rho = 0.98$, *p* = 0.0004, Fig. 4). The negative correlation between Ct. Po$_{AT}$ and Tt.vBMD$_{XCT}$ was the second strongest but did not reach the significance level (Spearman's $\rho = -0.64$, *p* = 0.096).

DISCUSSION

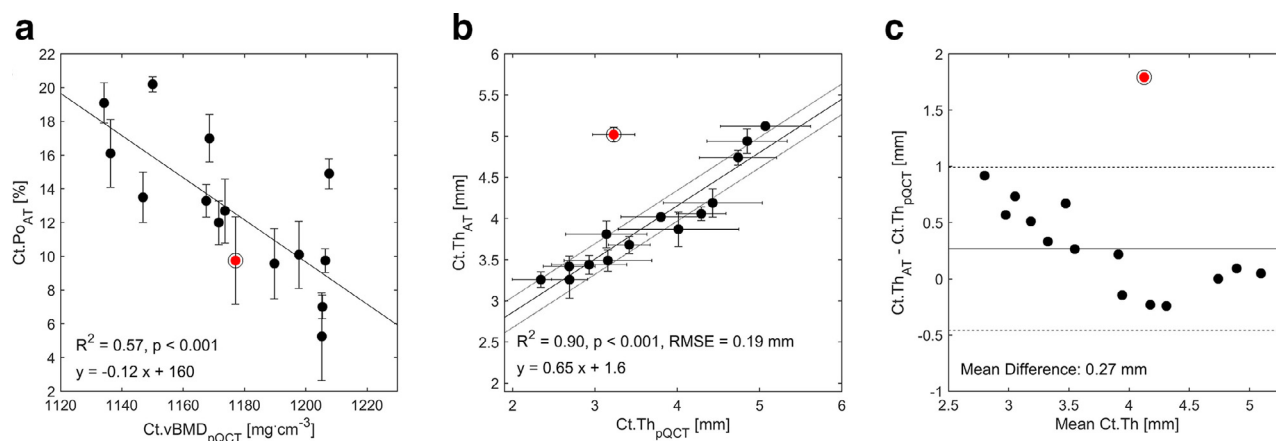In this *in vivo* pilot study, we used a novel 500-kHz tibia probe to measure guided waves successfully in 15

Fig. 3. Axial transmission versus site-matched peripheral quantitative computed tomography parameters measured at the proximal third of the tibia (N = 15). Linear regressions between (a) $Ct.Po_{AT}$ and $Ct.vBMD_{pQCT}$ and (b) $Ct.Th_{AT}$ and $Ct.Th_{pQCT}$ after exclusion of red outlier marked with circle. The correlation including the outlier was $R^2 = 0.62$, $p < 0.001$, root mean square error = 0.39 mm. The *dotted lines* in (b) indicate the root mean square error. (c) Bland−Altman plot of $Ct.Th_{AT}$ and $Ct.Th_{pQCT}$. Mean difference and lines were calculated without outlier. Mean difference with outlier was 0.33 mm. *Dashed lines* indicate 95% confidence intervals at ± 1.96 standard deviation.

patients. Excellent agreement was obtained between $Ct.Th_{AT}$ and site-matched $Ct.Th_{pQCT}$ when one outlier was removed. Moreover, $Ct.Po_{AT}$ correlated moderately with site-matched $Ct.vBMD_{pQCT}$. We adapted the ultrasound signal processing from a previously reported *ex vivo* study using a 1-MHz AT probe designed for measurements at the radius (Minonzio et al. 2018). In that way, $Ct.Th_{AT}$ and $Ct.Po_{AT}$ were obtained automatically from a 2-D transverse isotropic free plate model, which was fitted
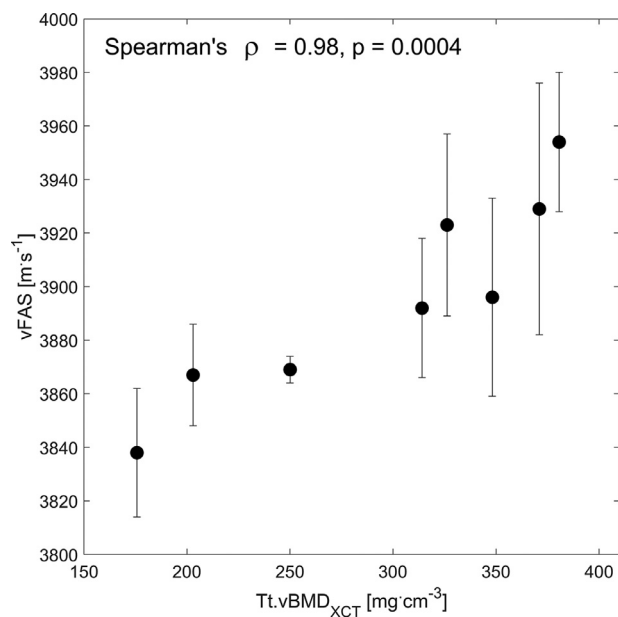

Fig. 4. Correlation between v_{FAS} at the midshaft and distal Tt. $vBMD_{XCT}$ with strong Spearman's rank-correlation coefficient ($\rho = 0.98$, $p < 0.001$, N = 8). Vertical error bars represent standard deviations (within at least three repeated cycles).

to the extracted dispersion curves. We also modified the former *in vivo* measurement protocol (Vallet et al. 2016): The number of measurements per cycle was increased from 10 to 400, and the probe was slowly tilted in both circumferential directions during the acquisitions, instead of performing static measurements. Thus, we maintained a similar single cycle repeatability *in vivo* (Ct.Po: 1.6%, Ct.Th: 0.13 mm) as previously reported *ex vivo* using the 1-MHz probe (Ct.Po = 1.9%, Ct.Th = 0.11 mm) (Minonzio et al. 2018).

A moderate correlation between site-matched $Ct.Po_{AT}$ and $Ct.vBMD_{pQCT}$ was found ($R^2 = 0.57$, $p < 0.001$). Because vBMD is a strong predictor of $Ct.Po$ ($R = -0.88$, $p < 0.001$) (Ostertag et al. 2016), a stronger correlation could have been expected. Several factors could have contributed to it. First, the AT and pQCT scan regions were not exactly site-matched. The pQCT device scanned only a 2.3-mm-thick section, whereas the region scanned by AT was much larger (*i.e.,* approximately 29 mm, according to the length of the receiver array). Second, $Ct.vBMD_{pQCT}$ was calculated from the entire cortical compartment, whereas AT scanned only the facies medialis (Fig. 1b). A more precise $Ct.vBMD_{pQCT}$ evaluation, that is, smaller region of interest, would have caused unreliable estimates because of the limited number of available cortical bone voxels (pQCT is a single-slice method with in-plane spatial resolution of 0.5 mm). In a recent *ex vivo* study using the same probe and site-matched μCT (with a 39-μm isotropic voxel size), we found a stronger correlation between $Ct.Po_{AT}$ and $Ct.vBMD_{μCT}$ ($R^2 = 0.80$, $p < 0.001$) (Schneider et al., under revision). To achieve this, we had the means to adequately segment the cortical

compartment (Burghardt et al. 2010) and considered only the volume below the receiver array. Moreover, these e*x vivo* measurements were conducted without overlaying soft tissue, which might have improved the correlation.

It is possible that soft tissue negatively affected the quality of our signals, reducing the accuracy of the fit between the plate model and the experimental dispersion curves. The accurate estimation of waveguide properties was previously reported despite the presence of soft tissue modes, but only in 4 patients and using a 1-MHz AT probe (Bochud et al. 2017). In that study, a bilayer model was proposed to account for additional soft tissue modes. However, the authors finally suggested using the plate model, because it was able to predict the experimental modes of the cortical waveguide equally well as the bilayer model, but with less complexity and computational cost. On the basis of this finding, we used the simpler plate model to predict the dispersion curves measured in this study at the tibia.

Five of 20 patients had to be excluded because they had thin cortical bone layers at the ultrasound measurement site ($Ct.Th_{pQCT} < 2.5$ mm). Interestingly, 3 of these 5 excluded cases were significantly older (73 ± 6 y) than the mean age of the 15 patients analyzed (47 ± 10 y). The decreased Ct.Th of these elderly patients might have been caused by endosteal trabecularization, which their pQCT scans also indicated. However, the two other excluded patients were relatively young (35 and 43 y), indicating that thin cortical bone at the tibia is present in patients of different ages. As a solution, the 1-MHz probe, originally designed for measurements at the thinner radius, could be used at the tibia when guided waves are not sufficiently excited using the 500-kHz probe. In the future, capacitive micromachined ultrasonic transducers (CMUTs) might allow the design of a probe with a larger frequency bandwidth. CMUTs in combination with a smaller pitch, although keeping a similar receiver array length, could significantly enhance the detection of guided wave modes over a larger Ct.Th range.

It is a limitation that the distal tibiae of only 8 patients were scanned with HR-pQCT. Thus, the linear regression analysis between the AT and distal HR-pQCT measurement parameters needs to be considered with caution because of the small sample size. However, we found a statistically significant correlation (v_{FAS} vs. Tt.vBMD$_{XCT}$, Fig. 4) that underlines the sensitivity of this parameter to systemic microstructural changes. This finding suggests that guided wave measurements conducted at the midshaft tibia may also reflect microstructural changes at relevant fracture sites, such as the proximal femur. However, tibial v_{FAS} at 250 kHz has previously been found to correlate only weakly with femoral strength

(Bouxsein et al. 1999) and to be a poor discriminant of osteoporotic fracture (Stegman et al. 1995). To date, only one study investigated the direct association between Ct. Po at the tibia midshaft and femoral neck fracture strength ($R = -0.50$, $p < 0.001$, N = 56) (Abraham et al. 2015). A strength of our ultrasound system is that it measures four cortical bone parameters at the same time (Ct.Th$_{AT}$, Ct.Po$_{AT}$, v_{FAS} and v_{A0}), which may provide improved fracture prediction combined using multivariate models. The scope of forthcoming studies will be to relate these four ultrasound parameters to hip fracture, alone or in conjunction with other measurements.

In this study, we used a first-generation HR-pQCT system (XCT-I, isotropic voxel size: 82 μm), which allows scanning of only the distal tibia (Boyd 2008). At this site, we could not conduct site-matched guided wave measurements because the cortex is too thin (Ct.Th < 2 mm) and the facies medialis is not flat enough. We did not find any statistically significant correlation between the AT and cortical HR-pQCT parameters (Ct.Th$_{XCT}$, Ct.Po$_{XCT}$, Po.Dm$_{XCT}$, Ct.vBMD$_{XCT}$). Only v_{FAS} against Tt.vBMD$_{XCT}$ reached the significance level (Fig. 4). However, this correlation needs to be considered with caution because of the small sample size. One reason for the absence of significant correlations between the cortical AT and HR-pQCT parameters may be the distinct characteristic pattern of trabecular and cortical bone mass distributions across the tibia. For example, toward the epiphyses, cortical bone exhibits significantly lower vBMD values compared with more proximal sites (Kamer et al. 2016). Furthermore, little cortical bone is present at the standard HR-pQCT ultra-distal measurement site. Therefore, cortical parameters should be assessed more proximally (Ostertag et al. 2014; Sundh et al. 2017). This is possible with the second-generation HR-pQCT (XCT-II, isotropic voxel size: 61 μm), which allows scanning of the tibia midshaft at even higher resolution (Ensrud et al. 2018). Consequently, future guided wave studies should be conducted with the site-matched XCT-II to improve the accuracy of reference thickness estimates. Moreover, it would be of great interest to observe the correlation between Ct. Po$_{AT}$ and site-matched Ct.Po$_{XCT}$, although the HR-pQCT scanner cannot accurately measure small pores with diameters less than 100 μm (Cooper et al. 2016; Ostertag et al. 2014, 2016).

We found a moderate correlation between v_{FAS} and Ct.vBMD$_{pQCT}$ ($R^2 = 0.43$, $p < 0.01$, Table 1). This finding is in agreement with previously reported *in vivo* measurements of tibial v_{FAS} at different frequencies: 200 kHz (Moilanen et al. 2003), 400 kHz (Kilappa et al. 2010) and 1.25 MHz (Sievänen et al. 2001). We did not find a statistically significant correlation between v_{FAS} and Ct.Th$_{pQCT}$ similarly to the studies at 400 kHz

(Kilappa et al. 2010) and 1.25 MHz (Sievänen et al. 2001). Only the study at 200 kHz (Moilanen et al. 2003) found a weak but statistically significant correlation ($R = 0.24$, $p < 0.05$), indicating that larger wavelengths, reaching deeper into the cortex, are needed to obtain a dependency between v_{FAS} and Ct.Th at the tibia (Bossy et al. 2005). The reproducibility of v_{FAS} (0.7 %) obtained in this study is in line with other *in vivo* studies, as, for example, the 1.8% obtained by Moilanen et al. (2003).

Compared with that of v_{A0}, the measurement of v_{A0} has been less studied *in vivo*. Here, we found that v_{A0} correlated moderately with Ct.Th$_{pQCT}$ and Ct.vBMD$_{pQCT}$. This was expected because the velocities of guided waves depend on both thickness and material properties, that is, represented here by Ct.vBMD$_{pQCT}$. Furthermore, these results agree with a clinical study using 200-kHz AT at the tibia of pubertal girls to measure v_{A0} (Moilanen et al. 2003). However, in that study the wave packages of the A_0 mode were extracted in the time domain, whereas we isolated the A_0 dispersion in the frequency-phase velocity domain. The authors report that 22% of their v_{A0} measurements were judged unreliable because of interference with soft tissue, in which ultrasound propagates at velocities ($\sim$1500 m/s) similar to those of the A_0 mode in cortical bone (Moilanen et al. 2008). In our study, we observed a regular disappearance of the A_0 mode at higher frequencies (0.5$-$1.0 MHz), particularly in patients with thick soft tissue layers. Thus, to improve robustness, we chose to estimate v_{A0} in a lower and narrower frequency range (0.4$-$0.5 MHz, Fig. 2b) compared with what we used *ex vivo* (0.5$-$0.8 MHz) (Schneider et al. 2019). Consequently, we did not observe any v_{A0} failure case and our *in vivo* reproducibility (1.1%) was superior to that of Moilanen et al. (2008), 2.3%.

CONCLUSIONS

It is possible to estimate Ct.Po and Ct.Th at the tibia using a novel 500-kHz AT probe. Good agreement was found between Ct.Th$_{AT}$ and site-matched Ct.Th$_{pQCT}$. We found a moderate correlation between Ct.Po$_{AT}$ and site-matched Ct.vBMD$_{pQCT}$ which was used as a surrogate for Ct.Po. The second-generation HR-pQCT (XCT-II), which allows measurements at the tibia midshaft with significantly enhanced resolution compared with pQCT, is now on the market. Further *in vivo* studies should be conducted site-matched with XCT-II to improve the accuracy of reference estimates. The measurement of guided waves at the tibia might improve the prediction of bone fractures in a cost-effective and radiation-free manner.

REFERENCES

Abraham AC, Agarwalla A, Yadavalli A, McAndrew C, Liu JY, Tang SY. Multiscale predictors of femoral neck in situ strength in aging women: Contributions of BMD, cortical porosity, reference point indentation, and nonenzymatic glycation. J Bone Miner Res 2015;30: 2207–2214.

Armbrecht G, Belavý DL, Backström M, Beller G, Alexandre C, Rizzoli R, Felsenberg D. Trabecular and cortical bone density and architecture in women after 60 days of bed rest using high-resolution pQCT: WISE 2005. J Bone Miner Res Off J Am Soc Bone Miner Res 2011;26:2399–2410.

Bochud N, Vallet Q, Bala Y, Follet H, Minonzio JG, Laugier P. Genetic algorithms-based inversion of multimode guided waves for cortical bone characterization. Phys Med Biol 2016;61:6953.

Bochud N, Vallet Q, Minonzio JG, Laugier P. Predicting bone strength with ultrasonic guided waves. Sci Rep 2017;7:43628.

Bossy E, Talmant M, Laugier P. Bi-directional axial transmission improves accuracy and precision of ultrasonic velocity measurement in cortical bone. IEEE Trans Ultrason Ferroelectr Freq Control 2004;51:71–79.

Bossy E, Padilla F, Peyrin F, Laugier P. Three-dimensional simulation of ultrasound propagation through trabecular bone structures measured by synchrotron microtomography. Phys Med Biol 2005;50:5545.

Boutroy S, Bouxsein ML, Munoz F, Delmas PD. In Vivo Assessment of Trabecular Bone Microarchitecture by High-Resolution Peripheral Quantitative Computed Tomography. J Clin Endocrinol Metab 2005;90:6508–6515.

Bouxsein ML, Coan BS, Lee SC. Prediction of the strength of the elderly proximal femur by bone mineral density and quantitative ultrasound measurements of the heel and tibia. Bone 1999;25:49–54.

Boyd SK. Site-specific variation of bone micro-architecture in the distal radius and tibia. J Clin Densitom 2008;11:424–430.

Burghardt AJ, Buie HR, Laib A, Majumdar S, Boyd SK. Reproducibility of direct quantitative measures of cortical bone microarchitecture of the distal radius and tibia by HR-pQCT. Bone 2010;47:519–528.

Chappard C, Bensalah S, Olivier C, Gouttenoire PJ, Marchadier A, Benhamou C, Peyrin F. 3D characterization of pores in the cortical bone of human femur in the elderly at different locations as determined by synchrotron micro-computed tomography images. Osteoporos Int 2013;24:1023–1033.

Cooper DML, Kawalilak CE, Harrison K, Johnston BD, Johnston JD. Cortical bone porosity: What is it, why is it important, and how can we detect it? Curr Osteoporos Rep 2016;14:187–198.

Ensrud KE, Vo TN, Burghardt AJ, Schousboe JT, Cauley JA, Taylor BC, Hoffman AR, Orwoll ES, Lane NE, Langsetmo L. for the Osteoporotic Fractures in Men (MrOS) Research Group. Weight loss in men in late life and bone strength and microarchitecture: A prospective study. Osteoporos Int 2018;29:1549–1558.

Foiret J, Minonzio JG, Chappard C, Talmant M, Laugier P. Combined estimation of thickness and velocities using ultrasound guided waves: A pioneering study on *in vitro* cortical bone samples. IEEE Trans Ultrason Ferroelectr Freq Control 2014;61:1478–1488.

Glüer DCC, Blake G, Lu Y, Blunt1 BA, Jergas1 M, Genant1 HK. Accurate assessment of precision errors: How to measure the reproducibility of bone densitometry techniques. Osteoporos Int 1995;5:262–270.

Granke M, Grimal Q, Saïed A, Nauleau P, Peyrin F, Laugier P. Change in porosity is the major determinant of the variation of cortical bone elasticity at the millimeter scale in aged women. Bone 2011;49:1020–1026.

Kamer L, Noser H, Blauth M, Lenz M, Windolf M, Popp AW. Bone mass distribution of the distal tibia in normal, osteopenic, and osteoporotic conditions: An ex vivo assessment using HR-pQCT,

DXA, and computational modelling. Calcif Tissue Int 2016;99: 588–597.

Kanis JA. Assessment of fracture risk and its application to screening for postmenopausal osteoporosis: Synopsis of a WHO report. WHO Study Group. Osteoporos Int 1994;4:368–381.

Karjalainen J, Riekkinen O, Töyräs J, Kröger H, Jurvelin J. Ultrasonic assessment of cortical bone thickness in vitro and in vivo. IEEE Trans Ultrason Ferroelectr Freq Control 2008;55:2191–2197.

Kilappa V, Moilanen P, Xu L, Nicholson PHF, Timonen J, Cheng S. Low-frequency axial ultrasound velocity correlates with bone mineral density and cortical thickness in the radius and tibia in pre- and postmenopausal women. Osteoporos Int 2010;22:1103–1113.

Kroker A, Plett R, Nishiyama KK, McErlain DD, Sandino C, Boyd SK. Distal skeletal tibia assessed by HR-pQCT is highly correlated with femoral and lumbar vertebra failure loads. J Biomech 2017;59: 43–49.

Langton CM, Njeh CF. The measurement of broadband ultrasonic attenuation in cancellous bone—A review of the science and technology. IEEE Trans Ultrason Ferroelectr Freq Control 2008;55:1546–1554.

Lespessailles E, Hambli R, Ferrari S. Osteoporosis drug effects on cortical and trabecular bone microstructure: A review of HR-pQCT analyses. BoneKEy Rep 2016;5 836.

Minonzio JG, Talmant M, Laugier P. Guided wave phase velocity measurement using multi-emitter and multi-receiver arrays in the axial transmission configuration. J Acoust Soc Am 2010;127:2913–2919.

Minonzio JG, Bochud N, Vallet Q, Bala Y, Ramiandrisoa D, Follet H, Mitton D, Laugier P. Bone cortical thickness and porosity assessment using ultrasound guided waves: An ex vivo validation study. Bone 2018;116:111–119.

Moilanen P, Nicholson PHF, Kärkkäinen T, Wang Q, Timonen J, Cheng S. Assessment of the tibia using ultrasonic guided waves in pubertal girls. Osteoporos Int 2003;14:1020–1027.

Moilanen P, Talmant M, Kilappa V, Nicholson P, Cheng S, Timonen J, Laugier P. Modeling the impact of soft tissue on axial transmission measurements of ultrasonic guided waves in human radius. J Acoust Soc Am 2008;124:2364–2373.

Moreau L, Minonzio JG, Talmant M, Laugier P. Measuring the wave-number of guided modes in waveguides with linearly varying thickness. J Acoust Soc Am 2014;135:2614–2624.

Muller M, Moilanen P, Bossy E, Nicholson P, Kilappa V, Timonen J, Talmant M, Cheng S, Laugier P. Comparison of three ultrasonic axial transmission methods for bone assessment. Ultrasound Med Biol 2005;31:633–642.

Neto GPC, Pereira RMR, Alvarenga JC, Takayama L, Funari MFA, Martin RM. Evaluation of bone mineral density and microarchitectural parameters by DXA and HR-pQCT in 37 children and adults with X-linked hypophosphatemic rickets. Osteoporos Int 2017; 28:1685–1692.

Ostertag A, Peyrin F, Fernandez S, Laredo JD, de Vernejoul MC, Chappard C. Cortical measurements of the tibia from high resolution peripheral quantitative computed tomography images: A comparison with synchrotron radiation micro-computed tomography. Bone 2014;63:7–14.

Ostertag A, Peyrin F, Gouttenoire PJ, Laredo JD, DeVernejoul MC, Solal MC, Chappard C. Multiscale and multimodality computed tomography for cortical bone analysis. Phys Med Biol 2016; 61:8553.

Otsu N. A threshold selection method from gray-level histograms. IEEE Trans Syst Man Cybern 1979;9:62–66.

Parnell WJ, Vu MB, Grimal Q, Naili S. Analytical methods to determine the effective mesoscopic and macroscopic elastic properties of cortical bone. Biomech Model Mechanobiol 2012;11:883–901.

Rittweger J, Beller G, Ehrig J, Jung C, Koch U, Ramolla J, Schmidt F, Newitt D, Majumdar S, Schiessl H, Felsenberg D. Bone-muscle strength indices for the human lower leg. Bone 2000;27:319–326.

Schneider J, Iori G, Ramiandrisoa D, Hammami M, Gräsel M, Chappard C, Barkmann R, Laugier P, Grimal Q, Raum K. Ex vivo cortical porosity and thickness predictions at the tibia using full spectrum ultrasonic guided wave analysis. Arch Osteoporos (2019) 14: 21. https://doi.org/10.1007/s11657-019-0578-1.

Schuit SCE, van der Klift M, Weel AEAM, de Laet CEDH, Burger H, Seeman E, Hofman A, Uitterlinden AG, van Leeuwen JPTM, Pols HAP. Fracture incidence and association with bone mineral density in elderly men and women: The Rotterdam Study. Bone 2004;34:195–202.

Sievänen H, Cheng S, Ollikainen S, Uusi-Rasi K. Ultrasound velocity and cortical bone characteristics in vivo. Osteoporos Int 2001;12:399–405.

Stegman MR, Heaney RP, Travers-Gustafson D, Leist J. Cortical ultrasound velocity as an indicator of bone status. Osteoporos Int 1995;5:349–353.

Sundh D, Nilsson AG, Nilsson M, Johansson L, Mellström D, Lorentzon M. Increased cortical porosity in women with hip fracture. J Intern Med 2017;281:496–506.

Talmant M, Kolta S, Roux C, Haguenauer D, Vedel I, Cassou B, Bossy E, Laugier P. In vivo performance evaluation of bi-directional ultrasonic axial transmission for cortical bone assessment. Ultrasound Med Biol 2009;35:912–919.

Vallet Q, Bochud N, Chappard C, Laugier P, Minonzio JG. In vivo characterization of cortical bone using guided waves measured by axial transmission. IEEE Trans Ultrason Ferroelectr Freq Control 2016;63:1361–1371.

Wainwright SA, Marshall LM, Ensrud KE, Cauley JA, Black DM, Hillier TA, Hochberg MC, Vogt MT, Orwoll ES. Hip fracture in women without osteoporosis. J Clin Endocrinol Metab 2005;90: 2787–2793.

Journal Data Filtered By: **Selected JCR Year: 2017** Selected Editions: SCIE,SSCI
Selected Categories: **"BIOPHYSICS"** Selected Category Scheme: WoS
Gesamtanzahl: 72 Journale

Rank	Full Journal Title	Total Cites	Journal Impact Factor	Eigenfactor Score
1	Physics of Life Reviews	1,381	13.783	0.002960
2	NATURE STRUCTURAL & MOLECULAR BIOLOGY	27,547	13.333	0.081820
3	Annual Review of Biophysics	2,721	11.742	0.009390
4	BIOCHIMICA ET BIOPHYSICA ACTA-REVIEWS ON CANCER	5,276	8.220	0.009300
5	BIOSENSORS & BIOELECTRONICS	48,853	8.173	0.069510
6	CURRENT OPINION IN CHEMICAL BIOLOGY	10,226	7.572	0.019010
7	QUARTERLY REVIEWS OF BIOPHYSICS	2,236	7.242	0.002790
8	Biochimica et Biophysica Acta-Gene Regulatory Mechanisms	7,047	5.179	0.019420
9	BIOCHIMICA ET BIOPHYSICA ACTA-MOLECULAR BASIS OF DISEASE	12,799	5.108	0.027740
10	BIOCHIMICA ET BIOPHYSICA ACTA-MOLECULAR AND CELL BIOLOGY OF LIPIDS	8,827	4.966	0.019590
11	STRUCTURE	14,417	4.907	0.036760
12	BIOCHIMICA ET BIOPHYSICA ACTA-BIOENERGETICS	11,931	4.280	0.022190
13	COLLOIDS AND SURFACES B-BIOINTERFACES	25,844	3.997	0.034800
14	BIOELECTROCHEMISTRY	4,076	3.789	0.004420
15	Journal of Biophotonics	2,723	3.768	0.006190
16	BIOCHIMICA ET BIOPHYSICA ACTA-GENERAL SUBJECTS	13,602	3.679	0.025440
17	Current Topics in Membranes	602	3.514	0.002170
18	BIOPHYSICAL JOURNAL	51,994	3.495	0.057840
19	BIOCHIMICA ET BIOPHYSICA ACTA-BIOMEMBRANES	16,912	3.438	0.024100
20	JOURNAL OF STRUCTURAL BIOLOGY	9,955	3.433	0.030150
21	PROGRESS IN BIOPHYSICS & MOLECULAR BIOLOGY	3,973	3.427	0.004540

Rank	Full Journal Title	Total Cites	Journal Impact Factor	Eigenfactor Score
22	Biomechanics and Modeling in Mechanobiology	2,874	3.212	0.007100
23	JOURNAL OF PHOTOCHEMISTRY AND PHOTOBIOLOGY B-BIOLOGY	9,308	3.165	0.010700
24	ARCHIVES OF BIOCHEMISTRY AND BIOPHYSICS	21,719	3.118	0.016080
25	JOURNAL OF BIOMOLECULAR STRUCTURE & DYNAMICS	3,152	3.107	0.004620
26	Acta Crystallographica Section D-Structural Biology	20,390	3.099	0.028000
27	NMR IN BIOMEDICINE	7,537	3.031	0.014150
28	FEBS LETTERS	49,716	2.999	0.044030
29	JOURNAL OF BIOENERGETICS AND BIOMEMBRANES	2,497	2.914	0.002430
30	PHOTOCHEMICAL & PHOTOBIOLOGICAL SCIENCES	6,230	2.902	0.008050
31	CHEMISTRY AND PHYSICS OF LIPIDS	4,248	2.766	0.004600
32	BIOCHIMICA ET BIOPHYSICA ACTA-PROTEINS AND PROTEOMICS	7,704	2.609	0.013080
33	INTERNATIONAL JOURNAL OF BIOMETEOROLOGY	5,208	2.577	0.006340
34	Biomicrofluidics	3,572	2.571	0.008760
35	BIOCHEMICAL AND BIOPHYSICAL RESEARCH COMMUNICATIONS	80,377	2.559	0.076330
36	RADIATION RESEARCH	8,468	2.530	0.006760
37	Biointerphases	1,587	2.455	0.003010
38	Cellular and Molecular Bioengineering	813	2.435	0.002230
39	JOURNAL OF BIOMECHANICS	29,184	2.431	0.028180
40	JOURNAL OF COMPUTER-AIDED MOLECULAR DESIGN	3,853	2.356	0.005640
41	Multisensory Research	242	2.339	0.000950
42	PROTEINS-STRUCTURE FUNCTION AND BIOINFORMATICS	15,764	2.274	0.014580
43	ACTA BIOCHIMICA ET BIOPHYSICA SINICA	2,982	2.224	0.004400

Bernard S, **Schneider J**, Varga P, Laugier P, Raum K, Grimal Q. *Elasticity–density and viscoelasticity–density relationships at the tibia mid-diaphysis assessed from resonant ultrasound spectroscopy measurements*. Biomechanics and Modeling in Mechanobiology, May 2015.

https://doi.org/10.1007/s10237-015-0689-6

Mein Lebenslauf wird aus datenschutzrechtlichen Gründen in der elektronischen Version meiner Arbeit nicht veröffentlicht.

Publications

Conferences

Schneider J, Bernard S, Minonzio JG, Varga P, Wendlandt R, Grimal Q, Laugier P, Raum K. "*Multiscale assessment of cortical bone properties with quantitative ultrasound,*" J Acoust Soc Am 2015.

Cai X, Bernard S, Laugier P, Grimal Q, **Schneider J**, Varga P, Raum K. *An introduction to measurements of human cortical bone elasticity using Resonant Ultrasound Spectroscopy*. IEEE Xplore, 2015.

Schneider J, Varga P, Zippelius T, Hoff E, Strube P, Pumberger M, Putzier M, Minonzio JG, Laugier P, Raum K. *Multisite ultrasound axial transmission study in postmenopausal women using optimized first arriving signal velocity measurements*. IEEE Xplore, 2015.

Raum K, Schrof S, **Schneider J**, Iori G, Kilappa V, Du J, Pumberger M, Putzier M, Zhou J, Isaksson H. *The role of acoustic microscopy in bone research*. J Acoust Soc Am, 2016.

Articles

Bernard S, **Schneider J**, Varga P, Laugier P, Raum K, Grimal Q. *Elasticity–density and viscoelasticity–density relationships at the tibia mid-diaphysis assessed from resonant ultrasound spectroscopy measurements*. Biomech Model Mechanobiol, 2015.

Iori G, Heyer F, Kilappa V, Wyers C, Varga P, **Schneider J**, Gräsel M, Wendlandt R, Barkmann R, van den Bergh JP, Raum K. *BMD-based assessment of local porosity in human femoral cortical bone*. Bone, 2018.

Schneider J, Ramiandriosa D, Armbrecht G, Ritter Z, Felsenberg D, Raum K, Minonzio J-G. *In vivo measurements of cortical thickness and porosity at the proximal third of the tibia using guided waves: comparison with site-matched pQCT and distal HR-pQCT*. Ultrasound Med Biol, 2019.

Schneider J, Iori G, Ramiandrisoa D, Hammami M, Gräsel M, Chappard C, Barkmann R, Laugier P, Grimal Q, Minonzio J-G, Raum K. *Ex vivo cortical porosity and thickness predictions at the tibia using full spectrum ultrasonic guided wave analysis*. Arch Osteoporos, 2019.

Iori G, **Schneider J**, Reisinger A, Heyer F, Peralta L, Wyers C, Gräsel M, Barkmann R, Glüer C, van den Bergh J, Pahr D, Raum K. *Large cortical bone pores at the tibia are associated with proximal femur strength*. Accepted for publication in PlosONE, 2019.

Acknowledgements